The versatile role of liquids in the design of functional materials: liquid-liquid wells, gels, porous polymers

Zur Erlangung des akademischen Grades eines

DOKTORS DER NATURWISSENSCHAFTEN

(Dr. rer. nat.)

von der KIT-Fakultät für Chemie und Biowissenschaften

des Karlsruher Instituts für Technologie (KIT)

vorgelegte

DISSERTATION

von

Mariia Kuzina

aus Moskau, Russland

Dekan: Prof. Dr. Hans-Achim Wagenknecht

Referent: Prof. Dr. Pavel Levkin

Korreferent: Prof. Dr. Gerardo Hernandez-Sosa

Tag der mündlichen Prüfung: 26.04.2024

"The hate of men will pass, and dictators die, and the power they took from the people will return to the people. [...] Let us fight for a world of reason, a world where science and progress will lead to all men's happiness."

Charlie Chaplin, The Final Speech from The Great Dictator

Kurzfassung

Flüssigkeiten nehmen eine zentrale Rolle im Kontinuum der Materiezustände ein. Die enorme Vielfalt an physikalischen und chemischen Eigenschaften, die im flüssigen Zustand zugänglich sind, unterstreicht ihre Rolle als grundlegendes Element beim Aufbau funktionaler Materialien und Systeme. Ihre inhärenten Fähigkeiten als Träger, Reaktionsmedien, dynamische und funktionale Komponenten machen Flüssigkeiten unverzichtbar in der Chemie, Biologie, Materialwissenschaft und Ingenieurwesen. **Ziel dieser Arbeit ist** es, die funktionale Rolle der flüssigen Phase bei der Konzeption und Entwicklung innovativer Materialien und Materialsysteme zu beleuchten und zu nutzen. Diese Arbeit strebt danach, neue Möglichkeiten in der Schaffung und Funktionalisierung von flüssigkeitsbasierten, flüssigkeitsdurchtränkten und vollständig flüssigen Materialien zu erschließen.

Das erste Projekt stellt einen innovativen Ansatz zur Handhabung von Flüssigkeiten auf gemusterten Oberflächen vor, indem „Flüssigkeitsbrunnen" für andere Flüssigkeiten auf Oberflächen geschaffen werden. Diese Methode erleichtert die Entwicklung dynamischer, selbstreparierender Flüssigkeitsbehälter für gezielte chemische Extraktion und Materialformung, eröffnet neue Wege für präzise Flüssigkeitsmanipulation in Mikrofluidikgeräten und zeigt darüber hinaus das Potenzial von Flüssigkeiten für komplexe Flüssigkeitsmusterung. Einzigartige Eigenschaften werden durch den flüssigen Zustand von Wasserwänden präsentiert, die mit festen Barrieren schwer zu erreichen sind. Die Eigenschaften und das Verhalten von Flüssigkeitsbrunnen werden mittels Raman-Spektroskopie, Kontaktwinkelgoniometrie, Simulationen und Laser-Konfokalmikroskopie sowie verschiedenen Stabilitätstests untersucht. Flüssigkeitsbrunnen ermöglichen die komplexe Verdrängung von Flüssigkeiten mit niedriger Oberflächenspannung (engl. LSTLs) mit präziser Volumenkontrolle. Sie werden als Schablonen in der wassertemplierten Polymerisation verwendet, um Polymere zu formen, wobei die Wasserwand leicht entfernt und neu geformt werden kann für schnelles Prototyping von Polymerfilmen. Die Verwendung von Wasser als durchströmbare, recycelbare Barriere dient der Trennung organischer Moleküle. Simulationen werden angewendet, um die Stabilität der Dreiphasen-Kontaktlinie zu untersuchen, die durch Oberflächenspannungsänderungen aufgrund der Gibbs-Adsorption erleichtert wird. Abschließend bietet dieser Ansatz eine allgemeine, fluorfreie und umweltfreundliche Methode zur Erstellung vollständig flüssiger, funktionaler und selbstheilender Kompartimente für die Einkapselung und Musterung von LSTLs.

Im zweiten Projekt liegt der Fokus auf flüssigkeitsdurchtränkten Materialien, Organogelen, wobei die Infusion verschiedener organischer Flüssigkeiten in 3D-gedruckte Polymere verwendet wird, um die physikalischen und mechanischen Eigenschaften der Organogele zu modulieren. Durch einen nach dem Drucken durchgeführten Quellprozess werden die Eigenschaften eines Polymer-Netzwerks von hochadhäsiv zu rutschig überführt, indem hydrophobe Lösungsmittel, einschließlich mittelkettiger Alkohole, Toluol und Öle, verwendet werden. Dies bewirkt, dass die Organogele von vollständiger Adhäsion zu verschiedenen Graden der Rutschigkeit übergehen, bis die Adhäsion vollständig eliminiert wird. Zusätzlich wird das Quellen in Lösungsmitteln mit unterschiedlichen Schmelzpunkten hinsichtlich seiner Fähigkeit untersucht, das thermo-mechanische Verhalten der Organogele zu modifizieren, ihre thermische Stabilität über einen breiten Temperaturbereich (von -30°C bis 25 und von 25 bis 100°C) zu erweitern und reversible Verhärtungs-Weichungs-Zyklen mit lösungsmittelabgestimmten Übergangstemperaturen zu ermöglichen. Die Eigenschaften der Organogele werden mit Methoden wie optischer Mikroskopie, UV-Vis-Spektroskopie, Rotationsrheometrie, Kontaktwinkelgoniometrie und Quelltests untersucht. Durch Variieren der Arten organischer Flüssigkeiten und Anpassen der 3D-Druck- und Nachbearbeitungsbedingungen beleuchtet die Studie die Beziehung zwischen Lösungsmittelmerkmalen und Organogel-Verhalten und bietet eine lösungsmittelunabhängige vielseitige Organogel-Herstellungsmethode zur weiteren Steigerung ihrer Anwendbarkeit in Mikrofluidik, weicher Robotik oder Extraktionsanwendungen.

Der dritte Abschnitt der Arbeit untersucht die Einbeziehung von flüssigen Porogenen beim 3D-Druck von porösen Polymeren. Die durch Polymerisation ererbte Porosität und eine wohldefinierte makroporöse Geometrie, geschaffen mittels DLP 3D-Druck und kritischer Punkt-Trocknung, werden mit einer computergestützten Studie der simulierten Steifigkeit basierend auf Bildern der Rasterelektronenmikroskopie des Basismaterials kombiniert. Durch Ändern der Tintenzusammensetzung und der Druckparameter wird der Einfluss von Porengröße und relativer Dichte auf die Struktursteifigkeit überwacht. Die simulierten Steifigkeitswerte für das Basispolymer stimmen mit den experimentell bestimmten elastischen Eigenschaften überein. Diese werden in Nanoindentationstests mit Youngs-Modulen von 554 bis 722 MPa basierend auf dem Co-Lösungsmittel-Verhältnis erhalten, was die Struktur-Eigenschafts-Beziehung validiert. Die Einführung von Makroporosität in Form einer 3D-tetraedrischen, biegedominierten Architektur führt zu spezifischen Youngs-Modulen von 79,5 MPa cm^3 g^{-1}, was mit Schäumen vergleichbar ist. Dieser Ansatz unterstreicht die entscheidende

Rolle von flüssigen Porogenen bei der Definition der Morphologie und Funktionalität der endgültigen Polymerstrukturen und ebnet den Weg für ihren Einsatz in Anwendungen, die spezifische mechanische Eigenschaften erfordern, wie leichte Strukturkomponenten und katalytische Träger.

Jeder Abschnitt dieser Forschung demonstriert nicht nur die einzigartigen Anwendungen von Flüssigkeiten in der Materialwissenschaft, sondern fördert auch das Feld durch die Einführung neuer Methodologien und die experimentelle, theoretische und rechnerische Erforschung der Wechselwirkungen zwischen Flüssigkeit und Material. Durch diese Erkundungen unterstreicht die Forschung das transformative Potenzial von Flüssigkeiten bei der Überbrückung traditioneller und innovativer Materialklassen und setzt einen neuen Maßstab für die Nutzung von Flüssigkeitseigenschaften im Streben nach bahnbrechenden Materiallösungen.

.

Abstract

Liquids occupy a central role in the continuum of material states. The vast diversity of physical and chemical properties accessible in the liquid state underscores their role as a foundational element in the construction of functional materials and systems. The inherent abilities as carriers, reaction media, and dynamic and functional components, make liquids indispensable across chemistry, biology, material science, and engineering applications. **The objective of this work** is to illuminate and exploit the functional role of the liquid phase in the conception and development of innovative materials and material systems. This work seeks to unlock new possibilities in the creation and functionalization of liquid-derived, liquid-infused, and all-liquid materials.

The first project introduces an inventive approach to liquid containment on patterned surfaces, creating "liquid wells" for other liquids on surfaces. This method facilitates the development of dynamic, self-repairing liquid containers for targeted chemical extraction and material shaping, opening up new avenues for precision liquid manipulation in microfluidic devices and beyond, showcasing the potential of liquids for complex liquid patterning. Unique properties are presented by the liquid state of water walls, which are difficult to achieve with solid barriers. The properties and behaviour of liquid-liquid wells are investigated by Raman spectroscopy, contact angle goniometry, simulations, and confocal laser scanning microscopy, as well as various stability tests. Liquid wells enable the complex displacement of low surface tension liquids (LSTLs) with precise volume control. They are utilized as templates in water-templated polymerization to shape polymers, with the water wall being easily removed and reformed for rapid polymer film prototyping. The use of water as a perfusable recyclable barrier is used in separating organic molecules. Simulation efforts are applied to investigate the stability of the three-phase contact line (air-organic-water), which is shown to be facilitated by surface tension changes due to Gibbs adsorption. In conclusion, this approach offers a general, fluorine-free, and eco-friendly method for creating fully liquid, functional, and self-healing compartments to confine and pattern LSTLs.

In the second project, the focus shifts to liquid-infused materials, organogels, where the infusion of various organic liquids into 3D-printed polymer is used to modulate the organogels' physical and mechanical properties. By employing a post-printing swelling process, the properties of a polymer network are shown to be transitioned from highly adhesive to slippery through the use of hydrophobic solvents, including medium-chain alcohols, toluene, and oils.

This caused the organogels to shift from complete adhesion to varying degrees of slipperiness, eventually eliminating adhesion entirely. Additionally, swelling in solvents with different melting points is investigated regarding its ability to modify the thermo-mechanical behaviour of the organogels, extending their thermal stability across a broad temperature range (from -30°C to 25 and from 25 to 100°C) and enabling them to undergo reversible hardening-softening cycles with solvent-tuned transition temperatures. The properties of organogels are examined by such methods, as optical microscopy, uv-vis spectroscopy, rotational rheometry, contact angle goniometry, and swelling tests. By varying the types of organic liquids and adjusting the 3D-printing and post-processing conditions, the study elucidates the relationship between solvent characteristics and organogel behavior and offers a solvent-independent versatile organogel fabrication method for further enhancement of their applicability in microfluidics, soft robotics, or extraction applications.

The third chapter of the work explores the incorporation of liquid porogens in the 3D printing of porous polymers. The polymerization-inherited porosity and a well-defined macroporous geometry created using DLP 3D-printing and critical point drying, are combined with a computational study of simulated stiffness based on scanning electronic microscopy images of the base material. By altering ink composition and printing parameters, the impact of pore size and relative density on structure stiffness is monitored. The simulated stiffness values for the base polymer are found to align with the experimentally determined elastic properties obtained in nanoindentation tests, with Young's moduli ranging from 554 to 722 MPa based on the co-solvent ratio, thus validating the structure-properties relationship. The introduction of macroporosity, in the form of a 3D tetrahedral bending-dominated architecture, yields specific Young's moduli of 79.5 MPa cm^3 g^{-1}, which is comparable with the stiffness of foams. This approach highlights the critical role of liquid porogens in defining the morphology and functionality of the final polymer structures, paving the way for their use in applications requiring specific mechanical characteristics, such as lightweight structural components, and catalytic supports.

Each segment of this work not only demonstrates the unique applications of liquids in material science but also attempts to advance the field through the introduction of novel methodologies and the experimental, theoretical, and computational exploration of liquid-material interactions. Through these explorations, this work underscores the transformative potential of liquids in bridging traditional and innovative material classes, setting new benchmarks for the utilization of liquid properties in the quest for cutting-edge material solutions.

Preface

This thesis was done in Levkin group from January 2020 to October 2023 at the Institute of Biological and Chemical Systems – Functional Materials Systems (IBCS-FMS) at Karlsruhe Institute of Technology. The thesis was financially supported by the Carl Zeiss Scholarship and the Cluster of Excellence "3D Matter Made To Order" (3DMM2O).

As a part of the thesis, the cooperation with other research groups took place:

- the group of PROF. BRITTA NESTLER in the projects "Liquid Wells as Analogues to Solid Vessels" and "Equilibrium droplet shapes on chemically patterned surfaces";
- the group of PROF. RUTH SCHWAIGER and the group of PROF. SHU-WEI CHANG in the project "3D-Printed Inherently Porous Structures with Tetrahedral Lattice Architecture".

The following colleagues have contributed to parts of this thesis and the related publications: Dr. Johannes Scheiger (planning of the experiments, RAMAN measurements, CLSM, writing and proof-reading of the publication), Dr. Yanchen Wu, Dr. Fei Wang, and Prof. Britta Nestler (fluid simulations and analysis, writing and proof-reading of the publication); Dr. Michael Eigenbrod and Prof. Stefan Hardt (fluids and interfaces theory, proof-reading of the publication); Dr. Chantal M Kurpiers and Prof. Ruth Schwaiger (mechanical tests and analysis, writing and proof-reading of the publication); Dr. Ya-Yun Tsai and Prof. Shu-Wei Chang (mechanical simulations, writing and proof-reading of the publication); Stefan Heißler (RAMAN measurements); Maxi Hofmann (mechanical tests), and Carmen M. Rodrigez (laser optical microscopy).

The results of the work were partially published in the following articles:

• 3D-printed inherently porous structures with tetrahedral lattice architecture: experimental and computational study of the mechanical behaviour. M. Kuzina et al. Macromolecular Materials and Engineering, 2023

• Organogels versus Hydrogels: Advantages, Challenges, and Applications. M. Kuzina et al. Advanced Functional Materials, 2023

• Liquid Wells as Self-Healing, Functional Analogues to Solid Vessels. J. Scheiger, M. Kuzina et al. Advanced Materials, 2021

Parts of the work were presented at the Materials Science and Engineering Congress 2022 (Darmstadt, Germany).

Hiermit versichere ich, diese Arbeit selbstständig verfasst zu haben, dass ich keine anderen als die angegebenen Quellen und Hilfsmittel benutzt habe, dass ich die wörtlich oder inhaltlich übernommenen Stellen als solche kenntlich gemacht habe und die Satzung des KIT zur Sicherung guter wissenschaftlicher Praxis in der jeweils gültigen Fassung beachtet habe.

Karlsruhe, den 10.03.2024

I hereby affirm that I have fully independently composed this work, that I have used no sources or aids other than those specified, that I have identified literally or conceptually quoted intellectual property as such, and that I have committed to the current regulations of KIT regarding good academic practice.

Karlsruhe, 10.03.2024

Table of Contents

1 Introduction

Liquids play an essential role in shaping our world and form together with solids and gases three main aggregate states of the matter. What sets the liquid apart from other types of matter is the ability to flow and adapt to the shape of their container, making them unique and versatile as carriers, reaction volumes, or functional components themselves. Under certain conditions, almost every existing material can obtain liquid state, allowing for diverse spectrum of physical and chemical properties of liquid systems. Due to suitable physical conditions, liquid state is abundant on Earth, starting from the main and most common liquid, water, which covers almost three-quarters of the Earth and represents a perfect example of liquid matter being a building block for millions of materials.

Since the early ages of science, liquids played a vital role in the creation of new materials. Liquids are exemplary reaction mediums, allowing for the mixing of hundreds of components and chemical reactions, they also serve as cooling and heating volumes, lubricants, and solvents in research and industrial processes. Due to the vast range of properties, liquids can play opposite roles in various processes, being able to act as dielectric and cooling insulators in liquid transformers (e.g., mineral, silicon oils) and transferring energy as liquid electrolytes in fuel cells and batteries (e.g., salts dissolved in aqueous or organic solvents, or ionic liquids).

In all areas of the modern world, be it construction, medicine, automatics, electronics or the art industry, there has been a continuously increasing demand for better, more versatile functional materials as well as new generations of multi-materials with multiple functional components. Yet, there is a large unexplored potential laying in the properties range of liquids that can be used for constructing new materials in combination with other developed materials and methods, such as liquid-infused materials, structured liquids, all-liquid systems, liquids as morphology forming components, later eliminated to create intricate porous materials. Therefore, it remains important to deepen our knowledge about the interaction of liquids with other materials and utilize them for solving practical challenges of modern materials science.

1.1 Fundamental properties of liquids

1.1.1 Polarity

The polarity of the liquid is one of the most crucial parameters that impact a large range of its functional properties, including miscibility with other liquids, solubility and dispersibility of other compounds,[1,2] wetting,[3] diffusion,[4] formulation stability[5] and emulsification,[6] and many other processes. Polarity arises from an uneven distribution of electrons between atoms

in a molecule, resulting in a dipole or bent structure, and influenced by electronegativity disparities and molecular symmetry.[7] Consequently, liquids, especially all common organic solvents, are commonly divided into polar and non-polar.

In chemical processes, solvent rarely plays a "passive" medium role. The polarity of the solvent can have a large effect on many, often connected, parameters, such as reaction rates, equilibrium constant and stability of intermediates and products, e.g. by solvation of reaction species or energy adsorption effects.[8–11] It is, however, important to note that the reaction kinetics, especially in the case of chain polymerization reactions, can be affected by many more properties of the solvent, including viscosity and density, internal pressure, and others.[12–15] Therefore, experimental screenings of multiple solvents (if possible, supported by computational analysis) are often required to find optimal thermodynamic and kinetic conditions for the reaction or even stability of the system overall.

It is challenging to define the polarity quantitively since it depends on a combination of electrostatic and specific interactions, however, polarity scales can be established empirically through dielectric constant.[16,17] The dielectric constant of a liquid is influenced by its polarity because under an electric field polar molecules align themselves in response, with the positive end of the polar molecule being attracted to the negative electrode, and *vice versa*. Molecules with higher polarity rotate and orient in alignment with the field more easily and have a greater ability to store electrical energy. In turn, non-polar liquids don't have a dipole moment, can't effectively align in an electric field and have lower dielectric constant.[18] The dielectric constant of a liquid is a crucial parameter itself for practical applications, e.g. when choosing liquid media for impregnation in electronics and cables for insulation,[19,20] dielectric cooling,[21,22] cell and liquid manipulation in biomedicine[23–25] or electrolytes in batteries and fuel cells.[26,27]

For liquid-containing materials, the polarity of the chosen liquid media directly determines the applicability of the material and can tailor its stimuli responsiveness, e.g., to electrical or pH-response, chemical reactivity or tolerance, biocompatibility or biological resistance, which makes solvents powerful and functional tools in materials science (**Figure 1**).[28] Gels, the most famous liquid-infused materials, can easily demonstrate the power of the liquid component to enhance or broaden material functionality: hydrogels, as gels based on water, dominate in tissue engineering, bioprinting, or cell culture.[29,30] Together with polar-solvent-based organogels, hydrogels are applied as pH-sensors, conductors, and wearable soft polymer devices. In turn,

organogels that are filled with non-polar solvents are best applied for anti-fouling, anti-acing, antiadhesion, and self-cleaning protective surfaces.[28] Polarity of the solvent also plays a big role in the process of phase-separation, which enables creation of many functional materials: microparticles,[31] micelles,[32,33] membranes,[34–36] or porous polymers.[37,38] Polarity-affected solid-liquid interactions and their applications will be covered in more details in Chapter 1.2.
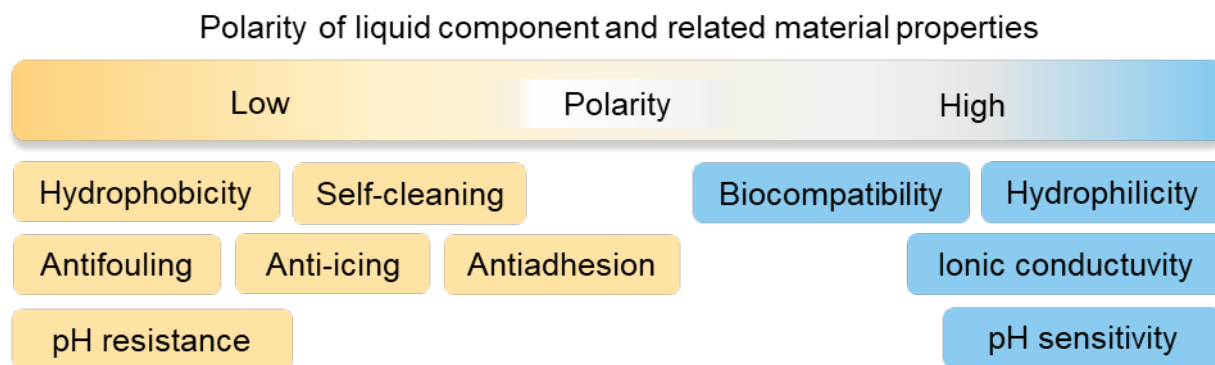
Figure 1: The functional role of liquid polarity in enhancing material behaviour, based on the example of gels. Adapted from KUZINA ET AL. with permission.[28] Copyright 2023, Wiley-VCH.

1.1.2   Temperature range of the liquid state – or the liquid range of solvents

The liquid range directly defines the limitations of the use of the particular liquid, since it refers to the temperature range at which it exists in a liquid state.[39] It differs for every substance and depends on several physical parameters, with primary factors being vapour pressure, intermolecular forces, molecular weight, and molecule structure.

Vapour pressure is a fundamental liquid property referring to the pressure exerted by a vapor in equilibrium with its condensed phases at a particular temperature in a closed system. Liquids with high intermolecular forces, as polar liquids, have lower vapour pressure, as it requires more energy for them to transit into vapour. However, vapour pressure is not a static property and depends on temperature. With increasing temperatures, less energy is needed for liquid molecules to transit into the gas phase, and therefore, vapour pressure increases. Hence, vapour pressure determines many parameters of the liquid, including its boiling point, evaporation rate, and volatility. Liquids with higher vapour pressure have lower boiling temperatures and are considered more volatile. [40,41]

The liquid range of the substance, vapour pressure, volatility rate, melting and boiling points are essential parameters to consider for every application. Vapour pressure is used to calculate thermodynamics of the liquid, and is a vital component of evaporation, distillation and boiling, phase-transition-based processes.[42–45] Melting and boiling points of the liquid can determine

the working range of liquid-containing materials and devices, such as batteries or gels, both at low temperatures and high temperature conditions.[46–51] At the same time, vapour pressure and volatility determine the safety precautions and limitations, defining whether the particilar liquid can be used on air, with the devices sensitive to vapours, at high temperatures, and significantly affect the fabrication strategy, costs and utilization limitations for the future material.

The range of temperatures at which a solvent stays liquid, be it the tendency to evaporate fast under mild conditions, or stay liquid at the extreme high or extreme low temperatures, can be used in multimaterials is a powerful tool in development of phase-transitioning, liquid-exchanging, stiffening-hardening, shape-memory materials.[51–55] By manipulating this range, it is possible to control material properties or its dynamic behaviour, leading to the improved performance or functionality.[56] Thus, volatile solvents can be used to dissolve the initial components of a multimaterial, form the homogeneous liquid multiphase intermediate and, by evaporation, enable the liquid-solid transition and the formation of the solid homogeneous composite, profiting of all its (normally hardly miscible in the solid state) components, as it was recently demonstrated by for the thermal-control polymer-graphene-paraffin-based composites.[57] Volatile solvents are ideal for applications requiring quick drying, making them indispensable in the production of coatings, adhesives, and lightweight composite materials.[58,59] However, with the recently increasing more sustainable approach aiming to create long-lasting biocompatible or biotolerant materials, e.g. gels or other liquid-containing materials, a lot of attention is given to liquids with larger temperature stability and lower vapour pressure. For that, mineral and nature-derived oils,[60,61] silicon oils,[62,63] ionic liquids,[64] green solvents[65,66] have been applied for extraction, sensors, batteries, lubricants, and many other areas and materials as new alternatives to volatile, explosive, and toxic organic solvents.

The strategic selection and application of solvents, based on their evaporation rates and liquid ranges, therefore play a critical role in tailoring the properties of multimaterials to specific needs, paving the way for advancements in a multitude of industries, from aerospace to electronics and beyond.

1.1.3   Surface tension

Liquid surface tension is a fundamental property describing the required force to stretch or break the forces of its molecules acting as a thin film at contact with another phase to counteract external pressure. Based on the strength of their cohesive forces and, thus, surface tensions, liquids could by divided on high- and low-surface-tension liquids. The highest surface tension

(coming from strong hydrogen bonding) is demonstrated by water and is present in hundreds of nature phenomena, such as the formation of the dew or rain drops, capillary, and lotus effects.[67] The presence of polarity in a liquid molecule affects its surface tension with polar liquids tending to have higher surface tensions compared to non-polar. Polar molecules at the surface of a liquid experience stronger intermolecular forces (e.g., hydrogen bonding and dipole-dipole interaction), leading to increased cohesion and surface tension.[68]

Polar molecules at the surface of a liquid experience stronger intermolecular forces (e.g., hydrogen bonding and dipole-dipole interaction), leading to increased cohesion and surface tension. Quantitively the surface tension can be defined by the following equations:

$$\gamma = F \cdot (2L)^{-1} \ (1),$$

were F – is the force that is required to hold the movable surface, and L is the length of the immobile side. The index ½ is reasoned by the existence of two sides (surfaces) in the film, each of them contributing equally to the force. Therefore, surface tension of the liquid is determined solely on its intristic properties.[69]

The ability of water and other liquids to form spherical droplets is caused by the curvature happing due to the pressure differences at both sides of the surface. This ability is used in various material development processes for synthesis of nanoparticles, micelles, and microspheres, allowing for advancement of practical fields, such as cosmetics, drug delivery, nanotechnology, and recently, droplet manipulation.[70–78] On the other hand, low-surface tension liquids, such as hydrophobic organic solvents, mineral or fluorinated oils are essential for the development of protective anticorrosive coatings, anti-stain and anti-biofouling treatment of surfaces.[79–81] Liquid surface tension is one of the key parameters defining spreading and flow of liquids on surfaces and is largely used in wetting theory that will be described in details in Chapter 1.2.1.

1.2 Phenomena of solid-liquid interaction

1.2.1 Wetting phenomenon

The concept of wetting describes fundamental interaction of liquid with the solid surface and is based on the ability of liquid to spread and maintain contact with a solid surface in the presence of a gas phase or another non-miscible liquid.[82,83] On the level of physical interactions, wetting process is determined by the balance between adhesive and cohesive forces. Adhesive forces between the liquid and other materials cause the spreading of the liquid over the surface and adhering to it.[84] Cohesive forces are intermolecular interactions that cause the formation of

droplets and are responsible for liquids balling-up and sliding from surface to minimize the contact. [85] Thus, many fundamental properties of the liquids that were introduced previously, are considered in wetting theory, such as: surface tension, viscosity, polarity.[86] On the other hand, since wetting is a purely interfacial phenomenon, it can be largely influenced by the properties of wetting surface, such as roughness, chemical composition, heterogeneities, as well as presence of other infused liquids or gas molecules.[87,88]

Development of wetting theory started in 1805 by Young and Laplace describing interfacial connections in a three-phase system consisting of a liquid, a perfectly smooth solid, and a surrounding gas. Then, the Young's law has been established, considering three main surface tensions contributing to the triangular balance of forces (surface tensions), liquid-gas (γ_{lg}), gas-solid (γ_{gs}), and liquid-solid (γ_{ls}). The energy minimum equilibrium was described through the angle θ (now commonly called as commonly called as Young's angle (**Figure 2** A and **Figure 2** B), at which a droplet meets the surface in a form of a spherical cap in the following (Young-Laplace) equation[89]:

$$\cos\theta = (\gamma_{gs} - \gamma_{ls}) \cdot \gamma_{lg}^{-1} \ (2)$$

Later, two other models have been proposed, expanding wetting theory to the cases where surface roughness or chemical inhomogeneities had a significant impact, which described wetting closer to how it occurs in nature, where perfectly smooth solid surfaces never exist. Wenzel state, introduced by Wenzel in 1936 (**Figure 2** C), described water droplet that is pinned to the rough substrate, fully penetrating into the rough surface. This additional roughness significantly increased the actual contact area and the contact angle thus could be determined by the equation:

$$\cos\theta_w = r \cdot \cos\theta \ (3)$$

where θ_w is a Wenzel contact angle (apparent contact angle), θ is a Young's angle, and r is a roughness factor.[90,91] Cassie-Baxter model was proposed in 1944 for rough chemically inhomogeneous surfaces, e.g. for the cases when surface roughnesses are filled with air bubbles (**Figure 2** D). According to this theory, to average free surface energies, a droplet will sit on top of the composite surface, with the apparent contact angle determined as:

$$\cos\theta_{CB} = \sigma_1\cos\theta_1 + \sigma_2\cos\theta_2 \ (4)$$

where θ_1 and θ_2 are the contact angles on the two chemically different areas and the σ_1 and σ_2 are the corresponding fractional surface areas.[89,92]
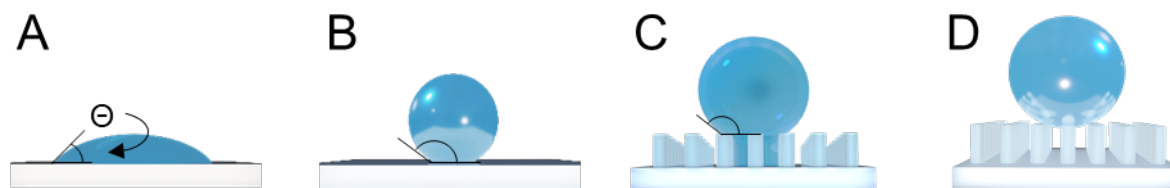
Figure 2. Wetting theories describing the contact angle θ of a droplet on a solid surface. A, B) Young's law of wetting on flat surface: (A) wetting, θ < 90°, (B) dewetting, θ > 90°. C) Wenzel state of a droplet wetting a rough surface. D) Cassie-Baxter state of a droplet wetting a rough surface with air trapped in surface roughnesses.

Measuring the contact angle of a sessile droplet on surface is the main quantitative method of describing surface wettability (**Figure 3**). Contact angle goniometers are used to measure the apparent contact angle of static droplets or contact angle hysteresis, i.e. a difference between advancing θ_a and receding angle θ_r of a droplet when it's tilted or inflated and deflated. Contact angle hysteresis is an important means of assessing the mean roughness or chemical inhomogeneiety of the sample. The lower is the difference between these values, the more homogeneous is the substrate.[93,94] Usually the observed apparent or static contact angle is an intermediate between advancing and receding angels. Based on the value of the apparent contact angle, the surface can be described as hydrophilic (θ < 90°), hydrophobic (θ > 90°), and superhydrophobic (θ > 150° or $\theta_a - \theta_r$ < 5°).
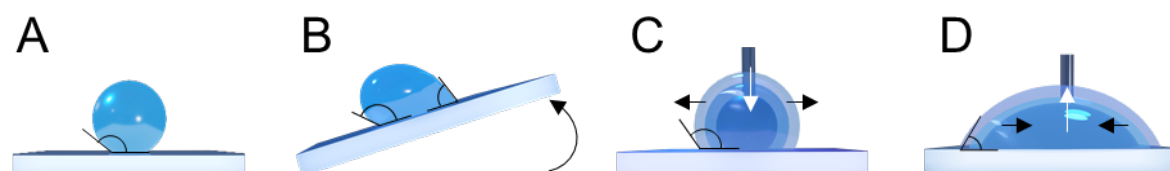
Figure 3. Conventional methods of measuring droplet contact angle on a solid surface. A) Static contact angle, B) Advancing (left) and receding (right) contact angle on a tilting plate, C) Advancing contact angle while inflating a sessile drop, D) Receding contact angle while deflating a sessile drop.

With the increasing complexity of functionalized anisotropic, chemically or mechanically patterned surfaces, as well as when describing wetting of natural materials, which are never fully isotropic, Young, Cassie-Baxter and Wenzel state do not fully apply. Comprehensive experimental, numerical and simulation methods have been developed recently to capture various droplet equilibrium states, including motion and evaporation on various roughness-induced chemically inhomogeneous substrates.[95–98] Numerical studies and experimental investigations have contributed to better understanding of three-dimensional droplet shapes on chemically patterned surfaces.[99–104] Various methods have been established to simulate the equilibrium droplet shapes including Cahn-Hilliard,[105–107] level set,[108] volume of fluid,[109] lattice Boltzmann,[110] Allen-Cahn phase-field model,[111] and others. However, there still

remains a need for theoretical frameworks to fully describe liquid behaviour on complex, inhomogeneous surfaces.

In 2011, a separate research direction for surfaces with special wettability has been introduced by TAK-SING WONG, JOANA AIZENBERG ET AL, called liquid-infused surfaces.[112,113] It refers to surfaces that have been treated or engineered to be infused or coated with a liquid lubricant, e.g., oil. The lubricant (non-volatile, completely wetting the surface liquid) is infused into the solid substrate and eliminates the contact pinning line and contact angle hysteresis of the immiscible droplets.[114] Moreover, since the droplet sits on a thin lubricant layer instead of the solid substrate, the contact line and apparent contact angles of the sessile droplet couldn't anymore be described by Young, Wenzel or Cassie-Baxter state. In this case they would be largely influenced by the surface tensions of both liquids and lead to a formation of the wetting ridge or even (what is undesirable) the complete cloaking of the droplet by the thin layer of the lubricant (**Figure 4**).[113,115–117]
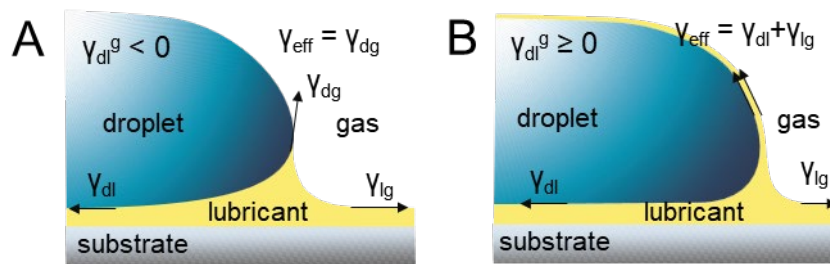
Figure 4. Wetting of the lubricant-infused surface by the immiscible droplet by the formation of the wetting ridge without and with a cloaking effect

The wetting ridge, as well as the cloaking phenomena on liquid-infused substrates is caused by the balance of the interfacial tensions of two liquids and the gas phase, and therefore can be described similarly to Neumann's triangle of forces in case of a liquid floating in a bulk liquid phase. Then, three interfacial forces would define the balance equation: γ_{dl}, γ_{lg}, and γ_{dg}, where "dl", "lg", and "dg" are interfacial forces between droplet and lubricant, lubricant and gas, and droplet and gas, accordingly. Then, if the interfacial energy of the combined droplet-lubricant and lubricant-gas interfacial forces is less than the interfacial energy of the droplet-gas interface, the effect of the wetting ridge will form (**Figure 4** A). Otherwise, the lubricant will cloak the droplet. i.e. spread all over its surface in a form of a thin (~1-100 μm) film (**Figure 4** B). This balance can be thus formulated as a following equation:

$$\gamma_{dl}{}^{g} = \gamma_{dg} - \gamma_{dl} - \gamma_{lg}. \text{ (5)}$$

Then $\gamma_{dl}{}^g < 0$ is a condition for a wetting ridge, and $\gamma_{dl}{}^g \geq 0$ – for cloaking. The apparent contact angle for a sessile droplet on a lubricant-infused surface could be approximated analogously to Young's contact angle (2) but using the effective interfacial force γ_{eff}:

$$\cos \theta_{app} = (\gamma_{gs} - \gamma_{ls}) \cdot \gamma_{eff}, \quad (6)$$

where $\gamma_{eff} = \gamma_{dg}$ in the absence of cloaking and $\gamma_{eff} = \gamma_{dl} + \gamma_{lg}$ in case of cloaking (as illustrated at **Figure 4**). However, such approximation would only be applicable for a negligibly low wetting ridge or cloaking.[115] Additionally, many other co-existing factors can make experimental and theoretical definition of apparent contact angle unreliable, such additional influence of the surface roughness and hydrophobicity, dynamic nature of the fluid-fluid surface tensions. Therefore, measuring the sliding angle instead of a static apparent angle remains a standard way to prove the lubrication effect and compare different lubricants and surfaces.[118–121]

Lubricants are extremely important for creating long-lasting materials able to function well despite extreme conditions, such as high and low temperatures, humidity, harsh frictions, and so on. A popular direction for the application of lubricants is to protect surfaces, creating anti-acing, anti-corrosion, anti-biofouling properties.[113] Another example of a functional role of a lubricant is to enable easy liquid-manipulation due to a low-friction surface created by the lubrication layer.[120] Additionally, lubricants can act as coolants to dissipate heat generated during operation.[122] Various liquids can act as lubricants, including natural and mineral oils,[123,124] derived from oils esters,[125–127] ionic liquids,[128] or hydrophilic mixtures.[129]

1.2.2   Swelling

If wetting describes liquid-solid interaction solely on the interface, swelling is a bulk phenomenon of a liquid infusing into a solid material causing its expansion locally or throughout its volume. The importance of swelling is easy to demonstrate on one of the most important modern multicomponent materials, gels. Swelling is a distinctive property of gels giving them a unique combination of properties of solid and liquid components, e.g. tunable visco-elasticity, the ability to dynamically respond to various stimuli or retain up to 99% of liquid phase structured in 3D space.

Theoretical concept of swelling was developed by Paul G. Flory and Alfred J. Rehner in the 1940s. According to Flory-Rehner theory, when an elastomer is introduced to a solvent, the solvent penetrates the polymer network, causing entangled polymer chains to separate and create free volume within the polymer structure. This free volume allows solvent molecules to diffuse throughout the polymer network, leading to an increase in weight and volume of the

elastomer.[130] Swelling causes a change of free energy that can be calculated as a sum of free energy of mixing and free energy of elastic deformation. Swelling equilibrium is reached, when the osmotic pressure of the solvent molecules that promotes swelling, is balanced by the elastic forces limiting the network chains extension. The maximum degree of swelling is determined by two major factors: 1) how soluble the un-crosslinked polymer would be in the respective solvent (also known as the polymer-solvent Flory-Huggins interaction parameter χ) and 2) the length and molecular weight of the chains between cross-linking points (less swelling ability with higher cross-linking). These factors are considered in the Flory-Rehner swelling equilibrium equation:

$$-[\ln(1 - \varphi_2) + \varphi_2 + \chi \cdot \varphi_2{}^2] = \rho_2 \cdot V_1 \cdot M_c{}^{-1} \cdot (1 - 2M_c \cdot M_2{}^{-1}) \cdot (\varphi_2{}^{0.333} - 0.5\varphi_2), \quad (7)$$

where φ_2 is the volume fraction of polymer in the swollen state, V1 is the molar volume of solvent, ρ_2 is the density of the polymer, M_2 is the polymer molar weight, and M_c is the molar weight of the chains between cross-linked. Therefore, according to the Flory theory, the choice of the solvent plays a large role in the swelling process, as its polarity and viscosity would determine the ability of the polymer network to mix or dissolve in it. Apart from that, the amount of the solvent plays a big role in the kinetics of swelling, so swelling tests are always carried out in the excess of the respective solvent to avoid reaching the equilibrium prior to the full swelling.
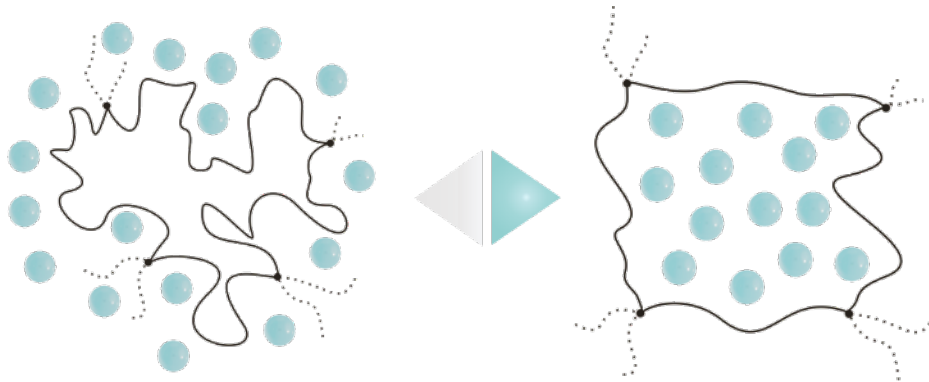
Figure 5. Illustration of the reversible swelling process. Swelling consists of two processes: diffusion of the solvent in the free volume of the polymer network and extension of the polymer network until the swelling equilibrium is reached.

Flory-Rehner theory has become a base for theoretical description of swelling processes. It has been later extended to the ionized polymers by Tanaka *et al.*[131], applied to thermo-responsive phase transition polymer gels by Hirotsu *et al*,[132] used for studying the effect of monomer concentration,[29,133,134] applied to systems of co-polymers,[135–137] micro-[136,138] and macrogels,[139–141] and to quantify various influencing parameters, such as pH, temperature,

external stress, and others.[134,142–146] However, much of the theoretical works are only applicable either to perfect networks, e.g. networks with constant chain length between cross-links and very regular structure, and their application to each particular network is limited by the scarce amount of precise measurements possible to conduct for the cross-linked polymer network. Later developed complex simulations using Monte Carlo method[147–149], finite element modelling, and other methods enable more realistic theoretical investigation of the swelling behaviour, but still have to be adjusted when applied to particular networks and solvents due to the high amount of influencing parameters.

For a respective gel-solvent pair, there are three important parameters that illustrate swelling behaviour and can be investigated quantitatively: swelling ratio or swelling capacity and swelling rate. The swelling capacity of the gel in the given moment is quantified by its mass (Q_m) or volume (Q) swelling ratio by the following proportions between its dry and swollen states:

$$Q_m = (W_{swollen} - W_{dry}) \cdot W_{dry}^{-1} = M_{solvent} \cdot M_{polymer}^{-1} \text{ (8) or}$$

$$Q = V_{swollen} \cdot V_{dry}^{-1} = (V_{solvent} + V_{polymer}) \cdot V_{polymer}^{-1} = 1 + Q_m \cdot \rho_{polymer} \cdot \rho_{solvent}^{-1}.^{[150]} \text{ (9)}$$

Then, swelling curve resulting from swelling ratios measured multiple times in time intervals until full swelling is reached, can be further characterized using the Voigt viscoelastic model. This method is frequently applied to model the creep and relaxation behavior of polymers and also allows for quantitative analysis of the swelling rate. The Voigt model is formulated based on the following equation:

$$Q(t) = Q_{max} \cdot [1 - \exp(-t \cdot \tau_s^{-1})], \text{ (10)}$$

where τ_s is a swelling time constant or rate parameter that gauges the resistance to solvent diffusion, and Q_{max} is a power parameter, representing the resistance of the polymer network expansion and the equilibrium degree of swelling.[151,152]

To sum up, swelling is a phenomenon that represents the unique diffusion- and free energy-determined interaction of various materials, but especially gels, with fluids. This ability to absorb, store, release, and exchange fluids enables materials to serve as reservoirs or barriers and creates special synergy between liquid and solid components in functional visco-elastic materials. Swelling processes are essential in drug discovery, water purification, sensing, environmental protection, and many other areas. The unique properties of gels as functional materials will be further highlighted in Chapter 1.3.2.

1.2.3 Phase-separation

Phase separation, also known as demixing, refers to the occurrence when substances separate from a mixture or solution into multiple distinct phases. This process is widespread in numerous natural, industrial, and scientific processes, playing a crucial role in fields like oil recovery,[153] inject printing, nanosynthesis, various forms of extraction and purification, polymerization, and various biological processes, such as autophagy[154] or formation of membraneless organels assemblies. [155–157] Liquid-liquid phase separation (LLPS) represents a fascinating process where a homogenous liquid naturally segregates into two distinct liquid phases, each with different concentrations of components. A simple example of a LLPS process would be the everyday occasion of water-oil separation on droplet emulsion in another liquid. This phenomenon is commonly seen in soft matter and natures, for organic molecules, and proteins, but also occurs in systems containing polymers and therefore is widely used for the materials' engineering. Relevant for the objects of this thesis might be the polymer-diluent phase separation, that can occur in gels or porous polymers.[158]

At a specific temperature (T) and pressure (P), the conditions for miscibility within a polymer-diluent system can be defined by the mixed Gibbs free energy (ΔG_{mix}), the relationship between its second derivatives, and the volume fraction of the polymer (φ_p).

$$\Delta G_{mix} < 0 \ (11)$$

$$\left(\frac{\partial^2 G_{mix}}{\partial \varphi_p^2}\right)_{T.P} > 0 \ (12)$$

$$\text{where } \Delta G_{mix} = \Delta H_{mix} - T\Delta S_{mix}. (13),$$

ΔH_{mix} represents the enthalpy of mixing, and ΔS_{mix} represents the entropy of mixing.
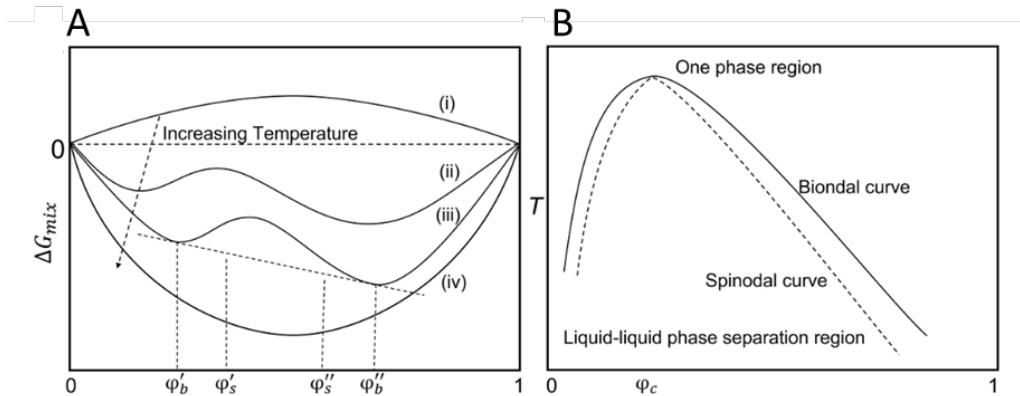
Figure 6. Energy landscape of LLPS in polymer-diluent systems. Gibbs free energy ΔG_{mix} of mixing as a function of the volume fraction of polymer. (i) immiscible, (ii) and (iii) partially miscible, (iv) miscible. (b) Temperature-composition phase diagram for a polymer-diluent system.[158] Reproduced from the work of J.XU ET AL. with permission. Copyright 2023, Elsevier B.V.

The system is categorized into three states based on Gibbs free energy, ΔG_{mix}: complete immiscibility ($0 < \varphi_p < 1$), partial miscibility (marked by a negative ΔG_{mix}'s second derivative), and full miscibility across all compositions. In the context of partial miscibility, as demonstrated in **Figure 6** A, the system achieves homogeneity only under certain compositions and temperatures. Here, a negative second derivative of ΔG_{mix} indicates instability, leading to phase separation, while positive values indicate stability against minor concentration changes. This separation results in a polymer-rich and a polymer-poor phase in equilibrium.[159] The role of temperature in this dynamic is critical, with higher temperatures facilitating solvation and lower temperatures promoting separation due to diminished polymer-diluent interactions. The temperature-composition phase diagram presented in **Figure 6** B, with its binodal and spinodal curves, outlines the stability, metastability, and instability regions. Specifically, the region below the spinodal curve, where $\left(\frac{\partial^2 G_{mix}}{\partial \varphi_p^2}\right)_{T.P} > 0$, indicates an unstable system prone to spontaneous phase separation, a phenomenon termed spinodal decomposition.[160,161] The metastable region between the binodal curve and the spinodal curve is characterized by the absence of spontaneous LLPS. [158,161]

Until now the theory about the LLPS process can only limitedly describe the interactions in complex liquid-polymer and polymer-polymer systems. It is important to notice that the phase separation described in the LLPS process is a reversible process, while the polymerization-induced phase separation is not purely a physical phenomenon and is caused by the complex chemical reaction of growing and cross-linking polymer chains. Therefore, such systems are difficult to describe by traditional physics theory and have merely been explained by combined computational and experimental efforts, taking into account many parameters influencing the separation process, such as multi-component diluent systems, chemical cross-linking, solvation effects and electrostatic interactions, solubility of the components, side reactions, and so on.[162,163]

1.3 Liquids made to order: functional role of liquids in 2D and 3D

The full potential of liquids can only be realized by not limiting their within the traditional solid-wall containers but through mastering their manipulation in shape, volume, and integration into miniaturized devices, on-chip systems, and other materials. This exploration extends to the innovative introduction, capture, or release of liquid phases from various materials, leveraging their inherent ability for dynamic shape transformation.

To accommodate such precise control over liquid structuring, a range of tools has been developed, from basic fluid microchannels in polymer or glass molds to more sophisticated droplet-based assay platforms, droplet-in-fluid systems, and fluid-wall channels. These innovations enable the miniaturization of large-scale laboratory and manufacturing processes—such as synthesis, extraction, and analysis—to nanoliter volumes, accelerating these processes significantly. Such platforms provide precise control over synthesis conditions and the shape, size, and composition of products in a small volume, automated in a robotized manner.

The structuring of liquids, specifically the kinetic trapping of liquids in nonequilibrium shapes across liquid-liquid, liquid-solid, and liquid-gas systems, opens new avenues for various applications. However, manipulating low-surface-tension liquids on surfaces, critical for micro-scale lab-on-a-chip applications, presents challenges. Despite these hurdles, notable achievements have been made in the handling of low-surface-tension liquids on chips.

As the complexity of liquid-handling and liquid-infused systems increases, so does the need for a deeper understanding of these systems' fundamental principles. This includes exploring liquid-infused systems and the engineering of porous systems through the elimination of the liquid phase, areas that are often overlooked. Addressing this gap requires comprehensive numerical and simulation studies to elucidate the physicochemical properties and hydrodynamics of a wide array of fluids in contact with different phases. This refined approach to liquid manipulation in 2D and 3D not only broadens our understanding but also paves the way for innovative applications, encouraging a shift from traditional liquid use towards a future where fluid dynamics play a central role in technological advancements.

1.3.1 Liquid manipulation on surfaces and by other liquids

The kinetic trapping of liquid droplets and channels at solid-liquid of liquid–liquid interfaces in on-chip and on-surface liquid-handling platforms show great promise for various miniaturized and high-throughput biomedical, chemical, energy and material applications. Advancing the technology for manipulating liquids in smaller volumes, often combined with flow systems and stimuli responsiveness, is guided by an important need in science for accelerating research progress and harvesting larger amounts of experimental data by utilizing new, more sustainable and automatized platforms.[164–166]

Recent progress in the creation of functional surfaces and the theory of droplet dynamics has enabled the control of droplets on surfaces through the engineering of surface wettability gradients or the application of external stimuli.[164,167–169] Different platforms have been

developed for miniaturized liquid-handling in the last twenty to thirty years. They can be very generally divided on droplets-on-surface systems and microfluidic devices (**Figure 7**). For the single droplet manipulation, various anisatropically structured, patterned, chemically coated or stimuli responsive surfaces have developed (**Figure 7**, A-D). These platforms are promising for applications where the mobility of single droplets combined with the open systems is advantageous. Among a wide range of cutting-edge applications that can very well illustrate the innovative role of liquid phase manipulated in droplets, are chemical analysis,[170] in situ detection,[171,172] biological screenings,[173] miniature reactors,[174,175] dropwise condensation for energy harvesting and transfer systems,[176–178] liquid robots,[179,180] and many more.[181–183]

Followed by the idea of the increasing the throughout and using the droplets as mini reaction chambers, droplet-based microarray assays have appeared (**Figure 7** E). This invention has a potential to cover many crucial needs in modern science, such as reduction of costs, automation and integration of multi-step manufacturing processes on one platform, rapid prototyping, multiplexing capability, and others.[184,185] A great example to illustrate its revolutionary potential would be already existing protocols enabling high-throughput synthesis, screening and analysis of thousands of new drugs, followed by the high-throughput cell culture possible on the same platform.[186][186] The limitation of such arrays includes the limited applicability of LSTLs, high cost of the array platforms, and difficulty to introduce flow, component separation and exchange, purification, and other processes often crucial for the full transfer of bulk set-ups on the droplet array. However, already with the limited integration and automatization, they have greatly accelerated modern research in chemistry and biology liquid systems.
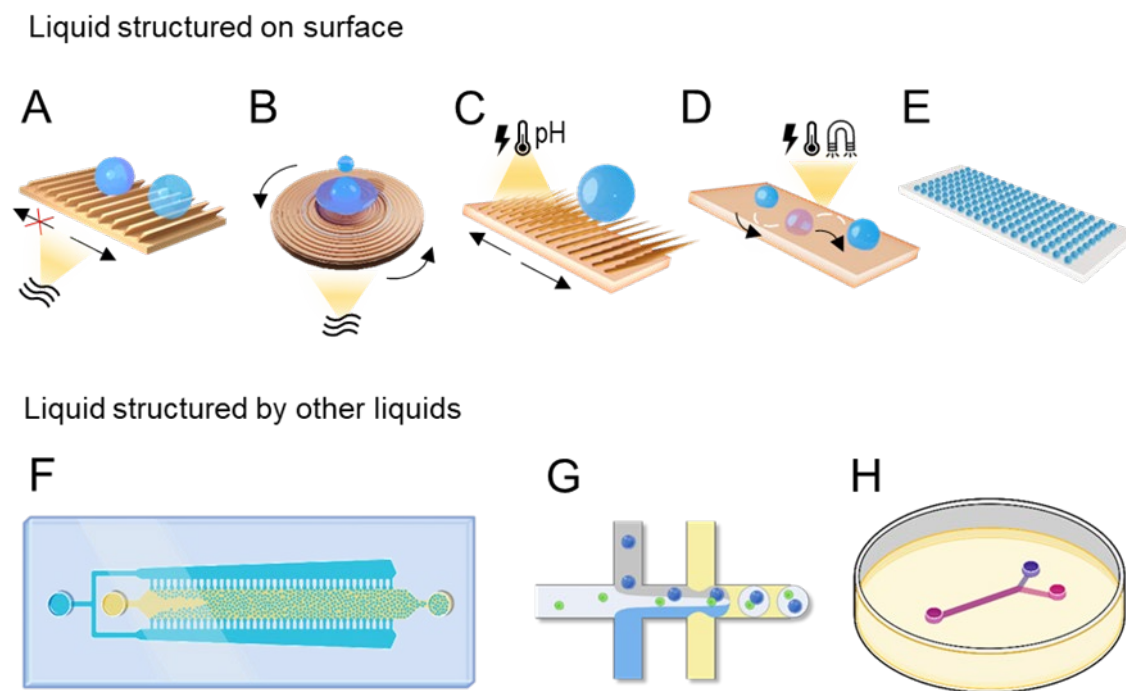
Figure 7. Schematic representation of various liquid manipulation platforms. (A-D) Single droplets on physically or chemically structured surface, often combined with applied external stimuli for the directed movement. (E) Droplet assay platforms. (F-H) Liquids structured by other liquids in various microfluidic divices.

As a next generation after the closed solid channel microfluidics, various liquid-in-liquid flow systems have created, in which one liquid is used to shape another or multiple liquids. This approach is represented by droplet-in-fluid, multiple-fluid-droplets, and fluid-wall channels and is referred to as multiphase microfluidics (**Figure 7**, F-H).[187,188] In such systems, the ultra-fast flow and high automatization potential could reproduce large laboratory and manufacturing processes in one chip, such as, e.g., synthesis, extraction and analysis of compounds. Hence, complex, time- and resources-demanding set-ups can be scaled down to nanoliters and speeded up to minutes. However, despite clear advantages, such systems also possess drawbacks similar to the ones of droplet microarrays, such as limited integration abilities, incompatibility with some synthesis and analysis methods, and so on. Therefore, a choice out of many liquid-manipulation approaches is needed to optimize different processes .

The easiest to manipulate in droplets liquid is water, as it both readily forms droplets down to sub-micrometer size on air, surrounded by other liquids and on various surfaces.[189] High surface tension of water and other polar liquids allows them to easier form droplets or channels surrounded by oil in microfluidics or on surfaces, being able to adhere to surface in complex continuous shapes and forming little microreactors. While water-handling systems have seen extensive development and application, the widespread utilization of hundreds of organic

liquids has been comparatively limited, although the importance of organic liquids in chemical and materials science processes is immense and requires miniaturization and automation. For manipulating oils in microfluidics and droplet arrays, omniphobic or oleophobic plain or micro-structured surfaces, as well as oil-in-water droplet microfluidics are mostly applied.[190] Furthermore, other approaches to form liquid channels on surfaces and by other liquids, should be developed. For example, the ability of water to form strong bonds with patterned substrates, and therefore acting as a barrier to confine other liquids, has not been fully explored. This property could significantly reduce the reliance on solid containers in microfluidic applications and introduce a new dimension to the fundamental study of liquid-liquid interfaces. At the same time, with the further increasing complexity of developed liquid-handling platforms, there is a remaining lack in theoretical and computational methods to describe such kinetically-trapped multi-component equilibria systems. Therefore, continuous numerical and simulation investigations are required about physicochemical properties and hydrodynamics of thousands of existing fluids in contact with each other, gas and solid phases on surface and on-chip.[111,191,192]

1.3.2 Liquids captured in 3D networks: gels

Liquid infused in the solid materials can enhance their functionality by providing or contributing to their reduced friction, mechanical robustness, repellence towards ice and biofilms, and many other properties that can be tailored for specific applications.[193–195] Among the materials benefiting from their liquid component, gels stand out due to their unique semi-solid visco-elastic nature, where properties addressed by a liquid can be much more defining the behavior, than those of their solid component, a three-dimensional colloidal or macromolecular network. The combination of high solvent content, tunable properties, adaptability and stimuli-responsiveness gels apart from other materials. Gel structure makes it possible for many gels to closely mimic natural biological tissues, making them particularly valuable in biomedical engineering and regenerative medicine. In addition, their ability to undergo significant deformation without rupture is beneficial for applications such as soft robotics or cushioning materials that require materials that can withstand mechanical stress. In this chapter we will these unique multifunctional materials, their classification, and the role of liquids in gel functionality.
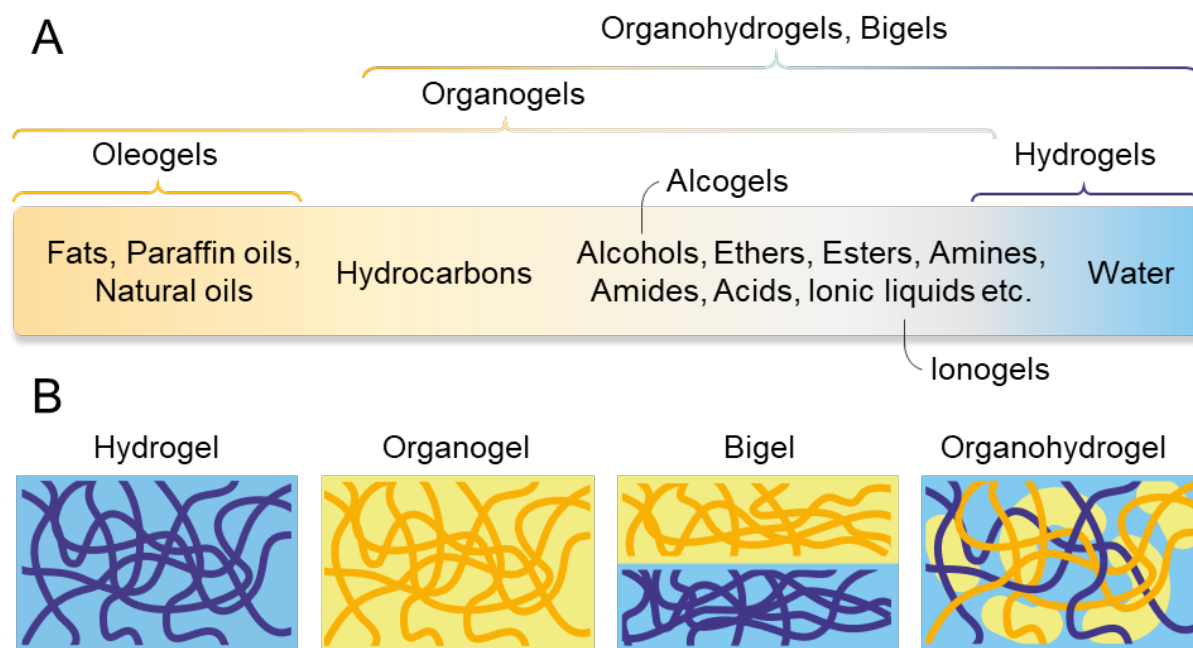
Figure 8. A classification of gels based on their liquid component (A) and overall composition (B). Adapted from KUZINA ET AL. with permission.[28] Copyright 2023, Wiley-VCH.

A gel is a non-fluid colloidal or polymer network that is expanded throughout its whole volume by a fluid (IUPAC Gold Book).[196] Gels have the capability to absorb and retain a significant amount of the fluid phase—up to 99%—and can also absorb and release various substances. Additionally, they are responsive to different physical and chemical changes, including alterations in temperature, light exposure, pH levels, and mechanical stress. The wide array of functionalities that gels possess stems from the combined characteristics of the organic liquid and the gel-forming agents. With a vast selection of liquids and gelators available, gels can be customized to exhibit diverse properties and functions. Based on their liquid component, gels can be divided on hydrogels (the main component is water or aqueous systems), organogels (gels based on organic liquids) – and various hybrid forms or subtypes of those two (**Figure 8** A). For example, oleogels and alcogels are swollen in oils and alcohols, respectively. The gels that have both hydrogel or organogel components are called organohydrogels or bigels. The difference between these types of hybrid gels comes already not from the liquid phase but from the way the networks are connected (**Figure 8** B), for bigels one can distinct the hydrogel part from the organogel network, while for organohydrogels, these networks are interconnected or meshed within one composite.[28,56]

When designing the gel system, solvent choice is pivotal, influencing gelator selection, gel formation, and post-gelation characteristics. Solvent structure can affect gelation by either facilitating initiation[197] or hinder gelation stability.[198–200] The gelation process relies on non-

covalent interactions such as van der Waals forces and hydrogen bonding, with optimal gelation achieved in solvents that are miscible with all gelation components yet minimally interferes with the gelator while the polymerization process occurs. As an example, ZHU ET AL. showed for the supramolecular gels that strong gelator-solvent interactions lead to unstable gels with lower gelation capacity.[201] Thus, selecting the right solvent environment is crucial for designing effective gels.

Solvent choice also impacts polymer network formation, affecting factors like co-monomer reactivity ratios in copolymerization,[202–205] known as the "bootstrap" effect. However, this effect varies with the copolymerization system [202] and must be assessed for each new solvent component. In the post-gelation, gels act as quasi-solid materials with properties influenced by the solvent's polarity, affecting the gel's hydrophilicity, hydrophobicity, or amphiphilicity.[206–208] The interaction between the solvent and the 3D network determines the gel's surface and bulk properties, including wettability, substance affinity, stimuli responsiveness, and stability. Different applications necessitate specific solvent polarities for optimal performance. Hydrogels are well-suited for the applications where e.g. biocompatibility and pH-sensitivity are required,[209,210] whereas organogels extend functionalities to hydro- and omniphobic surfaces using non-polar, low-surface-tension liquids, enabling self-cleaning and anti-fouling capabilities (**Figure 9** A).[211–217]

Thermal and environmental stability, along with dynamic properties of the gel are significantly influenced by the solvent (**Figure 9** B). Low boiling point solvents may cause gel shrinkage due to evaporation,[218] whereas high-boiling-point solvents enhance temperature stability.[219] Solvent freezing points are critical for maintaining visco-elasticity and ionic conductivity in low temperatures,[220–222] with organogels showing remarkable functionality under extreme conditions.[223–228] Binary solvent systems, like water–organic liquid mixtures, offer enhanced environmental stability by preventing crystallization and maintaining mechanical properties even at low temperatures, exemplified by the use of water–dimethyl sulfoxide mixtures for organogels.[224,229] The thermal stability of organogels can be tailored through the selection of solvents with specific boiling points.[50,230] Furthermore, by incorporating lubricants, organogels can be engineered to exhibit properties such as resistance to ice formation[231,232] and anti-biofouling capabilities, [81,233] making them not only thermally but also environmentally more resilient, than hydrogels.
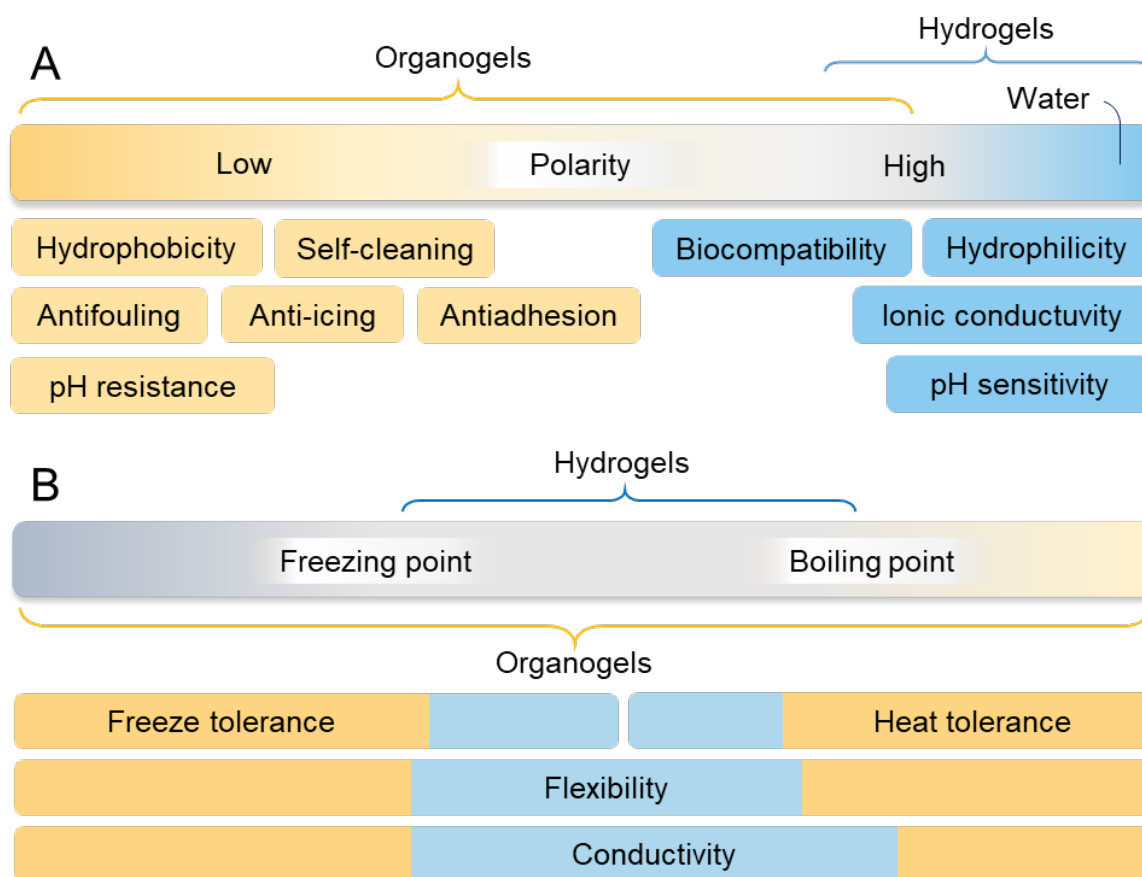
Figure 9. Organogels versus hydrogels. (A) Comparison of their application areas linked to the polarity range of the liquid component (A) and (B) of their functionality range depending on the liquid range of the liquid solvent. Adapted from KUZINA ET AL. with permission.[28] Copyright 2023, Wiley-VCH.

Gels have already been recognized as multi-functional materials that possess significant potential for enhancement and application across a wide spectrum of fields, owing to their adaptable properties facilitated by the extensive range of liquids and gelators available. The newly developed gels, especially organogels exhibit continuously advanced properties, including improved mechanical and environmental stability, conductivity and detection ability, function at a wider operational temperature spectrum, underscore the necessity for increased research efforts. Despite the discovered features, there exists a noticeable gap in both theoretical and practical studies concerning various organogel systems, highlighting the need for further exploration and development. The real-life application of organogels is also significantly slowed down by the challenges related to sustainability, particularly concerning toxicity and recyclability. Addressing these challenges through the development of organogels using environmentally friendly solvents and creating dynamic, degradable, and reusable polymer networks are seen as viable solutions. Efforts should be directed towards the creation of cost-effective fabrication techniques, the discovery of novel gelators that interact specifically with solvents, and the application of organogels in domains presently dominated by hydrogels, such

as implants, drug delivery systems, biomedicine, and biomimetic materials. Moreover, the potential integration of organogels with hydrogels to form multifunctional materials showcasing diverse response behaviors warrants investigation. The exploration into the use of more organic liquids alongside bio-derived gelators for gel formation, aiming to maintain their functionality while incorporating functional nanoparticles, presents an exciting avenue for future research. Furthermore, the integration of computational analysis with empirical experimentation is crucial for understanding the interactions within specific gelator systems and organic liquids, which will aid in the intelligent design of gel networks and the effective inclusion of additional components. In light of the current findings and potential avenues for research, it is evident that gels represent a versatile and expansive class of gels, capable of unlocking the full potential of soft, liquid-infused multifunctional materials. Therefore, a concerted effort in the study and development of new generation of organogels is imperative for advancing their application and overcoming the limitations existing conventional materials.

1.3.3 Liquid as a morphology architect: polymerization-induced phase separation

The distinctive property of liquids of facilitating a phase separation, which was briefly discussed in Chapter 1.2, is also an integral factor in the polymerization-induced phase separation phenomenon.[234,235]
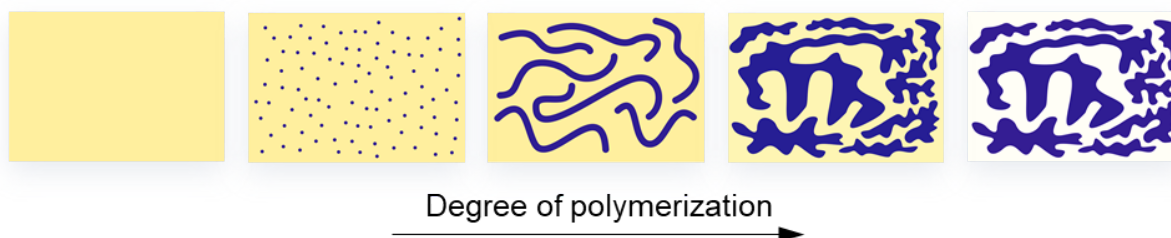
Figure 10. The schematic process of polymerization-induced phase separation..

Phase separation happens when a homogeneous mixture splits into two or more distinct phases due to variations in their properties such as polarity, viscosity or solubility. With regards to polymer-induced phase separation, usually, the liquid component acts as a solvent for monomers and initiators before the polymerization starts (**Figure 10**). Further during the polymerization process, the growing and cross-linking oligomer chains become immiscible with the liquid phase and form the nucleation centers. As the solid component grows, the mobile liquid porogen phase serves like a template that facilitates the structured porous polymer's

development.[162] Consequently the formed polymers, after the removal of the liquid porogen, exhibit porous morphology across their volume.

This versatile method is compatible with various polymerization systems, including e.g. step-growth,[236] free radical,[162,234] or seeded-emulsion[237] polymerization mechanisms. Furthermore, it offers convenience of designing advanced tailored materials by a precise manipulation of material morphology through a fine-tuning of the components, solvents, monomers, and was shown to be compatible with various fabrication methods, one of the most important of which is 3D-printing.[162] This powerful structuring tool combined with polymerization-induced phase separation was only recently demonstrated but has already shown its tremendous potential to be applied in cell culture platforms,[162] 3d-patterning,[238] electrical conductivity and photodetection,[239] superhydrophobic surfaces and bulk objects,[240] and will attract more and more research and industrial attention in future. Important challenges remain yet to be investigated and overcome, such as poor mechanical stability of the currently existing materials, limited amount of existing polymerizable inks, or low level of structure-property relationship understanding. Nevertheless, already in its early stages, this method is a clear demonstration of a powerful role of liquids in modern material science to be a structuring tool for solid materials.

2 Motivation

The aim of this work was to explore and widen the functional role of liquid phase in new materials and materials systems design, including: liquids on chemically patterned surfaces, 3D-printed organic liquid infused expanded polymer networks (organogels), and 3D-printed inherently-porous macro-architectured polymer structures.

Consequently, the work was divided in three main chapters, according to three main types of investigated functional materials. In the first part, a liquid analogue to a solid container is introduced, named "liquid wells" and created by pinning water to surfaces with hydrophobic-hydrophilic core-shell patterns and confining various low-surface-tension hydrophobic liquids within the water walls. The second part is dedicated to exploring possibilities of various organic liquids to determine and alter bulk and surface properties of organogels through a printing-drying-swelling process, by which the convenience of fabrication and functionality of the resulting gel is increased. The third part is describing a method of creating mechanically strong inherently porous polymers by utilizing the role of a liquid phase in 3D-printing inks as a main shaping component of the morphology of the 3D-printed porous polymers, through the process of polymerization-induced phase separation.

3 Results and Discussion

3.1 Liquid wells as analogues for solid vessels

Traditionally, liquids are stored in solid containers, but the solid walls do not offer adaptability, self-repair capabilities, and ease of modification. Liquid walls offer a potential solution to these limitations but face challenges in forming free-standing 3D structures. In this study, a liquid analog, named "liquid well," created by tethering water to surfaces with hydrophobic-hydrophilic core-shell patterns, is introduced. These liquid wells can stably contain immiscible fluids, similar to solid walls. Liquid wells can compete with or complement existing confinement methods, such as perfluorinated surfaces, offering unique advantages like self-healing and dynamic behavior, and the ability to be removed and reformed.

This chapter contains the results that have been previously published by SCHEIGER, KUZINA ET AL.[241] This study was conceptualized and executed jointly with DR. J.S. SCHEIGER. Experiments performed by DR. J.S. SCHEIGER include Raman spectroscopy and confocal laser scanning microscopy.

3.1.1 Project Idea and Background

Historically, liquids have been stored, contained and manipulated within the solid walls, including pottery, vases, metal canisters, glass, and many other materials. However, with the development of science and technology, there has been a growing interest in reimagining the boundaries of liquid manipulation and control, particularly when it comes to low-volume liquid handling on surfaces. Such perspective has stimulated significant progress across a spectrum of liquid-handling applications including microfluidic devices,[242] lab-on-a-chip technology,[243,244] repellent coatings,[245] oil-water separation,[246] and the fields of miniaturized chemistry or biology.[247–249] One of the most revolutionary methods of wall-less liquid handling on surface utilized chemically patterned surfaces with hydrophilic-hydrophobic regions that enabled precise spatial confinement of aqueous compartments in the shapes of droplets to channels.[165,166,250–254] The advancement towards omniphobic-omniphilic or superoleophobic patterned substrates has significantly broadened the horizons of liquid confinement, particularly with regard to droplets of low surface tension liquids (LSTLs), elevating the versatility of surface-templated liquid systems.[173] Nonetheless, the development of omniphobic or superoleophobic surfaces often necessitates the deployment of perfluorinated chemicals for surface modification or reliance on lubricant-infused surfaces (LIS), both of which are associated with intrinsic limitations, including environmental concerns and issues related to durability.[121,195] Furthermore, most of on-chip liquid-handling methods tend to be focused on

the manipulation of aqueous solutions, with rare instances of patterned LSTLs reported in the literature.[79,255–258] JOKINEN ET AL. have demonstrated the utilization of superhydrophobic-hydrophilic patterns to engineer multiphase droplets, facilitating the confinement of an organic liquid droplet within an aqueous one or enabling miniaturized liquid-liquid-liquid extraction applications.[259] Other strategies aimed at liquid confinement without the reliance on solid boundaries encompass the incorporation of water into a matrix of viscous polydimethylsiloxane oil,[260,261] the implementation of water-oil emulsions within microfluidic devices,[191,262] and the utilization of aqueous channels stabilized by immiscible magnetic liquid barriers.[263] Nevertheless, these approaches are predominantly limited to the confinement of water and did not utilize the power of a liquid with the higher surface tension to confine and shape another liquid with the lower surface tension.

Therefore, the aim of the current project was to demonstrate the mechanical stability and versatility of water walls on a chemically patterned hydrophilic-omniphobic surface, and its ability to act as a solid-like wall when confining a diverse range of organic liquids (**Figure 11**). In this project, liquid wells were investigated for being capable of containing various LSTLs in multiple shapes and volumes, as well as having a diverse functionality, which includes adaptability, self-restoration capabilities, and dynamic reactive behaviour, and altogether makes liquid wells a unique alternative to classical solid vessels.
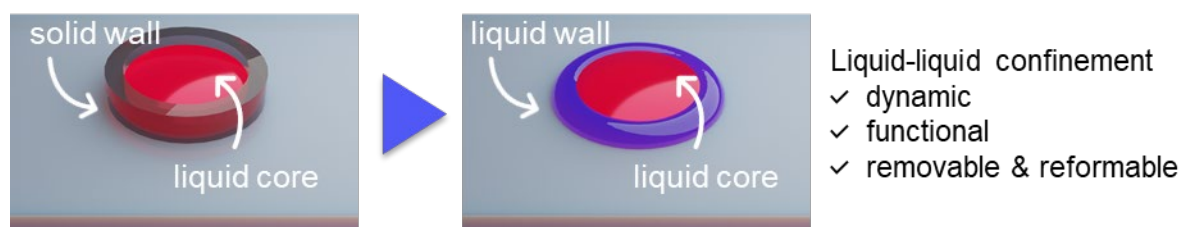
Figure 11. Project idea scheme. Distinctive features of a liquid-wall container as an analogue for a solid vessel.[241] Adapted from SCHEIGER ET AL. with permission. Copyright 2021, Wiley-VCH.

3.1.2 Results and discussion

To confine the low surface tension liquids (LSTL) by a fully liquid wall, the power of water as the liquid with the highest known surface tension, was used. However, to form a "water wall" on surface, the surface modification of the glass substrate had first to be applied. The functionalization was carried out through a reaction of 2-mercaptoethanol for the hydrophilic regions or 1-dodecanthiol for the hydrophobic regions with the vinyl groups on the previously modified nanoparticle-coated substrate (**Figure 12** A).
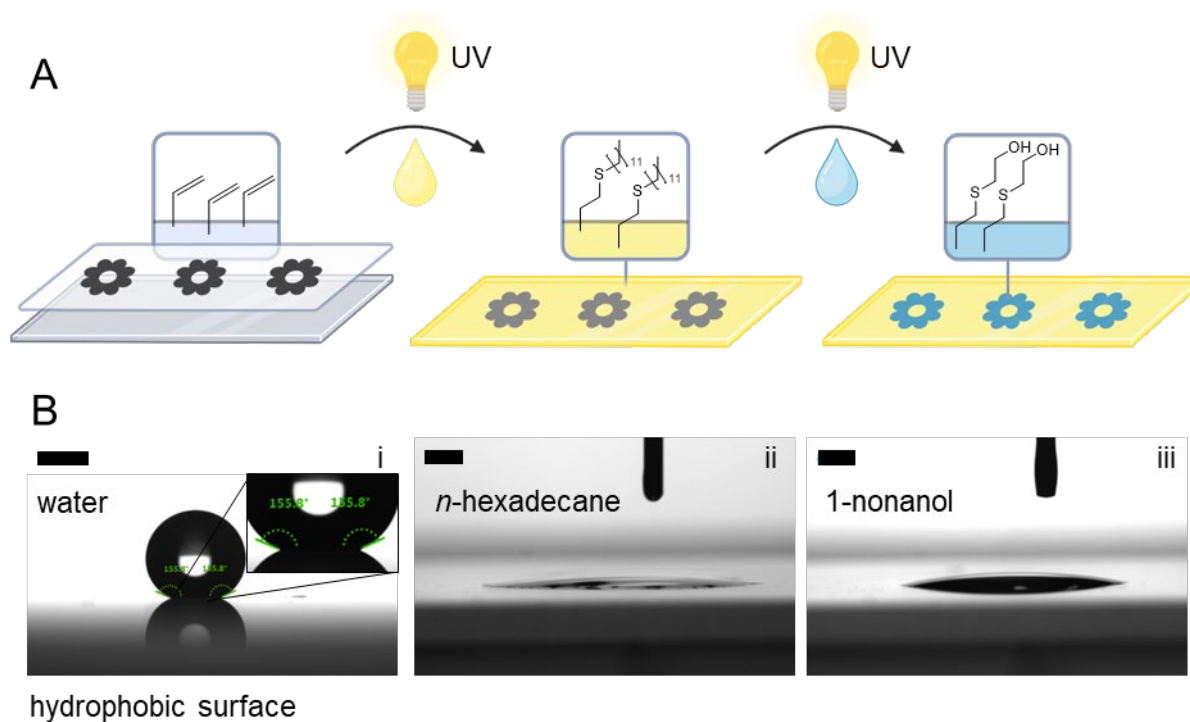
Figure 12. Thiol-ene surface modification of a glass substrate under UV-light. A) First, hydrophobic modification is carried out under a photomask, after this the hydrophilic borders are created. The modification occurs through the reaction of alkyl thiols or thioalcohols with the vinyl groups on the substrate surface premodified with nanoparticles. B) Static contact angles of water, n-hexadecane, and 1-nonanol on the hydrophobic part of the chemically patterned substrate. Values are given in **Table 1**. Scalebars: 1 mm. Adapted from SCHEIGER ET AL. with permission. Copyright 2021, Wiley-VCH.

The wettability of the surface after coating was determined via contact angles of liquid droplets measured with the contact angle goniometer. The alkyl-thiol-coated regions showed significant hydrophobicity, whereas remained fully wettable for hydrophobic solvents, as shown by the example of n-hexadecane and 1-nonanol (**Table 1**). Despite first forming a droplet on surface (**Figure 12** B), both hexadecane and 1-nonanol kept slowly spreading over the surface, hence no static contact angle could be measured anymore and were considered negligible. In turn, hydrophilic regions were fully wettable for both aqueous and organic droplets.

Table 1. Apparent contact angles for different regions of the patterned surface

Area of the pattern	Contact Angle [°]		
	water	*n*-hexadecane	1-nonanol
Hydrophilic (modified with 2-mercaptoethanol)	0	0	0
Hydrophobic (modified with 1-dodecanethiol)	157 ±7	0	0

Patterns with sub-millimeter details in any desired shape could be created with various photomasks. These patterns allowed aqueous liquids to assemble precisely in the shape of the

pattern, forming sharp, smooth edges while avoiding the hydrophobic areas around them, as shown by optical microscopy (**Figure 13**).
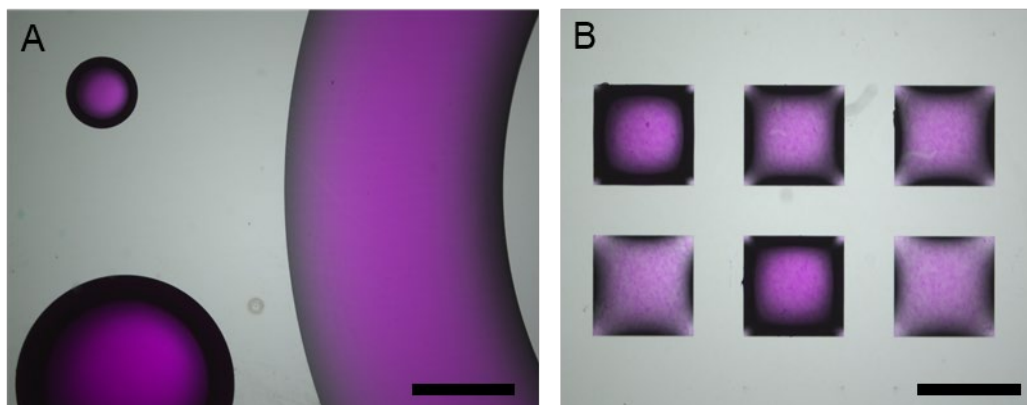
Figure 13 Optical microscopy images of hydrophilic surface areas filled with water. Liquid compartments filled with water colored with Rose Bengal exhibit sharp hydrophilic patterns of various shapes. Scalebar: 1 mm. Reproduced from SCHEIGER ET AL. with permission. Copyright 2021, Wiley-VCH.

Nonetheless, since confining a non-aqueous liquid within the aqueous wall was feasible only if the latter had a closed shape, with the hydrophobic region enclosed inside, water had to be first applied to the hydrophilic region of the pattern until it formed a closed well.
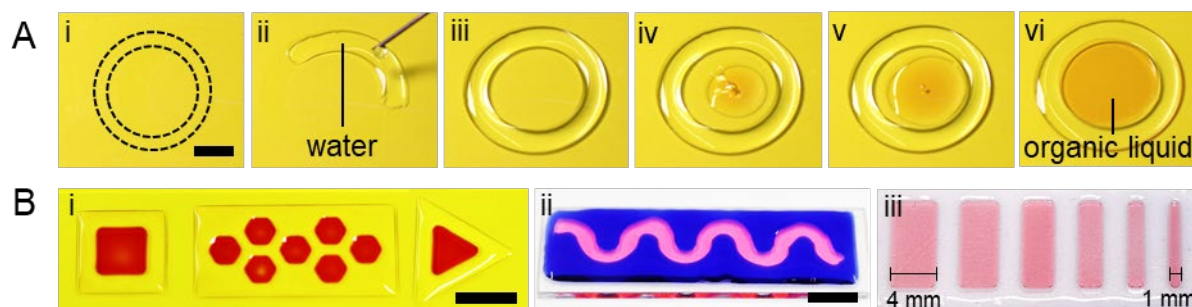
Figure 14. Formation of a liquid-liquid well. A) Water forms a ring on the hydrophilic surface area (dashed line). The organic solvent (1-nonanol, dyed with Oil Red O) is then added into the liquid well. Scale bars: 5 mm. B) Images of liquid wells with various shapes containing different LSTLs. (i) Red liquid: toluene dyed with Oil Red O), transparent liquid: water. (ii) Blue liquid: water dyed with blue ink. Pink liquid: 1-nonanol dyed with Rose Bengal., (iii) Transparent liquid: water. Pink liquid: 1 nonanol dyed with Rose Bengal. Scale bars: 10 mm.[241] Adapted from SCHEIGER ET AL. with permission. Copyright 2021, Wiley-VCH.

Subsequently, the LSTL was applied to the hydrophobic surface area enclosed by the water wall, where it spread but remained restricted to the shape pre-defined by the water barrier (**Figure 14** A). To illustrate the capability of this core-shell approach to produce a diverse and complex range of shapes, various patterns with different interior angles (60°, 90°, 120°) and a labyrinth-like structure were designed, as well as closed compartments as small as 1 mm. (**Figure 14** B). Despite the overall high variability of shapes and the ability of water barriers to dictate the shape of the organic liquid layer, another limitation for the sharp shapes, such as

rectangular and triangular (i, iii) forms, was observed. For the non-circular patterns, LSTLs tended to form not sharp but rounded edges inside the water barriers, which aligns with the principles of the Young-Laplace equation stating that liquids arrange themselves by minimizing potential energy while preserving their volume.[264]

To prove the chemical composition at the interface of the aqueous wall and the LSTS core, RAMAN mapping method has been applied. This method allows to create a chemical map of the sample based on Raman spectra collected from the array of spots on the sample (**Figure 15**).
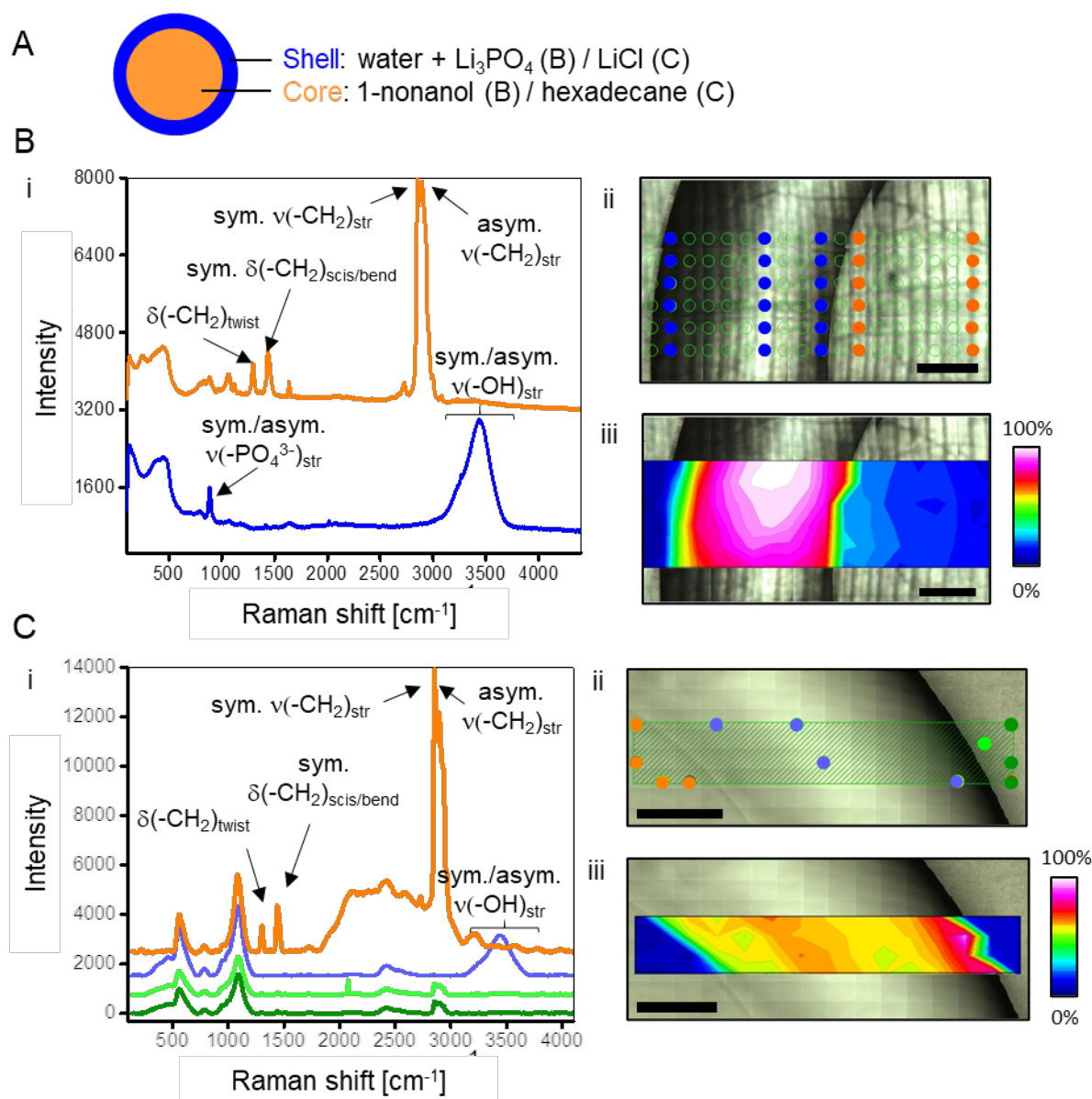
Figure 15. Raman mapping of the liquid-liquid interface between an organic liquid trapped in a ring of water. (A) Schematic illustration and chemical composition of the analyzed patterns. (B) Raman mapping results with 1-nonanol as organic core: averaged Raman spectra (i) obtained on different spots (ii) around the liquid-liquid interface. (C) Raman mapping results with n-hexadecane as organic core: averaged Raman spectra (i) obtained on different spots (ii) around the liquid-liquid interface. Integration and color coding of the OH stretching scattering

intensity yields a chemical map (B.iii, C.iii). Scale bars: 1 mm.[241] Reproduced from SCHEIGER ET AL. with permission. Copyright 2021, Wiley-VCH.

For the analysis, the circular shape pattern (previously shown at **Figure 15** A) was chosen, the shell of which was filled with aqueous LiCl or Li_3PO_4 (0.5 mg · mL^{-1}) solution, with the soluble lithium salts added to avoid the unwanted evaporation of water during the long measurement. The core was filled with either 1-nonanol or n-hexadecane, two high-boiling-point, practically immiscible with water LSTLs. Raman Spectra were recorded at various points on the sample. The intensities of the C-H stretch (3020 to 2780 cm^{-1}) and O-H bend (3100 to 3700 cm^{-1}) vibrations were chosen for the measurement to illustrate the phase separation between 1-nonanol/n-hexadecane and water surfaces. In case of 1-nonanol-filled ring (**Figure 15** B), the O-H vibration intensity showed to grow towards the center of the ring, likely due to an increased height of the water layer caused by the curvature of the water wall. Conversely, the C-H vibrations in the 1-nonanol phase showed a decrease in scattering intensity from the edge to the center of the circle. On average, the spectra from the water ring (blue, averaged) can be clearly distinguished from the spectra on the 1-nonanol-filled middle part (orange, averaged), which is as well true for the n-hexadecane-filled ring (**Figure 15** B).
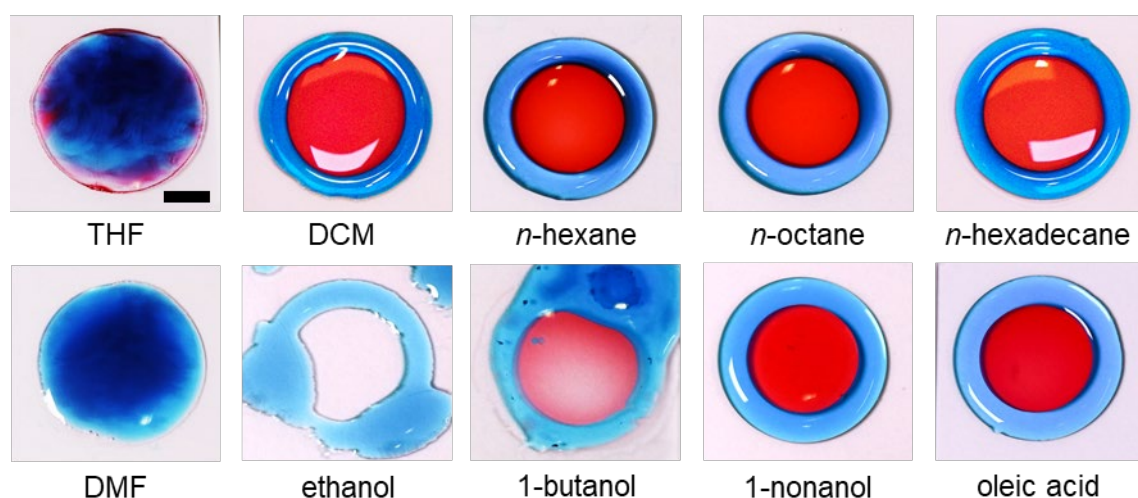
Figure 16. Confinement of low surface tension liquids by a water ring. For visualization, water was dyed with blue ink and the organic phase was dyed with oil red. Scale bar: 5 mm.[241] Reproduced from SCHEIGER ET AL. with permission. Copyright 2021, Wiley-VCH.

To further investigate the ability of a water wall to confine various organic liquids, the practical ring confinement test was carried out on the range of organic solvents with different physical properties (**Figure 16**). As expected, liquids miscible with water dissolved into the water walls. This mixture then either spread across the glass surface, as seen with ethanol and water, or stayed within a ring-like pattern, like with tetrahydrofuran-water and N,N' dimethylformamide-

water combinations. When examining a group of primary alcohols with gradually longer alkyl chains, such as ethanol, 1-butanol, and 1-nonaol, it was observed that only the most hydrophobic of them, 1-nonanol, could be confined by the water barrier. Other tested non-polar solvents, including toluene, dichloromethane, n-hexadecane, n-octane, and n-hexane, appeared to be successfully confined within the water wells as well. Physical properties of the tested solvents are presented in **Table 2**. Therefore, based on the large variety of solvents tested in this experiment, one could conclude that the only crucial criteria for the stability of the liquid-liquid well as the chemical non-miscibility of the organic liquid. From the practical point of view, such system could only be claimed "stable" when using non-volatile organic liquids with higher boiling points. Nonetheless, the experimental observation of dyed solutions of rapidly evaporating solvents, such as toluene and dichloromethane showed that they stayed confined within the water wall while evaporating, which could be very useful for, e.g. templated coating, thin-film or evaporation-induced polymerization applications, where fast evaporation of the organic solvent is a great advantage for the experiment.

Table 2. Physical properties of the solvents used for the ring-confinement test.[241]

Solvent	γ_{oa} [mN m^{-1}] (at 20 °C)	Dielectric constant (at 20 °C)	Boiling Point [°C]	Density (20°C) [g ml^{-1}]	Water solubility (20°C) [g L^{-1}]
Ethanol	22.1	24.5	78.3	0.789	Miscible
Ethyl acetate	23.2	6.02	77.1	0.902	83
1-Butanol	24.2	17.8	117.7	0.81	73[a]
1-Nonanol	28.0	8.83	215.0	0.827	1.0
Tetrahydrofuran	26.4	7.58	66.0	0.889	Miscible
Dichloromethane	26.5	9.08	39.8	1.325	17.5[a]
n-Hexadecane	26.95	2.05	287.0	0.773	2.3·10^{-5}
Toluene	28.4	2.44	110.6	0.865	5.2·10^{-1}
Dimethylformamide	37.10	36.7	152	0.95	Miscible
1-Hexane	18.43	1.89	68.7	0.672	9.5
1-Octane	21.62	1.95	125.0	0.7	7·10^{-4}
iso-Octane	18.77	1.94	99.0	0.69	-

at 25 °C

In order to explore the possibility of such liquid-liquid well to contain the third phase, the following experiment has been conducted. First, the ring pattern was filled with water (dyed with blue ink). Then, the core of the pattern was filled with the fluorinated liquid. After that, a drop of hexadecane (dyed with Oil Red O) was put in the middle of the ring. After being placed on top of the fluorinated fluid, the hexadecane droplet migrated to the water barrier and slowly spread on top of the fluorinated layer, from the corners to the center, forming a thick third film (**Figure 17**). Therefore, a triple-liquid system was created due to the hydrophilic water barrier and the strong omniphobicity of the first liquid in the ring.
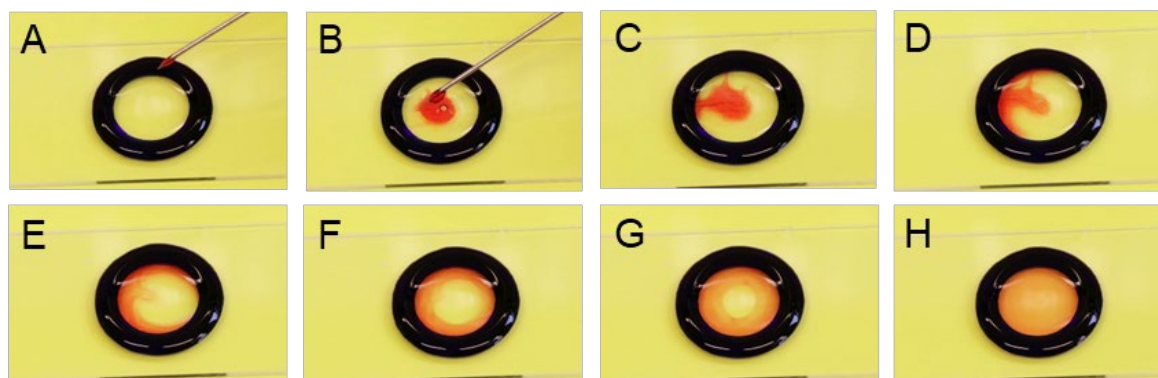
Figure 17. Confinement of two organic liquids by the water wall. From (A) to (H): spreading of a dyed hexadecane drop (ca. 1 µl) over the fluorinated liquid (30 µl) inside of the water wall (80 µl).

To address a following-up question if a polar liquid could be confined in the middle of the ring, the next experiment was designed. This time, a series of hydrophobic acrylates was tested for the ability to confine a water drop in the hydrophobic center of the ring pattern, so that it doesn't merge with the water well. As in the previous experiment, the water wall was formed on the ring pattern first. Then, one of four liquid hydrophobic methacrylates, including butyl methacrylate, trifluoroethyl methacrylate, dodecyl methacrylate, and heptadecafluorodecyl methacrylate was added to the middle of the pattern. After that, a drop of water (dyed with the blue ink) was placed on top of the hydrophobic liquid. The droplet migrated to the water barrier within seconds, however, the time of merging with the aqueous well differed depending on the organic liquid. For butyl methacrylate, the merging time was less than 2 s, while for the most hydrophobic and dense methacrylate in the series, heptadecafluorodecyl methacrylate, the droplet didn't merge with water wall up to several minutes (**Figure 18**). Apart from that, several aqueous droplets could be added to the liquid-liquid system simultaneously without merging (**Figure 18**). Thus, it has been demonstrated that liquid-liquid wells could confine multiple liquids with varying polarities within a single set-up, provided the immiscibility criteria are met. Additionally, the triple-liquid experiments revealed that not only basic organic solvents

but also a broad range of non-polar organic liquids, including, for example, hydrophobic an omniphobic methacrylates, can be successfully contained within aqueous barriers.
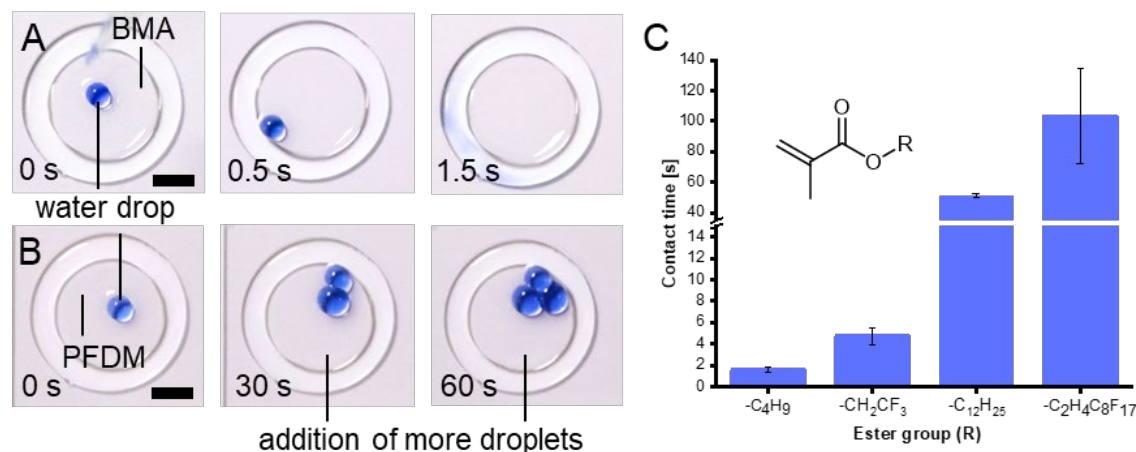
Figure 18. Confinement experiment of water droplets within the water-barrier in dependence of the inner organic layer. The organic-circle within the water-ring contained (A) butyl methacrylate and (B) heptadecafluorodecyl methacrylate. Scale bar: 5 mm. (C) Graph comparing the contact time obtained for different methacrylates. The contact time increased from butyl methacrylate, trifluoroethyl methacrylate, dodecyl methacrylate, to heptadecafluorodecyl methacrylate, respectively.[241] Reproduced from SCHEIGER ET AL. with permission. Copyright 2021, Wiley-VCH.

Liquid walls exhibited distinctive capabilities that set them apart from solid containers, one of which is being capable to hold a greater quantity of liquid than their height and size, largely due to the water wall's ability to adapt and deform. For instance, it has been observed that gradually increasing the volume of organic solvent (in this experiment, 1-nonanol) in a ring pattern (filled with 60 µL water) from 50 µL to 200 µL of 1-nonanol, the water ring, although visibly stretched, still managed to confine the volume of the organic liquid, surpassing its own volume by over three times (**Figure 19** A). At this volume, the meniscus of 1-nonanol was significantly higher than the water barrier, due to, presumably, the capillary forces which counterbalanced the gravity on the water ring, preventing the organic liquid from spilling. Based on the theory, the maximum capacity of the water well should be linked to the height of the liquid wall. This height has been theoretically described as a balance between capillary and gravitational forces, resulting in a length scale of $\lambda_c = (\gamma_{wa}/(\rho_w g))^{1/2}$ and the capillary length $\lambda_{c(water)} = 2.73$ mm. In this expression, γ_{wa} is the surface tension of water, ρ_w is the mass density of water and g is the gravitational acceleration. For the case that the radial extension of the liquid wall is much larger than λ_c, the rounded liquid surface will become increasingly flat, and the height of the wall approaches a value of $2\lambda_c \sin(\theta_w/2)$, where θ_w is the contact angle of water on the substrate.[265] To assess the maximum height of the water wall in the current setup (a ring on a

patterned surface) experimentally, its height was measured as a function of water volume, and reached the maximum of 1.95 mm for 210 µL of the contained liquid (see **Figure 19** B.i, ii and **Figure 18** C). In turn, the greatest height achieved by an organic liquid within a liquid well was 1.97 ± 0.02 mm, using 330 µL of 1 decanol contained by 60 µL water (**Figure 19**B, iii). Similar to the 1-nonanol case (**Figure 19** A), the meniscus of the 1 decanol exceeded the water wall's height several times, while the water wall deformed into a flattened state compared to it without the organic solvent inside. To confirm the observed the ability of the water wall to stretch and adapt to the volume of the liquid inside it, the height of the water wall was measured as the function of 1-decanol volume (**Figure 19** D). In this experiment, the water volume was kept at 60 µL, while varying amounts of 1-decanol were added to the core. Adding 40 µL of 1-decanol lowered the wall's height from 0.63 mm to 0.52 mm, presumably, due to the strong electrostatic interactions between water and 1-decanol molecules. However, the further increasing of the 1-decanol volume to 60 µL gradually raised the water wall's height to 0.58 mm, however, never reaching its original height without 1-decanol.
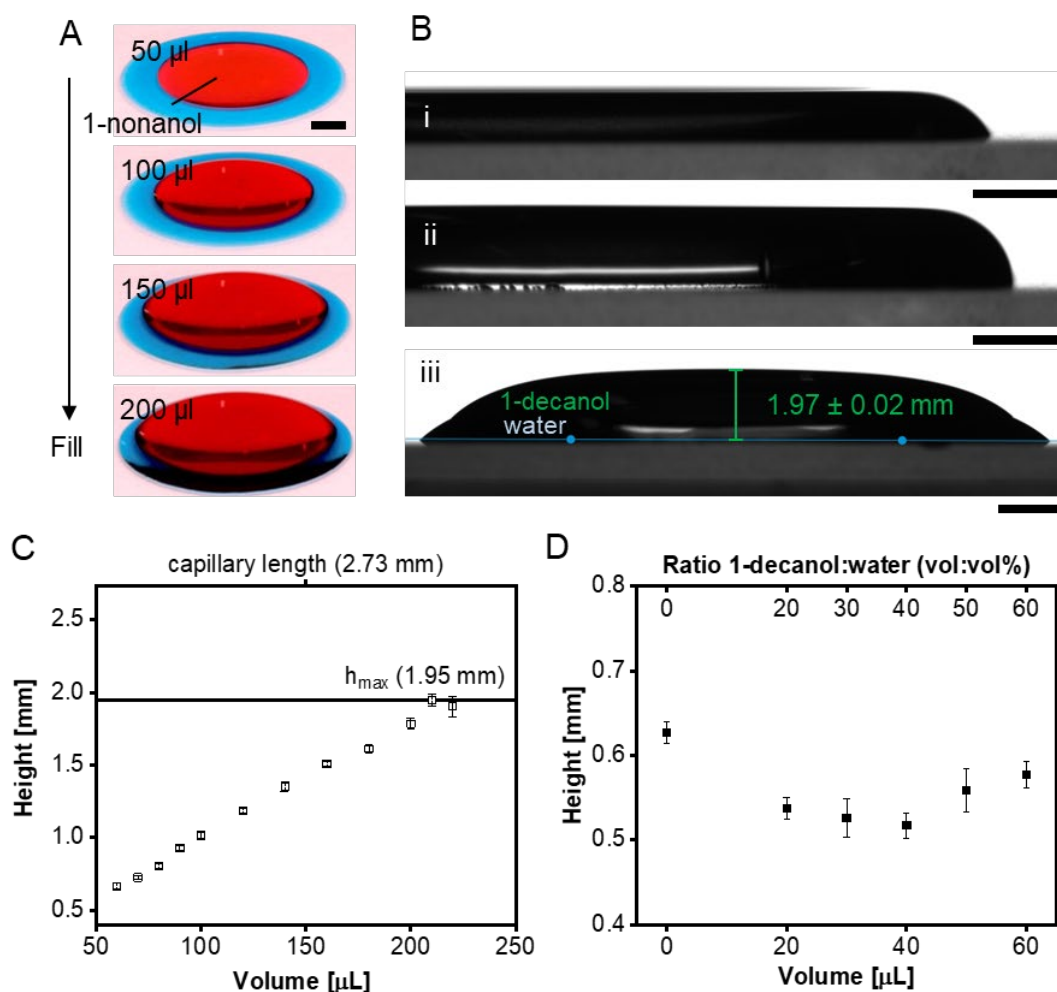
Figure 19. Liquid capacity test for the ring-shaped liquid-liquid well. (A) Capacity test for 1-decanol in a 60 µl water ring. (B) Illustration of a height test of the water wall for (i) 100 µl and (ii) 180 µl; a maximum height

(1.97 ± 0.02 mm) of 1-decanol that 60 µl of water could confine before the system becomes unstable (iii). (C) Height of a ring-shaped water wall as a function of the water volume. (D) Height of ring-shaped water wall as a function of the contained 1-decanol volume. Scale bars: 2 mm. Error bars in the graphs represent standard deviations (n=3). [265]Adapted from SCHEIGER ET AL. with permission. Copyright 2021, Wiley-VCH.

To sum up, the water wall's height and capacity in the liquid-liquid well largely varies depending on its own volume and the volume of the contained organic liquid, and thus can be adjusted by both of these parameters. This contrasts with previously reported liquid systems on omniphobic-omniphilic surface patterns, where the liquid's height and volume was shown to rely heavily on its contact angle with the surface, a property more challenging to dynamically change than the height of a liquid wall or core.[79] Additional important parameters that could affect the water wall capacity and maximum height but, unfortunately, have not been covered in the current project, are: the various sizes and shapes of the pattern; organic solvents with varying chemical and physical parameters; mixed aqueous systems compared to the pure water, and others. Investigating this phenomenon more detailed would be necessary to discover further features and limitations of the presented liquid-liquid wells system.

The intrinsic dynamic nature of a water to reform after the applied force could provide the liquid walls with the ability to reform after being distorted too, which was further verified by the "cutting" and "agitating" experiments. First, the ring-shaped liquid-liquid well was repeatedly sliced through with a ceramic knife, after which the well quickly restored its structural and compositional integrity (**Figure 20** A), except for a few traces of the organic liquid that were transferred with the knife (**Figure 20** B). In another experiment, a complex maze-like liquid-liquid well was actively agitated within a minute to test if the dynamic characteristic of liquid compartments would create a stability issue for handling the system. On the contrary, due to the liquid-liquid interactions between the aqueous walls and the organic core, as well as very strong surface affinity of the aqueous walls, even when the aqueous borders were displaced by the rigorous agitation, the system was capable of restoring itself to the initial state (**Figure 20** C). Thus, liquid walls could demonstrate both dynamic response to the mechanical force and the wall stability important for any real-life handling. To further demonstrate the dynamic features of the liquid wall the simple extraction test was carried out (**Figure 20** D). A dye solution consisting of Oil Red O (0.1 vol%) and methylene blue (0.1 vol%) dissolved in 1 decanol (30 µL) was deposited in a ring of water (100 µL). Immediately after the deposition (0 s) of the dye solution, methylene blue started to diffuse into the water barriers, whereas Oil Red O remained in the 1-decanol phase. The separation of the hydrophilic and hydrophobic components was complete within less than 2 hours. The water wall could thus not only confine

organic phase but also extract hydrophilic compounds from it, which made it more functional than a traditional vessel (i.e. made out of glass or metal). Noteworthy, the demonstrated experiments showed not only dynamic properties but also the robustness of liquid-liquid systems both against mechanical distortions and instabilities related to the evaporation of the aqueous wall. For example, the well remained stable during the extraction experiment that lasted more than 2 hours in total, with the only precaution against unwanted evaporation being made that the liquid well was covered with a plastic petri dish during the extraction. Certainly, the dynamic functionality of the liquid wells was only demonstrated briefly in this project and could be further developed to fully utilize this unique feature in the fields of liquid transfer, microfluidics, sensing, purification, and many others. Many more experimental setups could also be further realized for the water walls as extraction vessels, such as for example increasing the area of contact with the organic liquid by changing the wall-core ratio of the wells or changing the liquid volumes, refilling of the water after the saturation with the transferred substance, as well as the backwards extraction to the organic phase.
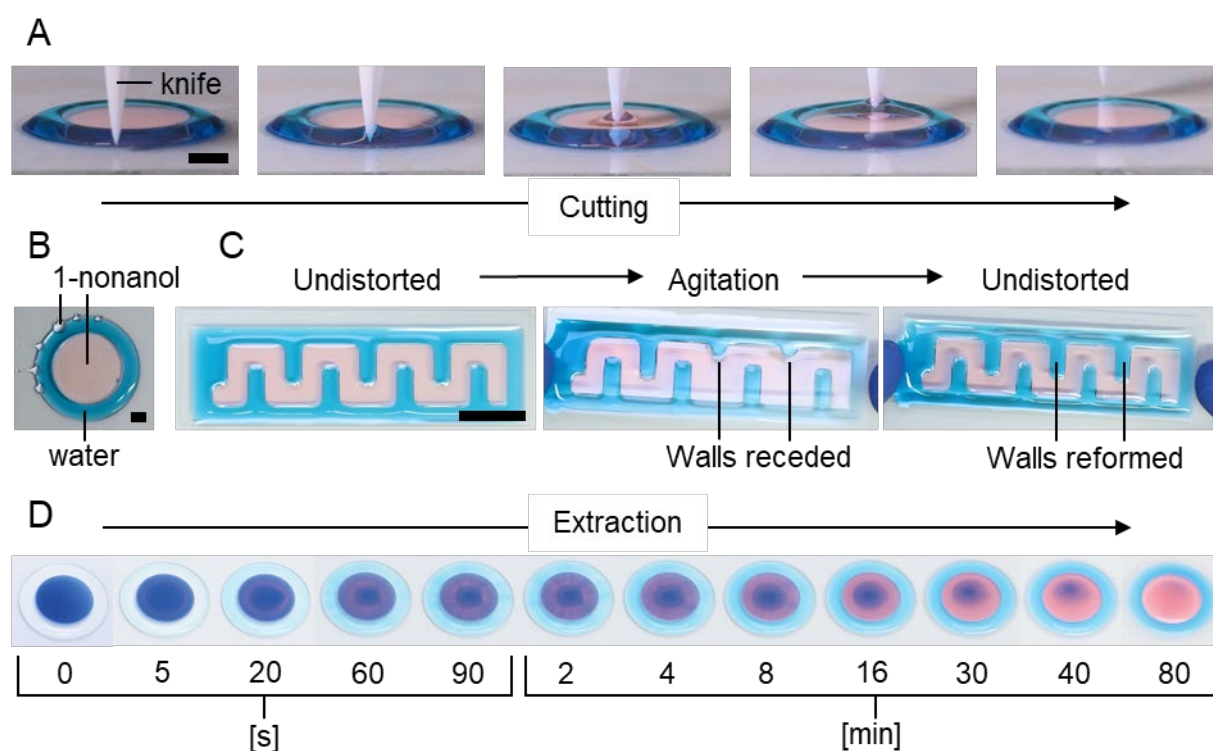
Figure 20. Dynamic properties of liquid wells. (A) Demonstration of cutting through the ring-shaped water wall – 1-nonanol core pattern. Water volume: 60 µL, 1-nonanol volume: 20 µL. (B) Picture of a ring-shaped water wall confining 1-nonanol after being cut by a knife multiple time.Scale bar: 3 mm. Water and 1-nonanol are dyed with blue ink and oil red o, respectively. (C) Agitation test for the stability of the liquid-liquid well. (D) Time-lapse of the extraction process of a hydrophilic dye (methylene blue) from the organic liquid (1-decanol additionally dyed with oil red o) to the water barrier.[241] Adapted from SCHEIGER ET AL. with permission. Copyright 2021, Wiley-VCH.
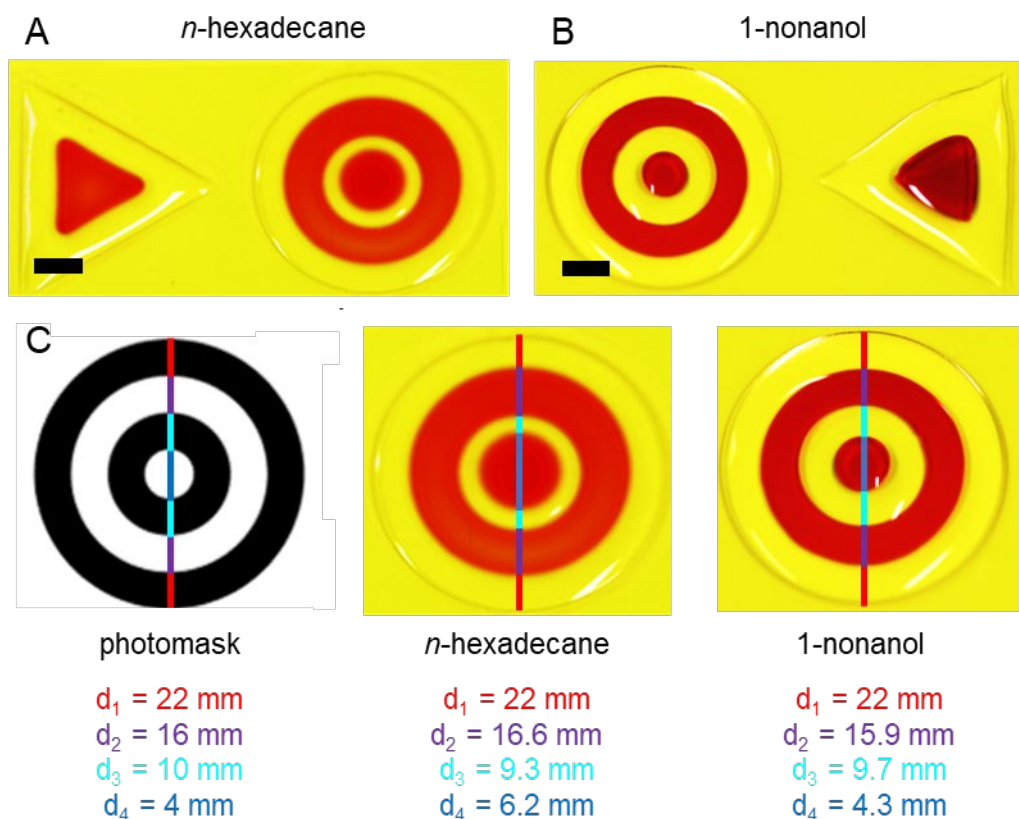
Figure 21. **Demonstration of differences when filling complex-geometry patterns with two different organic liquids.** Triangular and multiple-rings-shaped liquid-liquid wells filled with (A) n-hexadecane and (B) 1-nonanol demonstrate how distribution of the organic liquid and the ratio between the aqueous liquid part and organic liquid part differ for the same surface substrates. Organic liquids are filled with Oil Red O. Scale bars: 200 µm. (C) Measured difference between the diameters of the pattern rings of the photomask compared to the rings formed by n-hexadecane and 1-nonanol. For the inner and outer water barrier, 20 and 60 µL of water were added, respectively. For the organic liquid layers, same volumes of n-hexadecane were used, 8 µl for the inner ring and 40 µL for the outer ring. Adapted from SCHEIGER ET AL. with permission. Copyright 2021, Wiley-VCH.

For patterns more complex than the ring pattern that was previously used for the solvent test (e.g., patterns with sharp edges or multiple compartments), a noticeable difference was observed in the distribution of different organic liquids within the aqueous walls. For example, the clear visual evidence was observed when comparing patterns filled with two seemingly similar high-boiling-point LSTLs, n-hexadecane and 1-nonanol (**Figure 21** A and B). For example, 1-nonanol deposited in a triangular liquid well resulted in the shape of a Reuleaux triangle, whereas the use of n-hexadecane resulted in a barely altered triangular shape. In turn, for the multiple-rings-shaped pattern, 1-hexadecane evidently spread over the water surface, compared to 1-nonanol, which concentrated on the hydrophobic pattern and left the water barriers practically unchanged.

To prove the visual observation, a multiple-rings-shaped pattern was chosen (**Figure 21** C). The inner and outer water barrier, were filled, respectively, with 20 and 60 µL of water.

Whereas, the inner and outer organic liquid layers were filled with 8 and 40 µL of either n hexadecane or 1 nonanol, respectively. Both 1-nonanol and n hexadecane were dyed with 0.5 mg ml^{-1} Oil Red O to improve the visibility of the boundaries. After filling all the compartments and imaging the patterns, the diameters of all the pattern compartments were measured and compared with the initial photomask diameters, assuming that the outer aqueous ring diameter remained unchanged (ca. 22 mm). From the measured diameters, the total surface area covered by the respective organic liquid, could be calculated (results are shown in **Table 3**). As expected, n-hexadecane showed to take up a larger share of the surface area relative to the total area that was covered by 1-nonanol, resulting in 47% and 37%, respectively.

Table 3. Measured total surface area for the organic and aqueous part of the multiple-ring-shaped well (based on the diameters from Figure 21 C)

The part of the pattern	Total surface area [mm^2]	Proportion of total area [%]
Total area (d = 22 mm)	380.1	100
Area covered by n-hexadecane	178.7	47
Area covered by 1-nonanol	139.2	37

The investigation into the stability and solvent-related constraints of the presented liquid-liquid systems was a critical component of the project, particularly given the distinct behaviors of various non-polar solvents, as demonstrated by 1-nonanol and n-hexadecane. It was clear that liquid-liquid surface tensions must influence the interaction between the non-polar core and aqueous boundaries. Based on that, a hypothesis was proposed that the behavior of the non-polar liquid confined by aqueous borders, could be analogous to the behavior observed when a droplet of this liquid comes into contact with a bulk water surface. Indeed, it is commonly known that hydrocarbon oils tend to spread over the water surface in the form of thin films, which is the fundamental basis of the ecological problem of oil spills. However, it remained uncertain whether 1-nonanol would exhibit same or different behavior when in contact with bulk water. Therefore, a straightforward observational experiment was next conducted, in which a drop of 1-nonanol was brought in contact with water in a petri dish. For the variety of volumes tested (from 10 to 50 µL), 1-nonanol formed confined droplets that did not spread over the surface of the water, whereas for the hexadecane no droplets were formed and instead the immediate spreading and formation of the almost invisible thin film happened (hence, no images of this observation presented here). This again confirmed the hypothesis that the main difference between n-hexadecane and 1-nonanol-based liquid-liquid systems took place in the different character of interfacial interactions with water molecules.
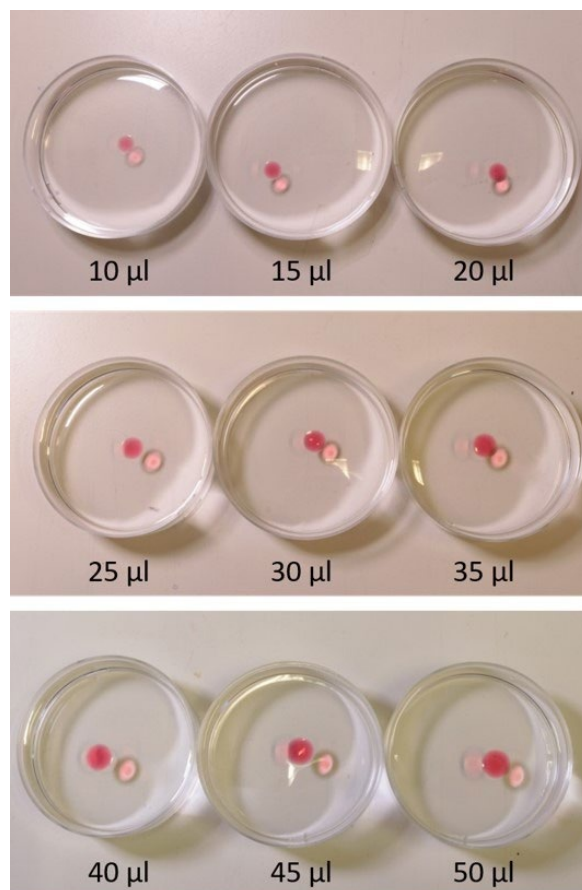
Figure 22. Images of 1-nonanol droplets (dyed with Oil Red O) in petri dishes filled with DI water. For all volumes tested (10 - 50 µL), 1 nonanol formed droplets which did not spread over the surface of the water. The same result was obtained for pure droplets of 1-nonanol.[241] Adapted from SCHEIGER ET AL. with permission. Copyright 2021, Wiley-VCH.

After finding out that the confinement of n-hexadecane within the water barrier might co-occur with (presumably, partial) spreading over the water surface, it was crucial to further investigate a probable formation of the thin film of hexadecane over the water barrier, as well as to image the interface water-organic liquid for the cases of n-hexadecane and which was attempted by confocal laser scanning microscopy (CLSM). Via CLSM, the 3D-stack images of pure water, as well as the water-n-hexadecane and water-1-nonanol filled rings were created (**Figure 23**). Therefore, the morphology at the boundary where water and organic liquid meet, was depicted before and after the introduction of either n-hexadecane or 1-nonanol. As shown by the images, the introduction of n-hexadecane resulted in minimal alteration to the configuration of the water boundary. In contrast, the addition of 1-nonanol caused the water boundary to extend into the area occupied by 1-nonanol, matching a noticeable difference in the volume occupied by 1-nonanol compared to n-hexadecane noticed in the previous experiments. This phenomenon could be attributed to the way the organic solvent interacts with the water barrier, leading to a non-linear reduction in the height of the organic solvent.
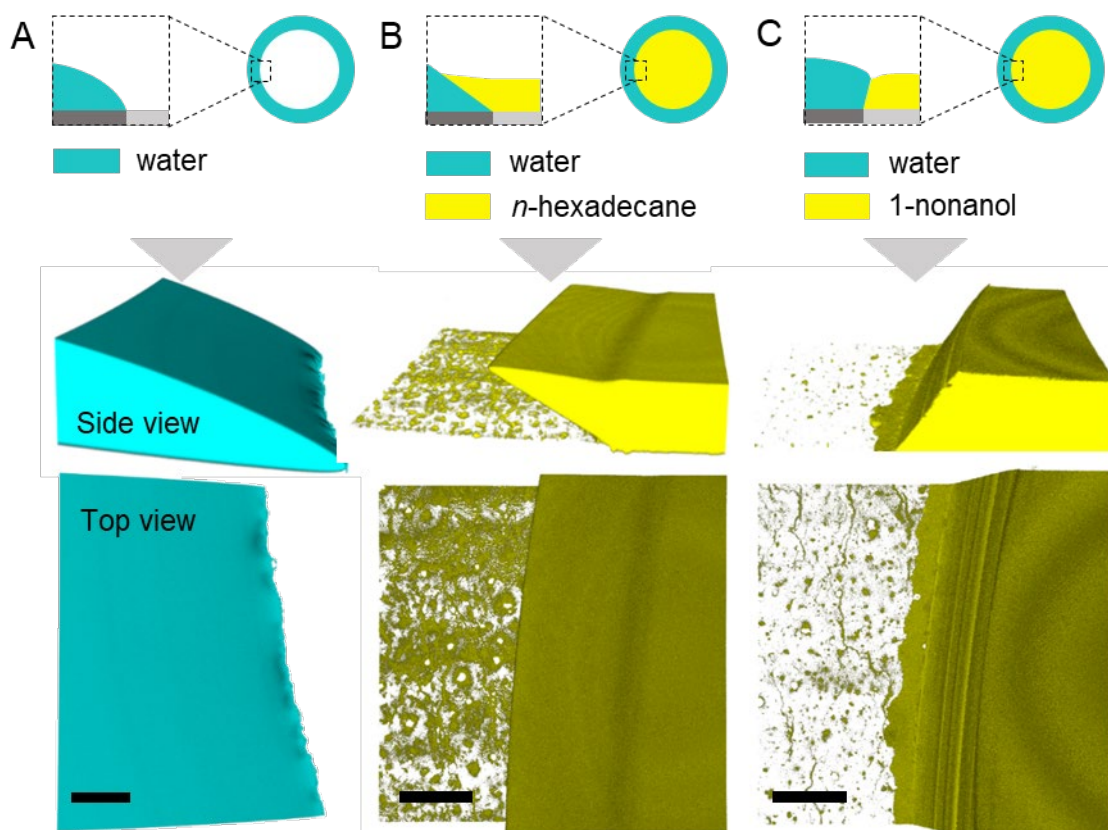
Figure 23. CLSM microscopy imaging of the water-organic-liquid interface for a circular pattern well. Schematic depiction of the experiment and CLSM z-stack images (side- and top view) of a water ring at (A) the water-air interface, (B) the water-hexadecane interface, and (C) the water-1-nonanol interface. Scale-bars: 200 μm.[241] Adapted from SCHEIGER ET AL. with permission. Copyright 2021, Wiley-VCH.

Due to a non-classical set up including dynamic contact points of liquids with each other, the surrounding gas, and two types surfaces underneath (the hydrophilic and hydrophobic parts of the pattern), the classical liquid-liquid-gas or liquid-solid-gas boundary cases could not explain the observed phenomena. Therefore, in an attempt to theoretically understand the different shapes obtained at the water-solvent interface and to support the experimental observations, liquid wells were simulated with a phase-field model, in the collaboration with the group of BRITTA NESTLER. Coupling the phase-field model with an appropriate boundary condition at the wall can capture the Young's contact angle as well as the so-called Neumann's triangle at a multiple phase junction via minimizing the total free energy of the system. A detailed description of the phase-field model is given by GARCKE and co-workers.[266] The parameter setups and the applied phase-field simulations can be found in the SI section of the published manuscript based on this work.
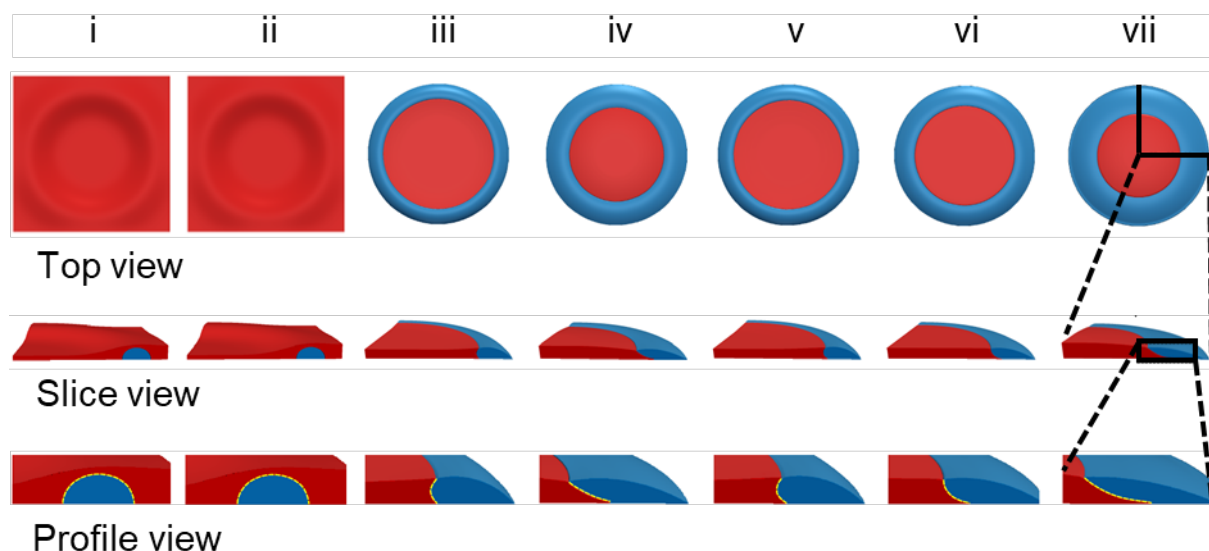
Figure 24. Phase-field simulation for the confinement of 1-nonanol red in a ring of water blue. In the image, 1-nonanol – red, water – blue. Each simulation (i-vii) is based on a different set of the surface and interfacial tensions γ_{oa} (organic-air), γ_{ow} (organic-water), and γ_{wa} (water-air). The surface and interfacial tensions (γ_{oa}, γ_{ow}, γ_{wa}) were (i) (28.0, 8.8, 72.86) mN m^{-1},[37-38] (ii) (28.0, 8.8, 44) mN m^{-1}, (iii) (28.0, 8.8, 36.43) mN m^{-1}, (iv) (28.0, 8.8, 21.86) mN m^{-1}, (v) (36.43, 8.8, 44) mN m^{-1}, (vi) (44, 8.8, 44) mN m^{-1}, and (vii) (51, 8.8, 44) mN m^{-1}. The assumed volumes are 100 µL for 1 nonanol and 60 µL for water. The inner and outer diameter of the hydrophilic surface area are 14 mm and 18 mm, respectively. The first row shows a top view, the second row shows a cross section and the third row highlights the cross section at the interface of 1-nonanol and water.[241] Adapted from SCHEIGER ET AL. with permission. Copyright 2021, Wiley-VCH.

The supporting discussion of the simulation results was gladly provided by DR. YANCHEN WU und DR. FEI WANG. According to Neumann's triangle rule, the formation of a stable three-phase contact line between an organic liquid, water, and air, is possible if the sum of the surface tensions γ_{oa} (organic liquid-air) and γ_{ow} (organic liquid-water) is greater than γ_{wa} (water-air).[267] It was hypothesized, that the same requirement ($\gamma_{ow} + \gamma_{oa} > \gamma_{wa}$) must be fulfilled to confine an organic liquid by a wall of water. Since the surface tension of the water-air interface is high ($\gamma_{wa} = 72.86$ mN m^{-1}), this is the case for *n*-hexadecane ($\gamma_{oa} = 26.95$ mN m^{-1}, $\gamma_{ow} = 55.3$ mN m^{-1}) but not for 1-nonanol ($\gamma_{oa} = 28.0$ mN m^{-1}, $\gamma_{ow} = 8.8$ mN m^{-1}).[268–270] However, if the Gibbs adsorption isotherm, i.e. the change in surface tensions due to the partial solubility of water in 1-nonanol and vice versa (1.76 mol L^{-1} and 1.94 mmol L^{-1}, respectively) is considered, the phase-field model is able to predict a confinement as observed experimentally.[271,272] According to LEE ET AL., the surface tension of the water-air interface can be reduced from 72.86 to 44 mN m^{-1} as a result of the dissolution of 1-nonanol in water.[271] Since the exact amount of 1-nonanol dissolving into the liquid wall is unknown and there is a paucity of literature for the Gibbs adsorption of water at the 1-nonanol-air interface, we considered a range of plausible values for γ_{oa} and γ_{wa} in the simulation. The interfacial tension γ_{ow} (1-nonanol-water) was determined experimentally to be 8.8 mN m^{-2} and was kept constant for all

simulations, since it mutually considers the Gibbs adsorption. For $\gamma_{ow} + \gamma_{oa} < \gamma_{wa}$ no stable three-phase contact line can be established and 1-nonanol moves over the water wall, see case (i) and (ii). When the value of γ_{wa} was reduced to 36.43 mN m^{-1} (iii) and 21.86 mN m^{-1} (iv), stable contact lines were observed. As the value γ_{wa} reduces, the 1-nonanol-water interface tilts inward, which is consistent with the experimental observation via CLSM (**Figure 23**). The simulations based on the phase-field model confirmed the hypothesis, that formation of a stable three-phase contact line and thus liquid wells are possible if the condition $\gamma_{ow} + \gamma_{oa} > \gamma_{wa}$ is met. When literature values for the surface and interfacial tension (γ_{ow}, γ_{oa}) are contemplated, this is the case for *n*-hexadecane but not for 1-nonanol. However, a variation in the surface tensions at the liquid-air interfaces because of the partial solubility of 1-nonanol with water can enable a transition from an instable to a stable liquid well. This explanation could be applied to other low surface tension liquids, such as toluene or *n*-octane, which fail to fulfill the criterion $\gamma_{ow} + \gamma_{oa} > \gamma_{wa}$ but nevertheless could be contained by a water well (**Figure 16**).[270] Moreover, the specific set of interfacial tensions (γ_{ow}, γ_{oa}, γ_{wa}) strongly influences the shape of the organic-water interface, which is most likely the reason for the experimentally observed difference between the shapes of the 1-nonanol-water and the *n*-hexadecane-water interfaces. The sets of surface tensions (iv) (γ_{oa}, γ_{ow}, γ_{wa})=(28, 8.8, 21.86) mN m^{-1} and (vii) (γ_{oa}, γ_{ow}, γ_{wa})= (51, 8.8, 44) mN m^{-1} appear to be the most likely possible parameters to reproduce the stable triple junctions of water-1-nonanol-air and water-1-nonanol-substrate, which were observed experimentally (**Figure 21** B). These findings correlate with the experiment of a 1-nonanol droplet settling on water., shown in **Figure 22**. This would not be the case, if literature values for the surface tensions (γ_{oa}, γ_{ow}, γ_{wa}) were contemplated.

Finally, to demonstrate the potential of liquid wells for practical applications, a water-templated film polymerization experiment has been carried out, in which water walls were used as a recyclable template, easy to remove and restore, and capable of manipulating the film shape. For the first experiment, a radical polymerization reaction was realized, via filling the core of the well with the precursor solution (the composition is shown in **Figure 25** A) and irradiating it under UV light ($\lambda_{max} = 365$ nm, 17-18 mW cm^{-2}) for 3 minutes. After the UV polymerization, the water template was washed away to obtain a free-standing polymer film with a thickness of 150-200 µm.
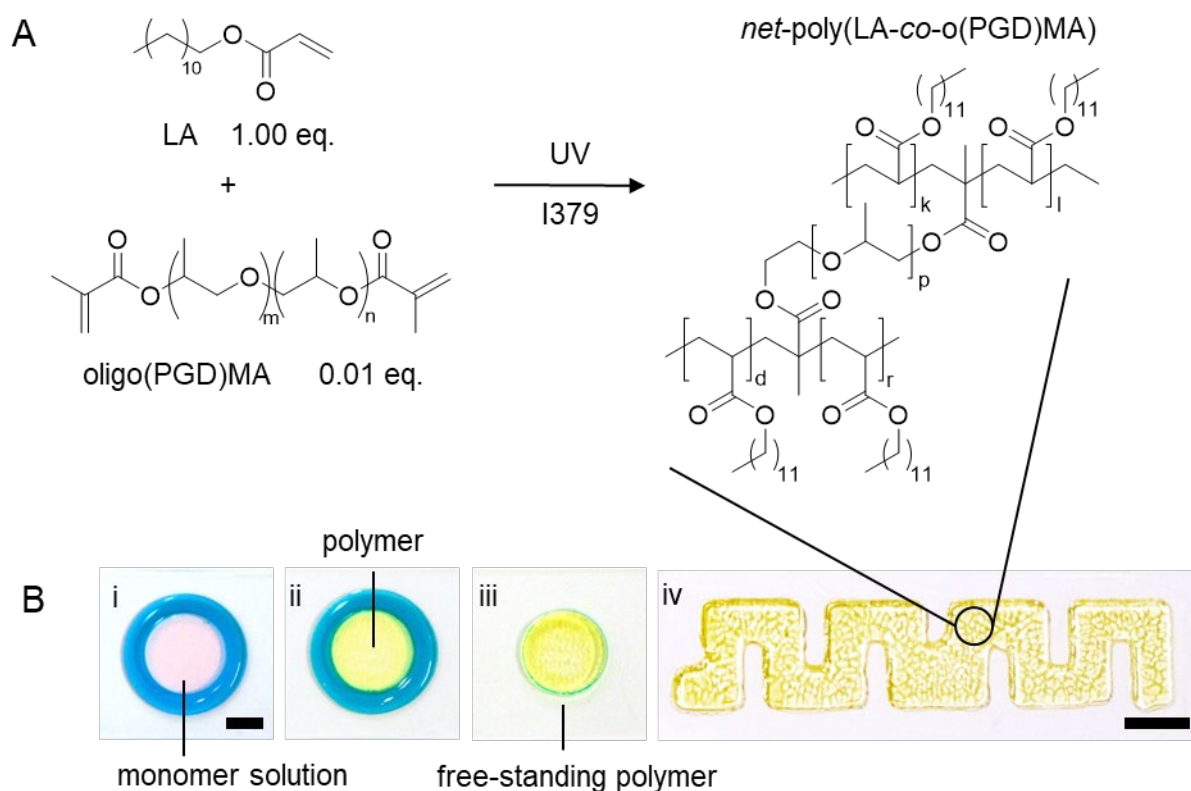
Figure 25. Water-templated film polymerization with liquid wells. (A) Reaction equation of the UV crosslinking polymerization of lauryl acrylate with oligo(propylene glycol) dimethacrylate (o(PGDMA)) using photoinitiator Irgacure 379. (B) Images showing the process of a water templated polymerization (WTP). First, (i) a liquid well is formed with a monomer solution in the core. Then, (ii) the liquid well is irradiated with UV light to trigger polymerization. At last, (iii) the water walls are rinsed away to reveal the polymer film. Complex shapes (iv) can be polymerized in a single step using the water templated polymerization. Scale bars: 5 mm.[241] Adapted from SCHEIGER ET AL. with permission. Copyright 2021, Wiley-VCH.

The process of water-templated polymerization can be used to prepare shaped polymer films in a single polymerization step and is economically and ecologically more efficient than a UV polymerization with a photomask, since all the monomers are polymerized and the liquid templated can be washed away and restored by rinsing or evaporation. Conveniently, the water walls can be reformed and the next film can be polymerized on the same template, similar to a classical mold, given if the chemical patterning of the substrate surface was not destroyed by removing of the previously polymerized film. The ease of use, possible automatization and the potential sustainability of the process makes it very interesting for the interfacial and film polymerization applications.[273] Furthermore, various perspective features of the method are to be further explored, such as its compatibility with other polymerization techniques (e.g., evaporation, room temperature radical polymerization), as well as co-polymerization of hydrophilic-hydrophobic compartments via simultaneous or subsequent polymerization of them monomer solutions added to the hydrophobic and hydrophilic parts of the chemically patterned surface.

To summarize this study, aqueous compartments on surface were investigated as a chemical and physical barrier to capture various low-surface-tension liquids (LSTLs) within designated closed-well-shaped patterns, for which hydrophobic-hydrophilic patterning within a core-shell structure was utilized. The aqueous barriers exhibited self-healing, adaptive, and other functional properties, such as the ability to extract chemicals through a diffusion process. These properties, attributed to the fluid state of the water walls, are challenging to replicate with traditional solid barriers. The use of liquid compartments came with limitations, including the maximum height of the water barriers and their compatibility exclusively with LSTLs that do not mix with water and other limitations, which were further investigated. These liquid-liquid wells enable the arrangement of LSTLs into complex quazi-two-dimensional patterns, offering precise control over volume without relying on fluorination, unlike other common superoleophobic or omniphobic patterning methods. Additionally, they can be utilized as molds for shaping polymers through a demonstrated water templated polymerization method. The water barrier, which does not bond with the polymer, can be easily removed and reshaped to varying heights, facilitating rapid prototyping of polymer layers. Such liquid enclosures are particularly beneficial in microfluidic devices for applications like on-chip extraction, phase-transfer catalysis, or reactions at interfaces. They also offer a unique opportunity to explore surface phenomena, including diffusion or the Marangoni effect, as the liquid-liquid interface is readily observable from above with CLSM. More broadly, using water-walls as a reusable mold could significantly reduce solid waste in scenarios requiring separation of organic compounds. Computational simulations employing a phase field model indicated that variations in surface tension at the liquid-air boundaries, driven by Gibbs adsorption, contribute to a stable tri-phase contact line (air-organic-water). This study showcases a method for creating entirely liquid, functional, self-repairing compartments for the containment and patterning of LSTLs and widens up the capabilities of on-chip liquid systems to multiple-liquid-systems without any solid barriers and complicated flow set-ups. At the same time, the method is easily compatible with various analytical methods, such as uv-vis, FTIR, Raman, optical and confocal microscopy, and could be potentially automatized and incorporated into flow microfluidics systems, which makes it very versatile and worthy of further development and exploration for chemical applications.

3.2 3D-printed organogels with solvent-assisted tunable behavior

The aim of this project was to investigate how various organic liquids can tailor the physical and thermal properties of organogels. The study also aimed to suggest a versatile and easily reproducible fabrication method for high-solvent-content organogels that was utilized via 3D-printing and consequent drying and swelling. By altering solvent types and conditions, the creation of organogels with behaviors ranging from adhesive to non-adhesive and thermal stabilities from below -15°C to over 100°C was enabled. Additionally, these organogels, when shaped into mesh forms, showed faster extraction processes by the optimized solvent-solute interactions.

3.2.1 Project Idea and Background

Organogels are a class of gels formed by a three-dimensional network and expanded substantially throughout its volume by liquid organic phase absorption.[28,56,207,274,275] Organogels exhibit a combination of properties coming from gelators, formed supramolecular or covalent polymer networks, liquid phase components, and their interactions, which enables their diverse functionality. As these organogels can be formed from a great variety of organic liquids and polymer networks, a tremendous range of properties is available.[28,275] Examples of organogels' properties coming directly from the swelling phase include photodegradability,[207] increased working temperature gap for electrically conductive gels,[223,276,277] promoted growth of nanocrystals and enhanced fluorescence, and boosted mechanical performance, such as their stretchability[278] or notch-resistance[279] Recent progress in the research of organogels has already shown their potential in the large scope of applications, including anti-adhesive[280] and self-cleaning surfaces,[231] drug carriers,[276,281] sensors,[282] actuators[55,218], and extraction vessels.[283,284] However, due to the present lack of research on this topic, many distinctive properties that the whole range of organic solvents can address to the gel, remain unexplored.[56] Therefore, to unleash the potential of organogels, it is important to develop new organogel materials and investigate their properties induced by the interaction of the specific liquid phases with polymer networks.

The current progress in universal and convenient fabrication methods for organogels has been limited mainly to films,[211,285,286]coatings,[287–289] and nanostructured bulk gels[278,287,290,291]. However, many real-life applications require precise control of the gel shape. Recently, irradiation through photomasks has been developed for structuring organogels to enhance their functionality. This technique has been used for the creation of liquid channels and gel photoresists,[207,292] the promotion of homeostatic growth of dynamic covalent polymer

networks,[293] and the fabrication of reversible organogel holograms.[294] Other developed techniques include mold-based micro-grooving for droplet sliding manipulation.[215] Although the most powerful tool for forming gels of arbitrary shape is 3D-printing,[295,296] there have been only a few published attempts to apply additive manufacturing to fabricate organogels. Zhang et al. demonstrated 3D-printable homogeneously luminescent organogels with complex free-standing architectures, not otherwise achievable for flexible perovskite gels.[297] O'Bryan demonstrated a method for 3D-printing of silicon-based structures through self-assembling micro-organogel based block copolymer in mineral oil.[298] This approach enabled the fabrication of branched perfusable silicon networks and functional fluid pumps. Despite the increasing progress in fabrication of 3D structured organogels, the full potential of fast and scalable production of organogels is yet not covered by the existing techniques, especially when it comes to fabrication of readily swelling organogels with high solvent content. The lack of research progress in 3D-printing of organogels restricts their application in advanced technology fields, such as soft robotics or biomimetic materials.

In this work, we show a convenient and tunable way to fabricate organogels via DLP 3D-printing and explore their behavior and properties depending on the composition of the ink, swelling solvents, and complexity of the macroscopic structure (**Figure 26**). For the printing process, we developed non-volatile inks based on mineral oil and conducted swelling after printing with multiple solvents compatible with the printed gels. Thus, we ensure increased solvent content (from 20-30 wt% up to 90 wt%) without losing printing resolution and demonstrate the versatility of the fabrication method. We investigate solvent-defined properties of organogels in bulk, such as tuneable thermal stability and swelling, as well as surface properties, including solid and wet adhesion. We provide a universal prototyping method that enables rapid production of structures without changing the synthesis procedure, using the same fabrication protocol for different application purposes. As an example of the added value of additive manufacturing, we demonstrate the improved capacity and absorption kinetics of organogels with complex architectures compared to the bulk gels for extraction of hydrophobic solvents, such as toluene, from water mixtures.
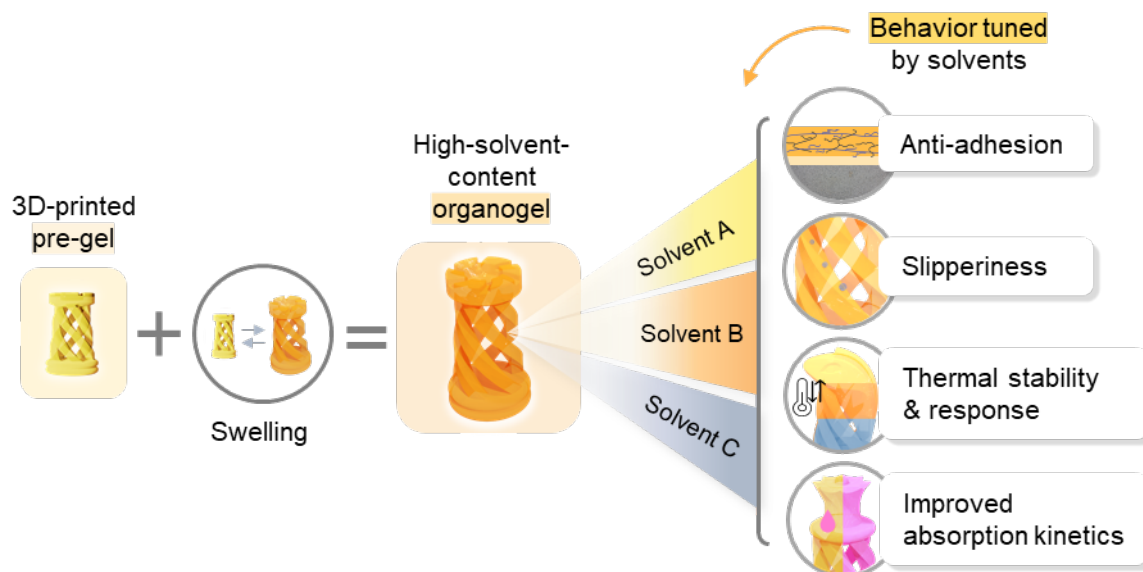
Figure 26. 3D-printed organogels with solvent-tuned properties. 3D-printing provides a free choice of shape and rapid production and enables better functionality. Solvent-defined performance is characterized in bulk, including thermal stability and response, swelling/shrinking, and absorption, and on surface, in terms of solid and wet adhesion.

3.2.2   Results and discussion

Organogels for this project were fabricated using DLP 3D-printing. The ink contained lauryl acrylate as a monomer, polypropylene glycol dimethacrylate as a cross-linker, a photoinitiator irgacure 379 (2-dimethylamino-2-(4-methyl-benzyl)-1-(4-morpholin-4-yl-phenyl)butan-1-one), and a biotolerant white paraffin mineral oil as a solvent (**Figure 27**). The exact compositions used for printing are listed in **Table 4.**
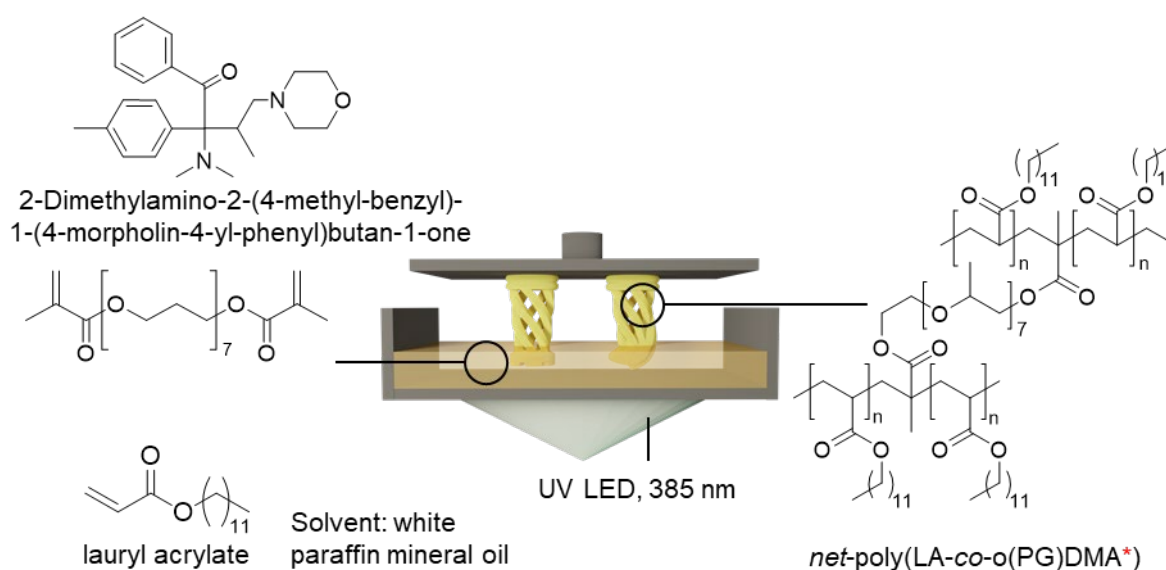
Figure 27. **Composition of 3D-printing inks and organogels.** Printing ink components, DLP-printing scheme, and resulting polymer composition are described.*o(PG)DMA in the name of the resulting polymer stands for oligo(propylene glycol) dimethacrylates.

Table 4. Description of the used printing inks. Several inks were tested to vary swelling behavior by adjusting cross-linker or monomer content. The name and function of each component are given in comments to the table

	Ink name	Composition
Decreasing the cross-linker content	LA80CL1	LA : mineral oil – 80 : 20 (w/w), o(PG)DMA – 1 mol% to LA, Irgacure 379 – 4w% to LA
	LA80CL0.75	LA : mineral oil – 80 : 20 (w/w), o(PG)DMA – 0.75 mol% to LA, Irgacure 379 – 4w% to LA
	LA80CL0.5	LA : mineral oil – 80 : 20 (w/w), o(PG)DMA – 0.5 mol% to LA, Irgacure 379 – 4w% to LA
Decreasing the monomer content	LA100CL1	LA : mineral oil – 100 : 0 (w/w), o(PG)DMA – 1 mol% to LA, Irgacure 379 – 4w% to LA
	LA80CL1	LA : mineral oil – 80 : 20 (w/w), o(PG)DMA – 1 mol% to LA, Irgacure 379 – 4w% to LA
	LA50CL1	LA : mineral oil – 50 : 50 (w/w), o(PG)DMA – 1 mol% to LA, Irgacure 379 – 4w% to LA

Comments to the table: LA – lauryl acrylate, *monomer*, *cross-linker*; Irgacure 379 – 2-Dimethylamino-2-(4-methyl-benzyl)-1-(4-morpholin-4-yl-phenyl)butan-1-one, *initiator*; mineral oil – white paraffin oil, *solvent*

After printing, the objects were put in n-isopropanol for 24 h and then dried in air for 3-8 h. The dried objects were then swollen in the respective swelling solvent to investigate their swelling behavior (the example of organogel dried and subsequently swollen in dyed toluene is shown in **Figure 28 A**). Spatially defined features are enlarged by the swelling process but retain the sharpness of details before (**Figure 28 B**) and after swelling (**Figure 28 C**). Therefore, the swollen 3D-printed organogels maintained complex shapes determined at the printing step (sharp, round, hollow, twisted), with the feature resolution remaining down to the sub-millimeter scale (**Figure 28 D**). Therefore, while the polymer network defined the shape, the dyed solvent influenced organogel bulk color, surface smoothness, and optical transparency.
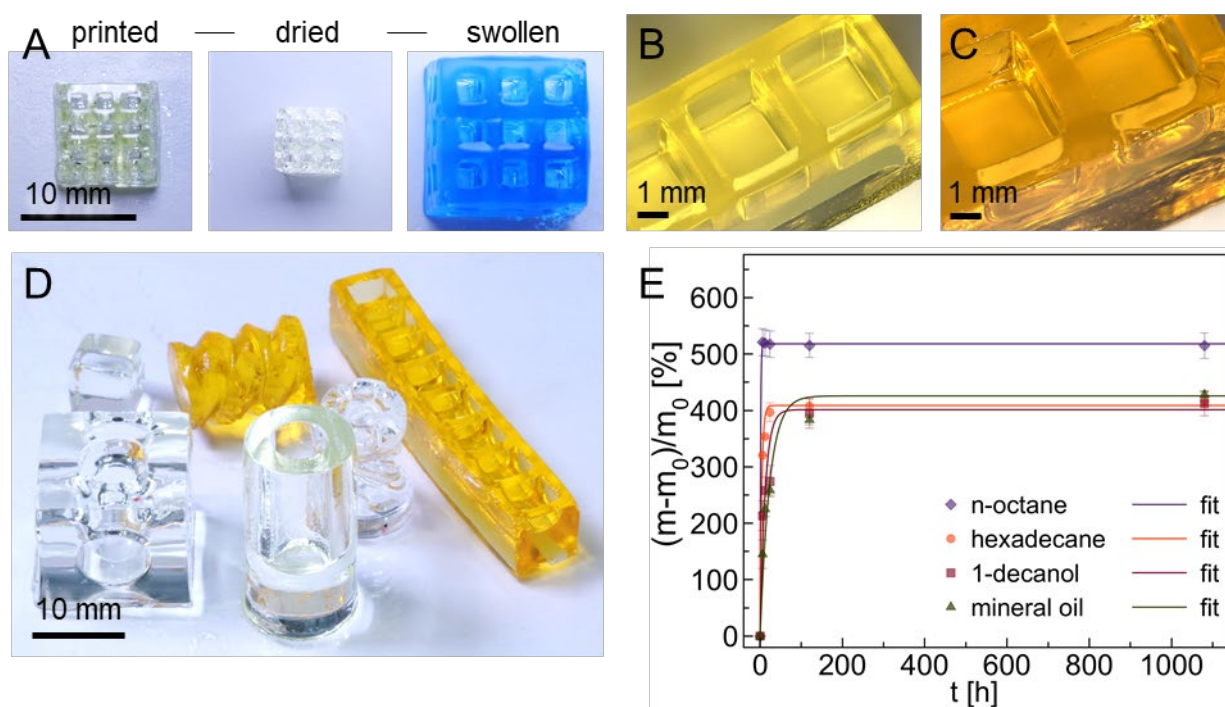
Figure 28. Swelling of 3D-printed organogel. (A) Organogel after printing (left), drying in isopropanol and air (center), and after swelling in Toluene dyed with Oil Blue O (right). The 3D structure of organogel is preserved from right after printing (C) to after swelling (B, D). The components of the printing ink and polymer composition are shown in Figure S1 A. (E) Swelling kinetics of organogel LA80CL1 for 45 days in various solvents. Dots are representing the average experimental values out of three independent swelling experiments. Lines represent the fit curves based on Voigt viscoelastic model (see **Figure 29** for the fit values). The exact composition of each printing ink is shown in **Table 4**.

The swelling kinetics varied for different solvents (**Figure 28 E**). The slowest and fastest reaching of the equilibrium were observed for 1-decanol and n-octane, respectively. For long-chain solvents, reaching the swelling equilibrium required from several days to a week, whereas, for n-octane, the swelling equilibrium was presumably reached in less than 12 h. Swelling kinetics was fitted by the Voigt viscoelastic swelling model, through which the swelling equilibrium and swelling rate coefficient could be calculated (**Figure 29**).
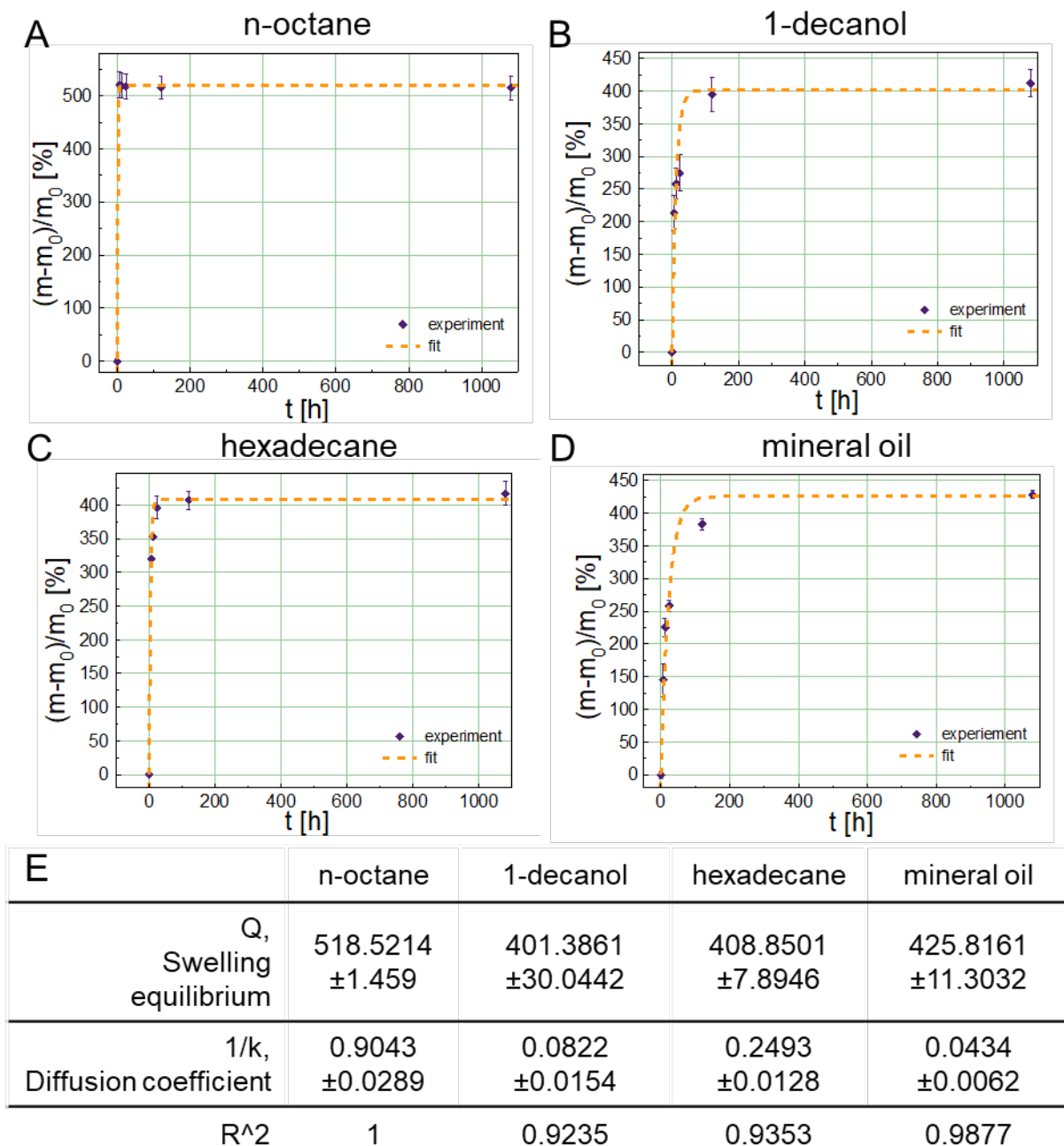
Figure 29. Swelling kinetics of organogel in various organic solvents. A-D) Experimental values and fitting curves of LA80CL1-based organogel swollen for 45 days in various solvents. Dots are representing the average experimental values out of three independent swelling experiments. Lines represent the fit curves based on Voigt viscoelastic model. E) A table with fitted values for swelling curves, including the swelling equilibrium, diffusion coefficient (or swelling rate coefficient), and the R2 parameter for each fitting function.

To further regulate the swelling equilibrium value, the cross-linker content was reduced from 1 mol% to 0.5 mol%, resulting in a faster uptake of the swelling liquid, from 350±5 wt% to 560±15 wt% (**Figure 30 A**, swelling solvent – 1-decanol). This change in swelling behaviour corresponds to the Flory-Rehner swelling equilibrium equation, according to which networks with higher cross-linking density exhibit reduced swelling capacity.[299,300] The control over the swelling ratio was also demonstrated by changing the monomer content in the ink (**Figure 30**

49

B, swelling solvent – 1-decanol), showing the importance of a weight ratio of a solvent to a monomer being at least 20:80 20 wt% of organic solvent in the printing ink to result in a less densely polymerized network with a higher swelling capacity. However, increasing the amount of the solvent to more than 50 wt% of the ink negatively affected the reactivity of the ink and led to the failure of printing even slightly complex, hollow or narrow structures. Therefore, we suggest lowering the cross-linker content as a preferable strategy to fabricate swellable 3D-printed organogels combined with the subsequent swelling to achieve 3D-printed organogels the higher (>90 wt%) solvent content.
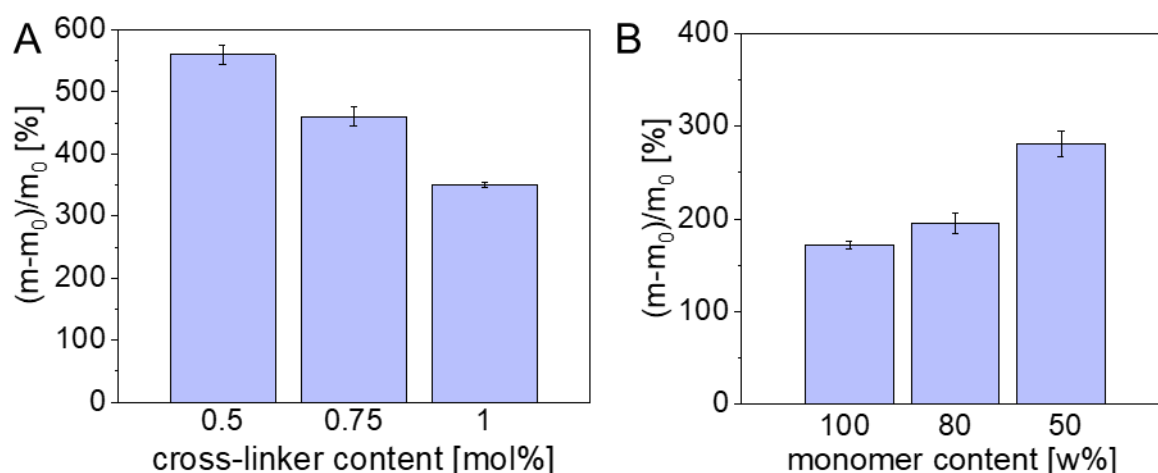
Figure 30. Swelling of organogels with the changing monomer vs. cross-linker content. Average swelling values for 24 hours in 1-decanol for with A) the cross-linker content varying from 0.5 to 1mol% to monomer (ink names from left to right: LA80CL0.5, LA80CL0.75, LA80CL1) and B) monomer to solvent ratio varying, the inks used: in the left - LA100CL1, no solvent in the ink, in the center – LA80CL1, the 80:20 ratio, and right – LA50CL1, the 50:50 ratio of the monomer LA to solvent, mineral oil. The exact composition of each printing ink is shown in **Table 4**.

Lauryl acrylate-based elastomers show considerably high wet and solid adhesion[301]. However, it has been shown in the present project to be completely overcome by swelling in a low surface tension solvent. To demonstrate the removal of organogel surface adhesion by swelling, we printed flat organogels (20 x 10 x 3 mm) and swelled them for 24, 48, and 72 h in the range of hydrophobic organic solvents. To characterize wet and solid adhesion, sliding angle measurements were performed, using 15 µl of water as a liquid (**Figure 31A, B**) and a 5 mm³ (0.91 g) neodymium cube (**Figure 31C, D**). The droplet shape analyzer platform was tilting from horizontal to vertical stand 1 degree per second, while the camera recorded the position of the drop or cube. The sliding angle was measured from the moment when the position of a water droplet or a cube changed from the initial while tilting.
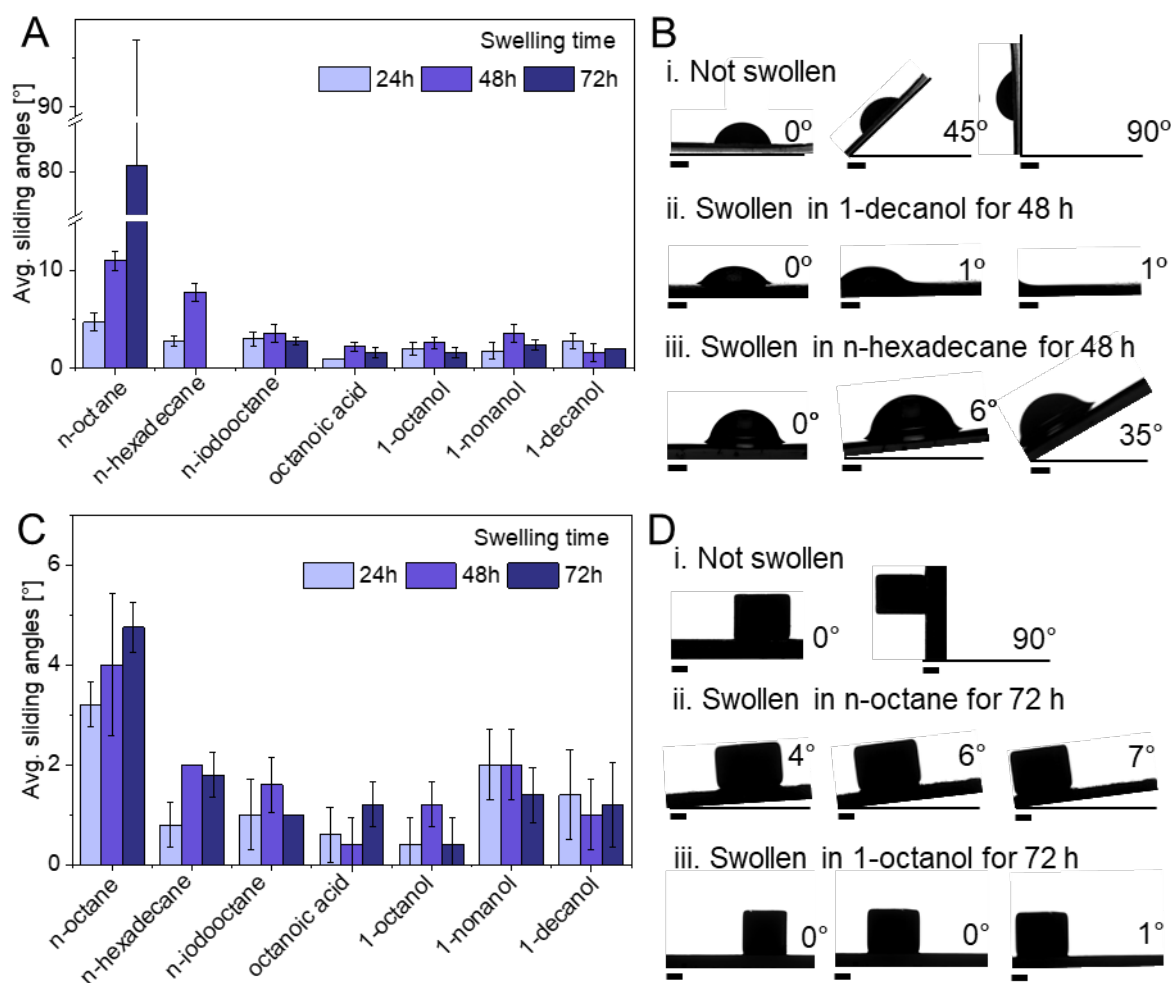
Figure 31. Wet and solid adhesion of organogel surface. (A) Sliding angles of a 15 µl water drop on organogel swollen in various solvents with different swelling times. (B) A 15 µl water drop is adhered to the surface of a non-swollen organogel (i) and sliding from the surface of an organogel swollen in 1-decanol (ii) and n-hexadecane (iii). (C) Sliding angles of a 5 mm³ neodymium cube on an organogel swollen in various solvents for 24, 48, and 72 h. (D) A neodymium cube is adhered to the surface of a non-swollen organogel (i) and sliding from the surface of an organogel swollen in n-octane (ii) and 1-octanol (iii). Composition of the ink: LA80CL1. Scale bar: 1 mm.

The non-swollen organogel showed liquid (**Figure 31B.i**) and solid (**Figure 31D.i**) adhesiveness, demonstrated by no sliding while turning up to 90 °C and back to 0 °C. This could be attributed both to the commonly known adhesive properties of lauryl acrylate-based elastomers[302], as well as less than 1n% amount of cross-linker used in the ink composition, which has been shown to increase the adhesive properties of the acrylate elastomers.[303] For swelling, hydrophobic solvents with different functional groups and chain lengths were chosen, including aliphatic hydrocarbons with varying chain lengths and boiling points (n-octane, n-hexadecane, 1-iodooctane), hydrophobic alcohols with varying aliphatic chain length (1-octanol, 1-nonanol, 1-decanol) and 1-nonanoic acid as fatty acid. All swollen gels demonstrated liquid and solid slippery behaviour up to a full loss of adhesion (the object starts sliding already without tilting). What was noteworthy however, is that the efficiency of lubrication increased

from aliphatic hydrocarbons to hydrophobic solvents with additional functional groups. Based on the average sliding angle for all swelling times (24, 48, 72 h), the best combination of liquid and solid adhesion was demonstrated by 1-octanoic acid and 1-octanol. Given that the shorter swelling times did not have a substantial effect on gel slipperiness (**Figure 31A** and **Figure 31C**), one could assume that the solvent lubrication layer on the surface contributes more to anti-adhesion than the extension of the polymer network caused by swelling. The liquid lubrication level was retained by the gel for more than 10 cycles and could be restored after multiple uses by gently pressing or shortly dipping in the reservoir with the swelling solvent.
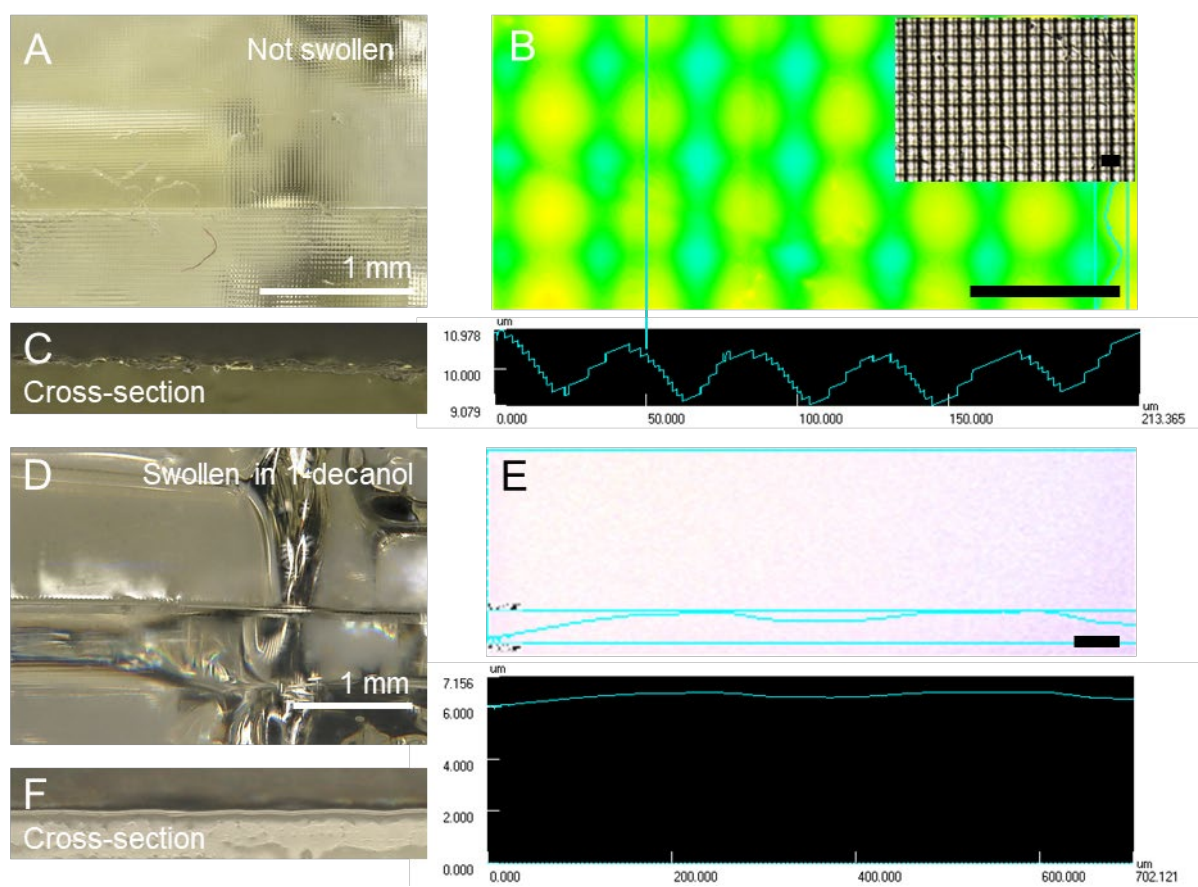
Figure 32. Surface morphology of 3D-printed organogels. Digital and laser optical microscopy of organogels before (A-C) and after (D-F) swelling in 1-Decanol. After printing, organogel surface inherits roughness square pattern, with area of each square 40 µm² (A, C) – the size of 1 digital mirror in the digital mirror device of the 3D-printer, and depth of several µm (B). After swelling, the lubrication by the solvent and extension of the 3D-network, the surface appears smooth (D, F) and no initial roughness is observed (E). Profiles on the Figures B and E were performed with the optical laser profilometry across the surface of the gel. Axis Y of the profile represents depth, axis X represents the length of sample along which the profile was measured. Black scale bars: 50 µm.

To investigate the possible morphology influence on the adherent vs. slippery behaviour of the non-swollen and swollen organogels, the top surface and the cross-section of the gel profile (after cutting the gel in half), as well as the roughnesses of the gel's surface before and after swelling were imaged via digital and optical laser microscopy (**Figure 32**). Due to the "voxel"-

based curing of each layer, 3D-printed organogel inherited the printing artefact in a form of the square pattern on the surface with a depth of several µm and area of ca. 40 µm². The area of each "square" corresponds the size of one digital mirror in the digital mirror device of the printer, and is caused by the differences in the light irradiation intensity in the corners vs. in the middle of the "voxel", while the depth of the pattern could be dependent on the layer thickness, laser overall intensity, resin reactivity and curing time. Because of this artefact, coming from the fabrication method, 3D-printed gels showed the optically limited transparency and surface roughness. However, imaging of the gels after swelling showed the improved smoothness of the surface (from ca. 5.4 µm roughness depth for the non-swollen gel to less than 0.5 µm for the swollen gel, based on the optical laser-based profilometry, as shown at B and E), which can be attributed both to the lubrication of the surface by the swelling liquid and to the filling of the gel volume by the solvent with the following expansion of the gel network.
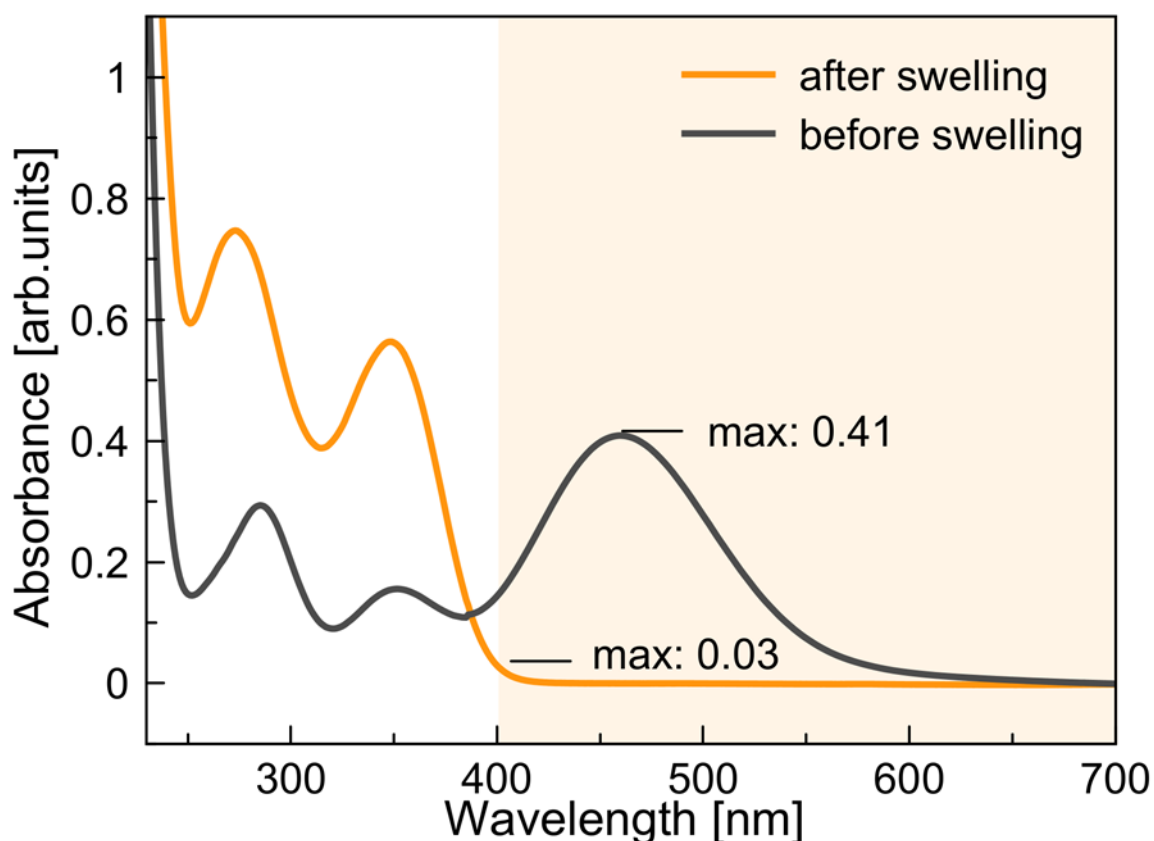
Figure 33. UV-VIS absorption spectrum of non-swollen and swollen organogel. The light orange area represents the visible region, with the indicated maximum values in arb. units for the organogel before swelling (black spectrum) and after swelling (orange spectrum).

Additionally, both by expansion of the network and "smoothening" of the printing artefacts by the process of swelling, the transparency of the organogel significantly increased in the visible

spectrum region (from max. 0.41 transmission in the non-swollen state to the max 0.03 transmission in the swollen stat, calculated based on the absorbance at 400-700 nm wavelength range, as shown at **Figure 33**). Similar effect of swelling improving the gel transparency properties has been previously demonstrated by ZHANG ET AL for the underwater dynamic transparency of non-printed organogels.[301] In this work, it has been demonstrated that swelling has the smoothing and levelling effect on the printing artefacts, as well as the enables better transparency for the printed parts, which could be a promising post-processing method for DLP 3D-printed visco-elastic objects.
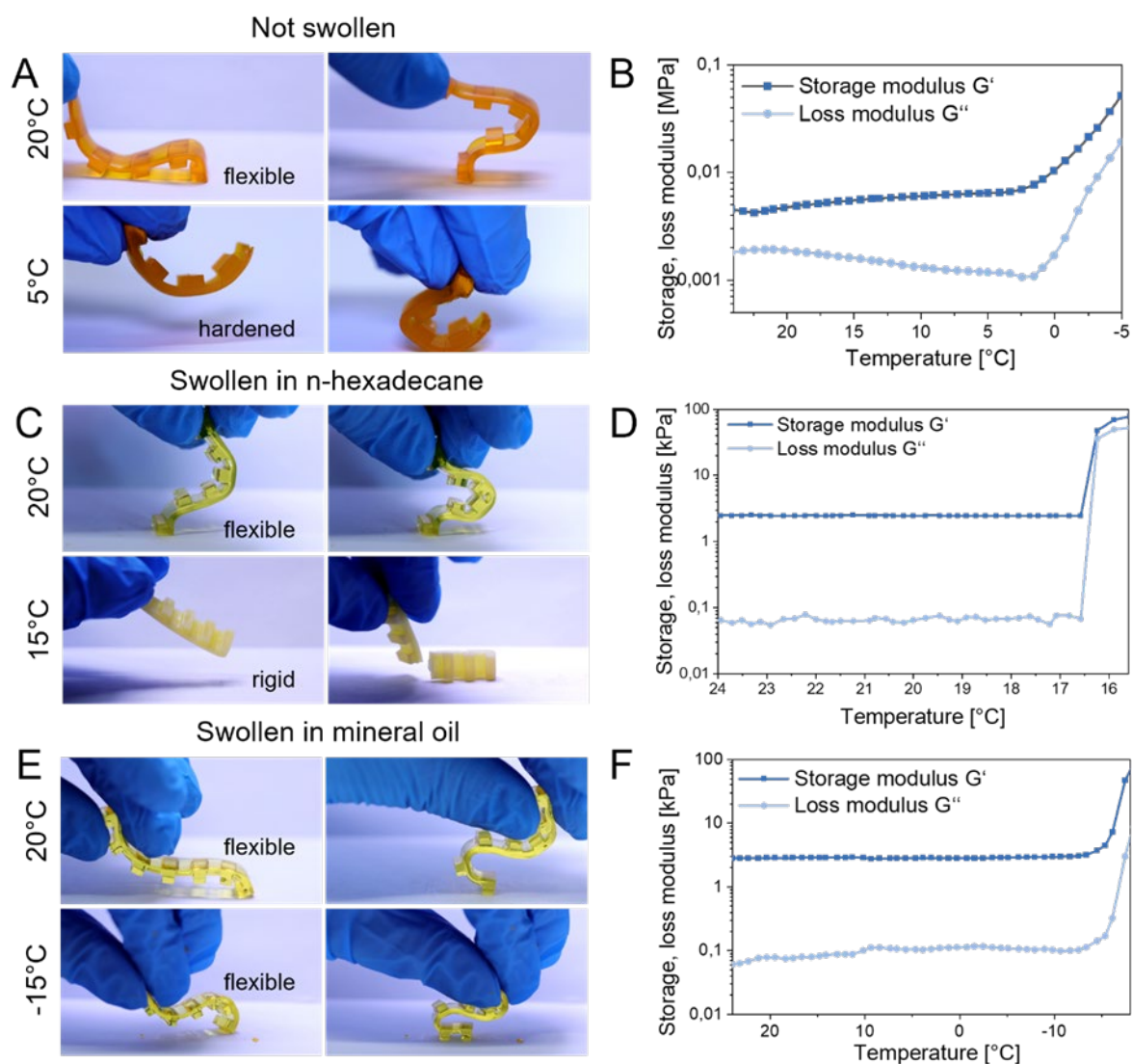
Figure 34. Organogel thermal-mechanical stability tuned by swelling and a choice of solvent. The illustration of the cooling-caused changes in flexibility and temperature sweep rheology for a non-swollen organogel (A, B) and organogel swollen in hexadecane (C, D) versus organogel swollen in mineral oil (E, F) for 72 h. Ink composition LA80CL1.

Organogels before and after swelling in various solvents exhibited changing rheological behaviour and thermal stability. Changing the swelling solvent determined the temperature range of organogel flexibility, as well as thermo-responsive stiffening and softening. This phenomenon was investigated by temperature sweep rheometry (**Figure 34**). Upon cooling to near 0 °C, a non-swollen organogel was gradually hardening and losing its flexibility (**Figure 34 A**), which was indicated by the rising storage and loss modulus (**Figure 34 B**). When swollen in an organic solvent with a high melting point, organogel exhibited a rapid thermo-responsive switch from soft viscoelastic to stiff behaviour at the melting point of the swelling liquid, hexadecane (T_m = 18.18 °C[304]) demonstrated in **Figure 34 C, D**. When swollen in a solvent with a lower melting point, such as mineral oil (MP ≈ −15 °C, information from the manufacturer), organogel retained the flexibility at a much larger temperature range with a similar rapid hardening behaviour when reaching the melting point of the solvent (**Figure 34E, F**).

Notably, the stiffening of the organogel at the melting point of the swelling liquid could be reversed with subsequent heating of the gel, and this way multiple stiffening-softening cycles could be repeated without the degradation of the mechanical stability (**Figure 35**). Therefore, the high solvent content can enable temperature-dependent dynamic behaviour of the organogels. By switching to a swelling media with the different melting point, one could tune the temperature of the stiffening-softening switch.
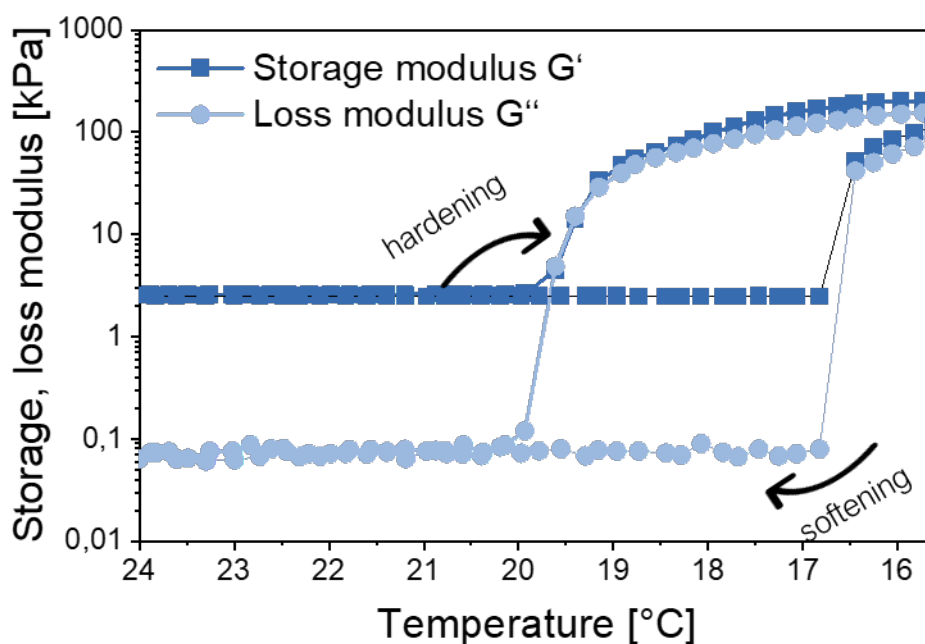
Figure 35. A full cycle of organogel reversible softening and hardening. Organogel was printed from the ink LA80CL1 and swollen in hexadecane for 72 h. Additionally, the temperature range where the swollen

organogels retain their mechanical behaviour, showed to not be limited to low-temperature stability. By performing rheology in the temperature range 25-100 °C on the non-swollen organogel and organogel swollen in hexadecane for 24 h, we have demonstrated that for the non-swollen gel, the fluctuation of the detected loss modulus was observed in the whole heating range (**Figure 36A**). However, for the organogel swollen in the high-boiling-point solvents both storage and loss modulus of the organogel were stable at temperatures up until 100 °C (**Figure 36D**).
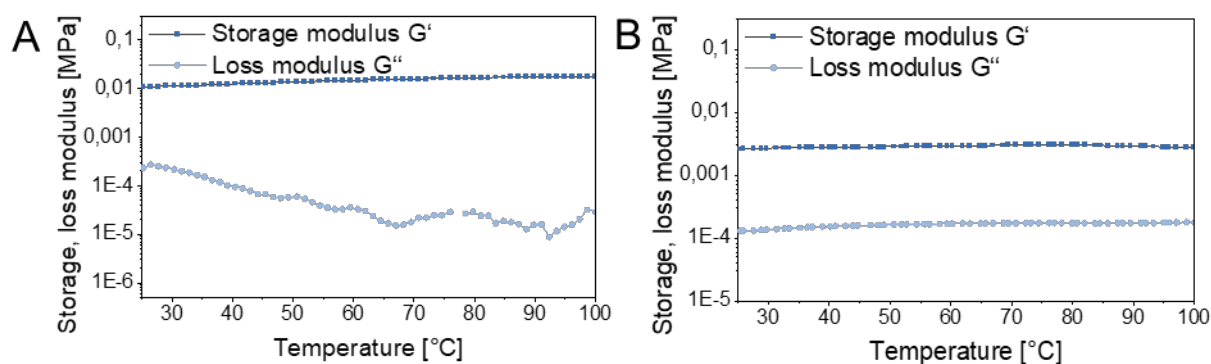
Figure 36. Organogel high-temperature thermal mechanical behaviour. Temparature ramp of (A) non-swollen and (B) swollen in hexadecane for 73 h organogel over the range 20-100 °C.

Thus, high-solvent-content organogels demonstrate not only solvent-induced tuneable mechanical behaviour, such as reversible dynamic stiffening-hardening, but also the ability to tune the preservation of the mechanical properties at low as well as high temperatures by adjusting the swelling phase.

Additive manufacturing enables not only rapid prototyping of materials but also a greater choice of shapes. For instance, the mold polymerization, standard for producing organogels, cannot produce hollowed or meshed materials, which are crucial for their high surface-to-volume ratio in absorption or extraction applications. For example, hollowed-out and meshed materials cannot be produced by mold polymerization, although such structures are important for their surface-to-volume ratio in applications for absorption or extraction, or in polymer-based devices, such as, microfluidics. To demonstrate the influence of the complex 3d-printed shape of the gel on the swelling kinetics, the swelling process of meshed and bulk 3D-printed cubes in toluene was compared (**Figure 37**).
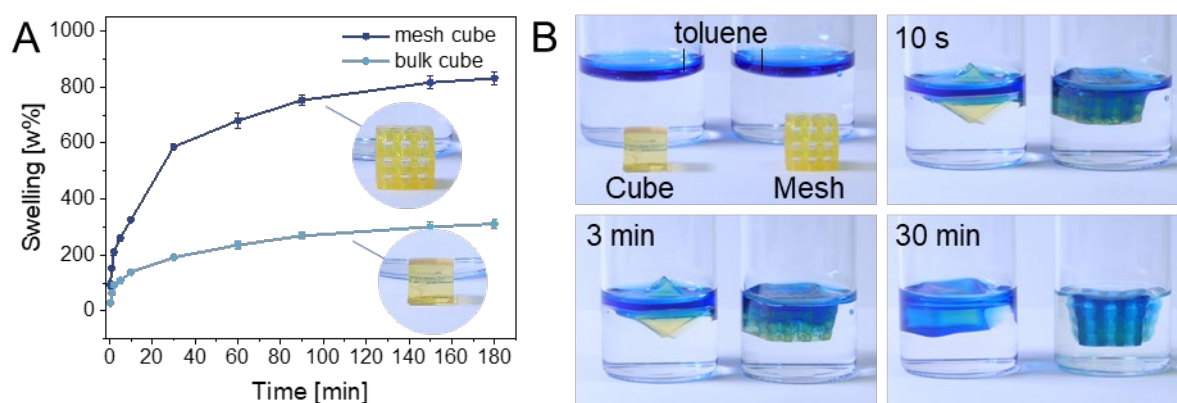
Figure 37. Extraction efficiency of a bulk cube vs. a mesh organogel. (A) Swelling process of bulk and meshed organogels in toluene. (B) Extraction of the dyed with Oil Blue N toluene layer on water surface by bulk and meshed organogel. Ink composition: LA80Cl0.5. The size of one side of the bulk cube (dry): 5.5±0.5 mm, the size of one side of the mesh cube (dry): 6.2±0.5 mm, one mesh section: ca. 1 mm wide.

The meshed cube exhibited faster diffusion of the solvent and easier access to the bulk, resulting in a higher mass uptake of over 800 wt% within 3 h. In contrast, the bulk cube with identical composition and volume had significantly slower diffusion than a hollow mesh, which slowed down the speed of the diffusion from all directions through the gel, according to the Fick's law of diffusion.[305] Apparent mass uptake of the bulk cube after 180 min resulted only at ca. 200 wt% (4 times less than for the meshed gel). To illustrate this effect, we recorded the toluene uptake from the toluene-water mixture by the bulk and mesh organogels (**Figure 37B**). The meshed cube swelled and consumed the whole toluene layer within 30 minutes, whereas the bulk cube's swelling and solvent uptake is taking much longer. To identify the swelling equilibrium and the swelling rate coefficient, several fitting functions have been compared, with the power law equation showing the closest fit (**Figure 38**). According to the fit curve, swelling equilibrium of the meshed cube has resulted at 845±48.0786 wt% (parameter A in the fitting formula), whereas for the bulk cube it led to maximal mass uptake of only 200 wt% (4x after 180 min), followed by a declining diffusion rate. These results demonstrate that advanced shapes attainable through 3D printing can largely improve the performance of the same material and bring it closer to practical applications.
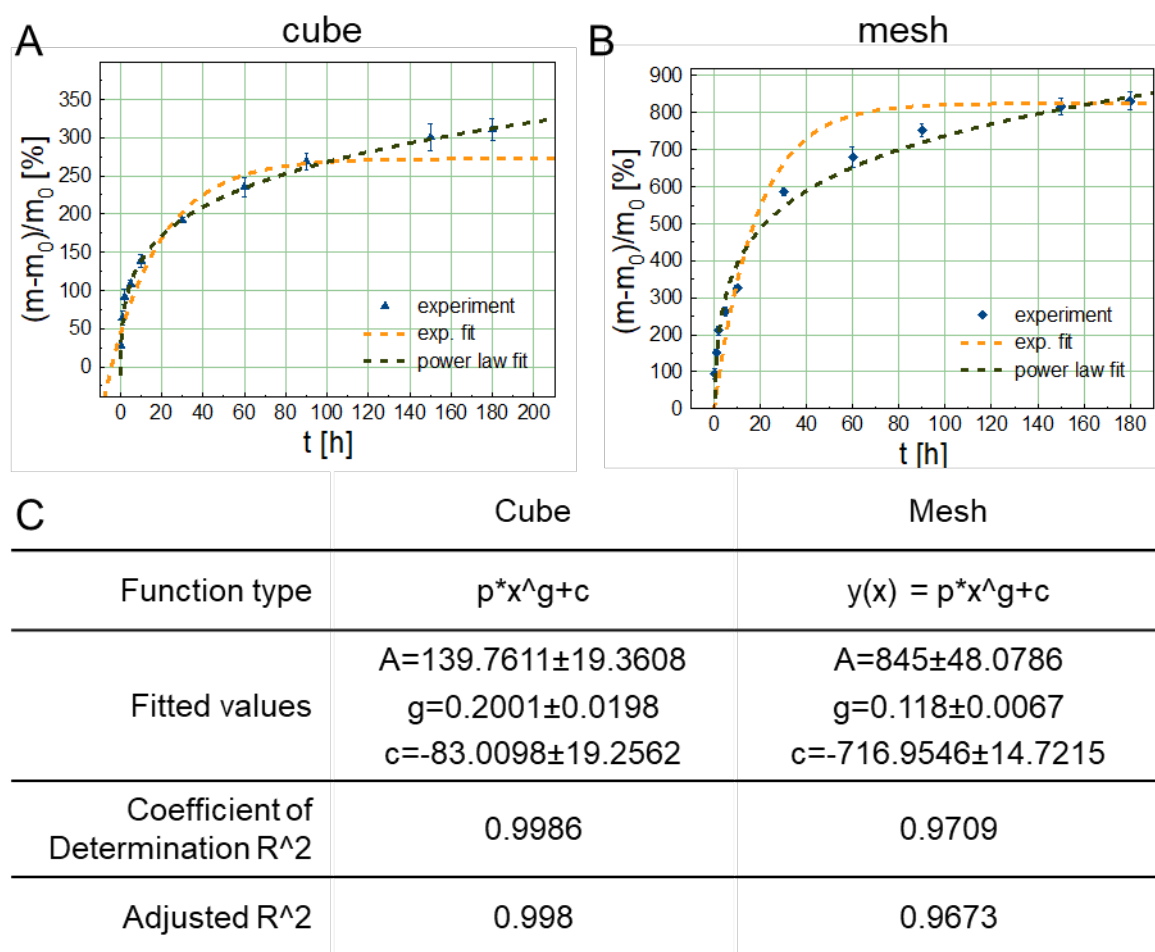
Figure 38. Swelling kinetics for a bulk cube vs. a mesh cube organogel.

In summary, this study has investigated the significant potential of organic liquids as swelling solvents to influence the properties of gels. Through photopolymerization-based 3D printing and subsequent swelling in various solvents, a versatile and adaptable fabrication method has been demonstrated for high-solvent-content organogels. By adjusting factors such as ink compositions, swelling times and swelling media, organogel properties could be largely tuned, upscaling their range of functionalities. In this study, various hydrophobic solvents have been applied as swelling media for organogels with the same polymer composition, including medium-chain alcohols, toluene, mineral oils, and fatty acids. Organogels that swelled in hydrophobic liquids transitioned from adhesive to liquid and solid-slippery behaviors, eventually losing adhesion completely. Furthermore, by changing the swelling solvents, one could tune the thermal behavior of organogels, expanding their thermal stability from -15°C to over 100°C. This adaptability also allowed for reversible hardening-softening cycles, with the switching point at the melting point of the dispersed liquid media. Capitalizing on the inherent hydrophobicity and solvent-confinement capabilities of organogels combined with the complex

3D-printed shape, they were demonstrated as mesh-shaped extraction vessels to optimize surface area, enhancing interactions between non-polar solvents and solutes in aqueous media. This approach significantly improved absorption kinetics, offering new capabilities for organogels in extraction processes.

In conclusion, the combination of organogels with swelling in a broad range of organic solvents, when combined with additive manufacturing techniques, opens a large range of properties and new horizons for organogel applications, from advancing extraction processes to contributing to developments in soft robotics and smart multi-responsive polymers.

3.3 Polymerization-induced phase separation to create 3D-printed inherently porous stiff materials

In this project, the unique ability of organic solvents to manipulate the polymerization-induced phase separation process was utilized in combination with DLP 3D-printing to create stiff light-weight materials with inherited nano- and architecture macro-porosity. The focus of the study was pointed at the investigation of polymer structures that achieve a significant weight reduction without compromising mechanical durability through a well-defined macroporous geometry. The use of organic solvents in the ink composition is critical for controlling pore size and density, thereby directly influencing the stiffness of the material. Further, ultra-sensitive mechanical nano-indentation testing was combined with computational methods to delineate the structure-property relationships, highlighting how the printing ink composition and printing parameters affect the materials' mechanical characteristics.

This project was done and published in a collaboration with the groups of PROF. RUTH SCHWAIGER (the parts with mechanical testing and analysis) and PROF. SHU-WEI CHANG (the computational analysis part).[306]

3.3.1 Project Idea and Background

The process of polymerization-induced phase separation facilitates the precise control over the porous structure of polymers in a singular step.[307] This process, initiated by the increasing incompatibility of the growing polymer chains with the liquid porogen, results in the formation of a biphasic liquid-solid system.[308] The following elimination of the liquid phase yields structures that are continuously porous from the nano- to the macro-scale without the need for sintering or the use of blowing agents, unlike what is necessary for ceramics or polymer foams.[309,310] It has been discovered that the phase separation induced by free-radical polymerization is possible to use with sophisticated manufacturing techniques, particularly stereolithography.[311] This research demonstrates a method that merges the bottom-up self-assembly of nano-porous polymers through phase separation with the top-down 3D-printing approaches of DLP (digital light processing)[162] and two-photon polymerization.[311] This approach allows for the creation of structures that have ordered 3D printed architectures and are inherently porous. Despite the simplicity of this method and the high resolution of the printing, questions remain regarding how to control the elastic properties through design and the relationship between the materials' structure and their properties. The challenge of accurately predicting mechanical behavior and controlling microstructure in materials with randomly distributed pores has remained a significant limitation for the method.[312] At the same

time, porous polymers, inherently less dense than their solid counterparts, are being explored for applications in construction and as biomaterials due to their lightweight nature.[313,314] Research in 3D-printing hierarchical porous polymers has been reported, including the printing of carbon nanotube/chitosan composites,[315] conductive TiO_2-$Ti_3C_2T_x$ heterojunction/rGO/PDMS composites with a vertical porosity gradient,[316] and rGO@Fe_3O_4/rGO@MXene/polydimethylsiloxane composite materials.[317] While increasing porosity can reduce weight, it often negatively impacts mechanical properties like stiffness and fracture toughness.[318,319] However, 3D-printed materials with carefully designed porous architectures can exhibit mechanical properties superior to those of the bulk material. Different lattice geometries can achieve higher stiffness-to-weight ratios thanks to their well-defined cellular architecture.[314,320–323] In some microporous or meta-biomaterials, traditional correlations between strength and Young's moduli are altered, allowing the design of materials with specific mechanical properties.[324–327] The stiffness of these structures can be adjusted by changing the strut dimensions, cell numbers,[328] and strut and node geometries through printing parameters.[329] This leads to the potential for developing new lattice-based architectures from materials whose mechanical parameters have been accurately measured.

This study aimed to broaden the toolkit and perspectives for future exploration of phase-separation-induced porous polymers in the creation of lightweight 3D-structured materials. For that, we created and categorized porous materials with various pore sizes: nano-porous (up to 1 µm), micro-porous (1 to 10 µm), and macro-porous (3D printed pores larger than 100 µm). Furthermore, this study investigates the mechanical properties of 3D-printed inherently porous polymers through micro-compression testing with a nanoindenter and simulations that model elasticity, porosity, and stress distribution using the Lattice Spring Model.[330–332] We explored how variations in composition and printing layer thickness influence mechanical properties, employing both experimental techniques and simulations.

3.3.2   Results and discussion

To create the structures with porosity induced while photopolymerization, the DLP (digital light processing) 3D printing technology was employed. The idea, as described in the introduction part, was to combine the nano-porosity coming from the phase-separation and following elimination of the organic solvent via critical point trying and architecture macroporosity created via 3D-printing (**Figure 39** A). The key to developing and controlling porosity lies in the phase separation of polymer particles from a porogen solvent, a critical aspect of the method.

For this purpose, the hydrophilic monomer hydroxy ethyl methacrylate (HEMA) and the cross-linker ethylene glycol dimethacrylates (EDMA) were chosen. In turn, a biphasic system of high-boiling-point hydrophobic porogenic solvents, specifically cyclohexanol and 1-decanol, was used to initiate the phase separation, when the growing oligo-(HEMA-EDMA) chains became immiscible with the liquid phase of the ink. In this work, tetrahedral lattice architecture was used to create macropores and further decrease the weight of the material while preserving its mechanical stiffness. The impact of the printing parameters on the porous architecture and its mechanical properties was assessed across a set of samples. This set included variations in two key aspects: 1) the ratio of the co-porogens 1-decanol to cyclohexanol, and 2) the thickness of the printing layers. This resulted in nine distinct compositions (identified as samples M1-M9, as depicted in **Figure 39** B). Details on the specific fractions of porogens, monomers, and the dye used in each ink formulation, are provided in **Table 5**.
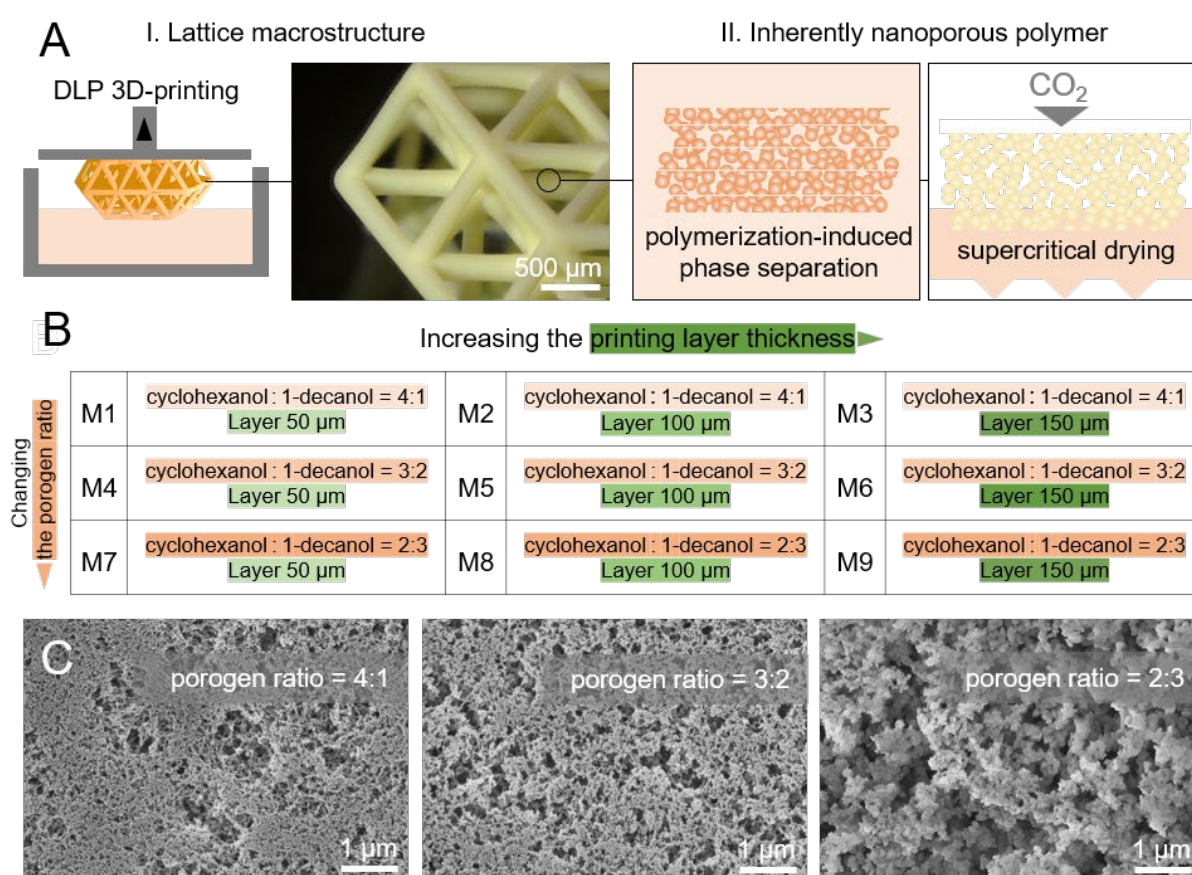
Figure 39. Fabrication of micro- and macro-porous polymers via DLP 3D printing combined with polymerization-induced phase separation. (A) Fabrication scheme. (B) Description of sample naming. Samples M1-M9 were printed from inks* with three different porogen ratios (cyclohexanol : 1-decanol) (rows) and various printing layer thicknesses increasing from 50 µm to 150 µm (columns). (C) Microscopy images show changing porosity and the size of particle agglomerates with porogen ratio changing from 4:1 to 2:3. *Detailed composition of each ink is given in **Table 5**.[306] Reproduced from KUZINA ET AL. with permission. Copyright 2023, Wiley-VCH.

The adjustment of the 1-decanol to cyclohexanol ratio in the porogen mixture was the main way in this study to shape the surface morphology of the printed structures. As the proportion of 1-decanol was increased from 25 wt.% to 60 wt.%, a noticeable transition in the surface texture was observed. Initially, the structure showcased a compact network featuring small granules and micropores under 1 μm (as seen in **Figure 39** C, left). However, with a higher ratio of 1-decanol, this evolved into a formation of larger particle agglomerates and expansive interconnected pores that could reach sizes up to 10 μm (illustrated in **Figure 39** C, right).

Table 5. Ink compositions with the varied co-porogen ratio.[306]

Ink 1	Ink 2	Ink 3
Samples M1-M3	Samples M4-M6	Samples M7-M9
30 wt.% HEMA,	30 wt.% HEMA,	30 wt.% HEMA,
20 wt.% EDMA,	20 wt.% EDMA,	20 wt.% EDMA,
40 wt.% cyclohexanol,	**30 wt.% cyclohexanol,**	**20 wt.% cyclohexanol,**
10 wt.% 1-decanol,	**20 wt.% 1-decanol,**	**30 wt.% 1-decanol,**
1 wt.% Irgacure 819,	1 wt.% Irgacure 819,	1 wt.% Irgacure 819,
0.1 wt.% Sudan I	0.1 wt.% Sudan I	0.1 wt.% Sudan I

To examine the morphology and to test mechanical characteristics of the base porous material for each of the compositions described above, a series of cylinder-shaped pillars with a diameter of 500 μm and a height of 1.5 mm was first printed. The pillars were printed and dried via critical point drying process directly on the glass substrate to avoid any mechanical destruction before the mechanical testing (**Figure 40**).
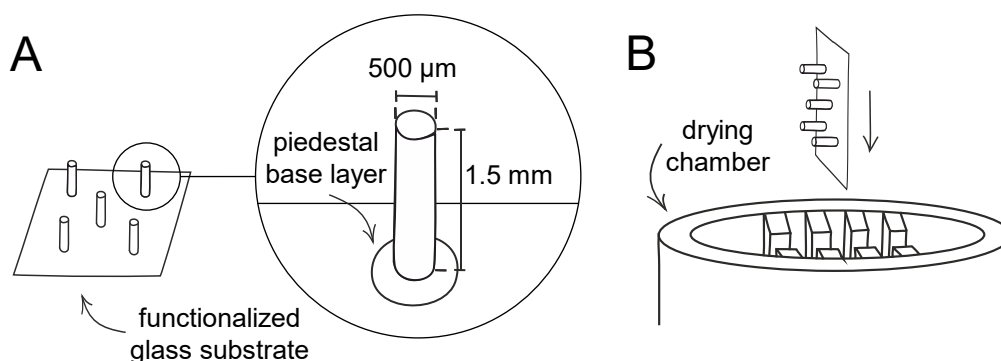
Figure 40. Scheme of the sample preparation. For each composition of samples M1-M9, 5 pillars are printed on the functional substrate (A). The substrate with the pillars is dried vertically in the critical point dryer chamber (B).[306] Reproduced from KUZINA ET AL. with permission. Copyright 2023, Wiley-VCH.

It is important to mention that other printing artefacts were spotted for the printed pillars (**Figure 41**). Increasing the printing layer thickness generally decreased the printing quality by

creating a visible inhomogeneity in a form of conic layers. Also, for some pillars, the number of layers didn't correspond the digital model which means that some new layers didn't attach to the object while irradiating. These artifacts would also potentially negatively affect mechanical testing results. Therefore, the samples were inspected after printing and before the following tests to ensure decent sample quality.
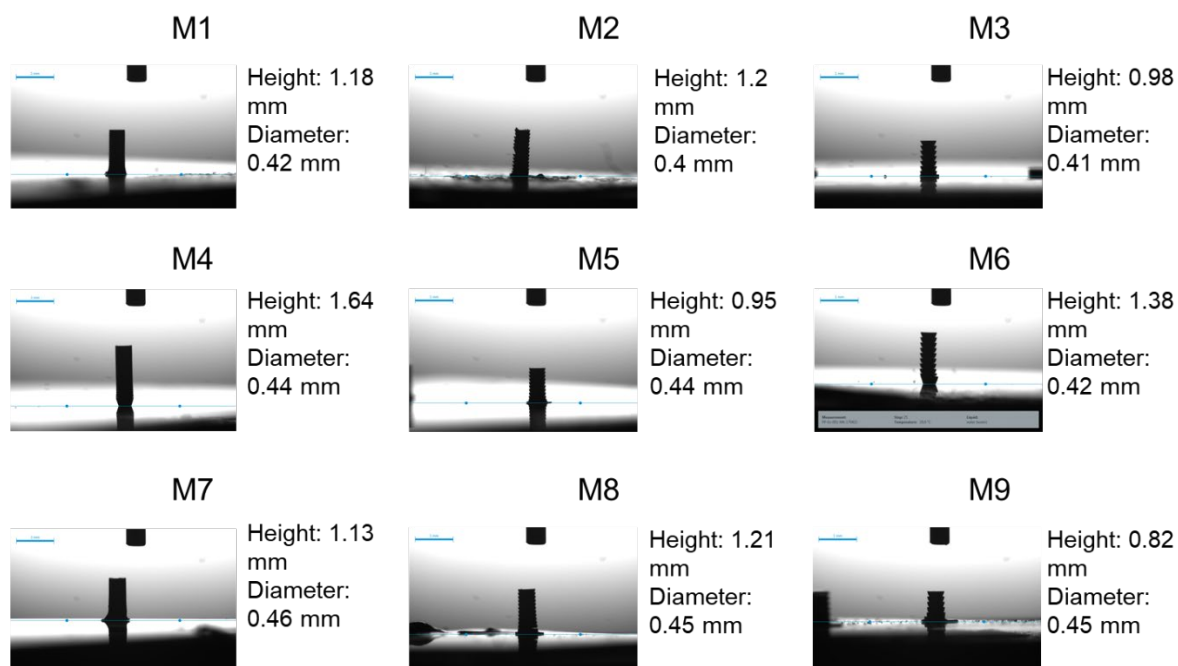
Figure 41. Printing artefacts: pillars heights and diameters. Images are taken with the camera of a contact angle goniometer. Scale bars (blue): 1 mm.[306] Adapted from KUZINA ET AL. with permission. Copyright 2023, Wiley-VCH.

The impact of printing layer thickness on morphology was also documented via electronic microscopy imaging. The printing layer thickness increasing from 50 µm to 150 µm led to more pronounced inhomogeneity in pore sizes (**Figure 42**). Furthermore, a grid-like pattern became apparent for the thicker printing layers, each grid element measuring approximately 40 µm across, mirroring the "voxel" size of the printer. This phenomenon is attributed to the scattering of projected light across a larger volume for the thicker printing layers, which in turn, results in diminished polymerization rates at the voxel edges. As a result of this printing artifact, regions with higher (second column in **Figure 42**) and lower (third column in **Figure 42**) density areas are formed which potentially could negatively affect material's mechanical properties.
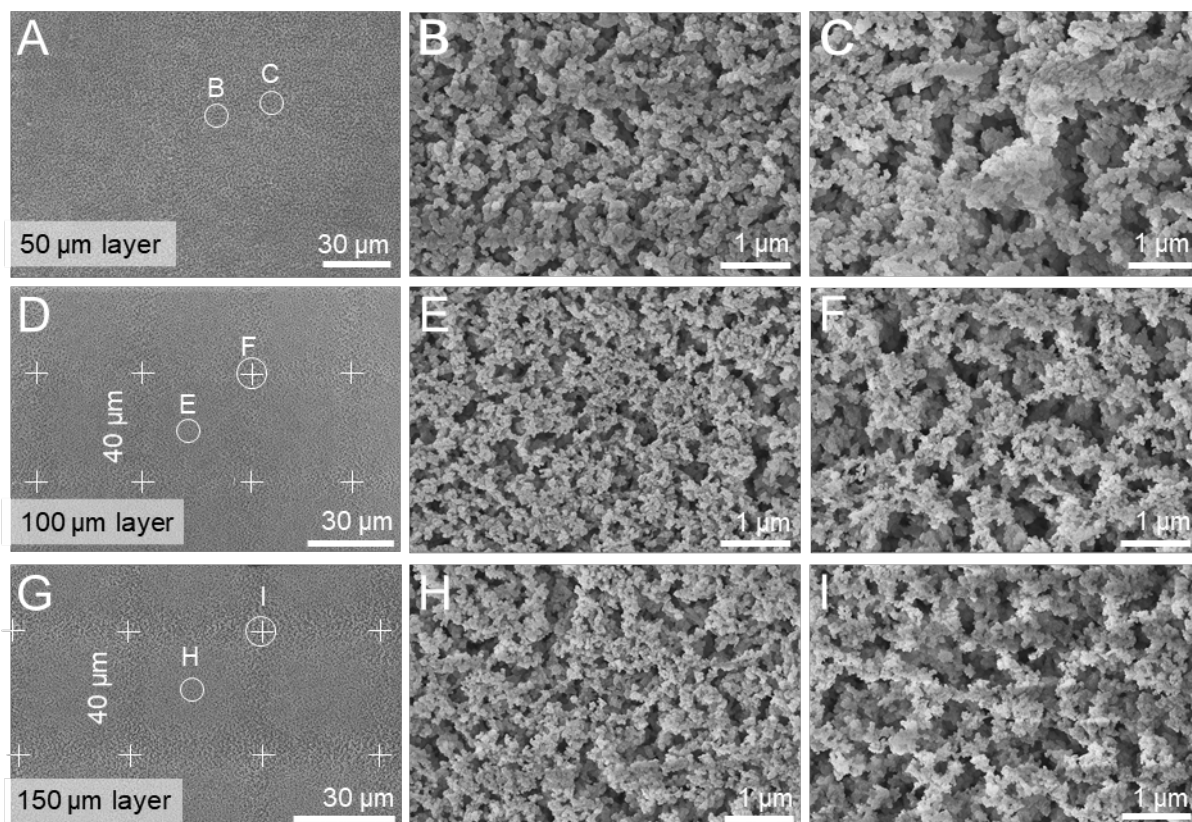
Figure 42. Microscopy images of samples M7-M9. The samples have (porogen ratio cyclohexanol : 1-decanol equals 2:3, the printing layer thickness is varied): (A)-(C) 50 μm printing layer, sample M7; (D)-(F) 100 μm printing layer, sample M8, (G)-(I) 150 μm printing layer, sample M9. For the 100 μm (D) and 150 μm (G) printing layers, a "voxel grid" is visible, which is a printing artifact of DMD mirrors(B,E,H).[306] Reproduced from KUZINA ET AL. with permission. Copyright 2023, Wiley-VCH.

The quantitative evaluation of the particle agglomerates' size, considering their irregular shape, was done by estimating the mean Feret's diameter from the microscopy images in **Figure 39** C and **Figure 42**. The value, representing the average length across an agglomerate confined within two parallel planes, was calculated for the samples M1, M4, and M7 , resulting in 27 ± 11 nm, 37 ± 13 nm, and 83 ± 19 nm, respectively (**Figure 43** A). Therefore, the average "grain" size in the polymer network increased with increasing the portion of 1-decanol in the porogen ratio. When comparing the series of samples with varying thickness layers, the average agglomerate size, also measured in a form of a mean Feret's diameter), the opposite effect was observed (**Figure 43** B). The increased thickness layer led to the decreased average particle size. Presumably, this could be related to less irradiation per area and therefore decreased polymerization ratio. These results underline how both changing the ratio of two solvents in the porogen mixture and printing parameters affect not only porosity, but also polymer structure, from smaller polymer particles into significantly larger agglomerates, and from dense continuous networks to looser structures with larger pores.
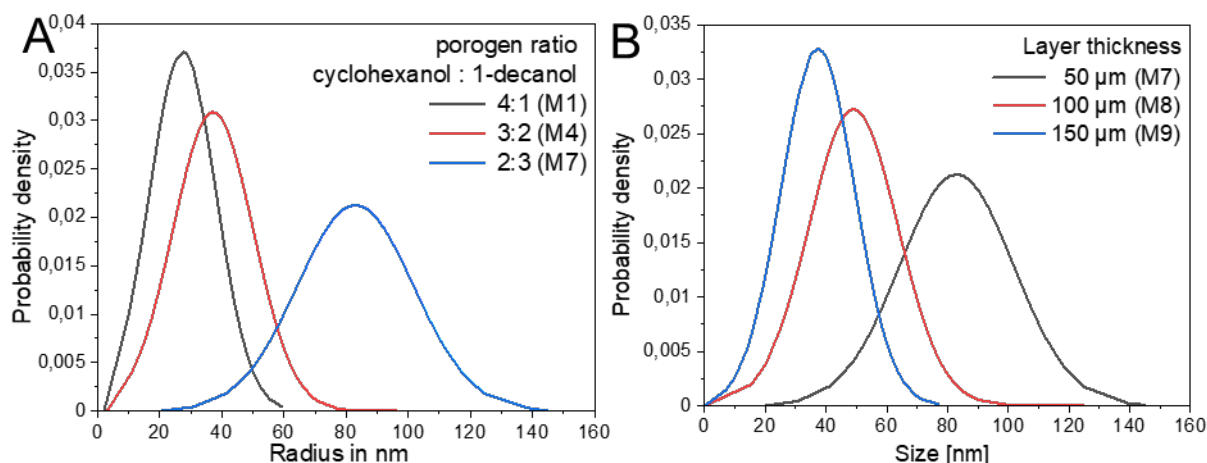
Figure 43. Particle agglomerates' size distribution. Graphs correspond the samples with (A) varying porogen ratio (M1, M4, M7) and (B) varying layer thickness (M7, M8, M9). Particles size was measured by the Feret's diameter of granular structures based on microscopy images shown at **Figure 39** C and **Figure 42**.[306] Reproduced from KUZINA ET AL. with permission. Copyright 2023, Wiley-VCH.

The microscopy images were further used by DR. YA-YUN TSAI to simulate material's elasticity response (as a part of a cooperation with the group of PROF. SHU-WEI CHANG). DR. YA-YUN TSAI gladly provided the images and the description of the simulation results for the manuscript that are presented further.

Microscopy images were analyzed to simulate elasticity using a variety of models, notably the lattice spring model (LSM), alongside the coarse-grained, spring network, and bead-spring models. LSMs, as depicted in **Figure 44** A, conceptualize a solid as a network of beads connected by harmonic springs, with each bead symbolizing a minor segment of the material interacting harmonically with others. This method has been widely employed in research on the mechanics of bio-inspired or 3D-printed materials due to its simplicity and efficacy.[331,333–335] Microscopy images of the pillar's top surface were randomly and automatically cropped (**Error! Reference source not found.** B) and subsequently converted into discrete particle models using the Img2Particle image-to-particle conversion tool (**Figure 44** C).[336] The outcomes from the lattice spring model conversions are presented in Figure 3D for samples M1, M4, and M7, illustrating the application of LSMs in evaluating the material's elastic properties.
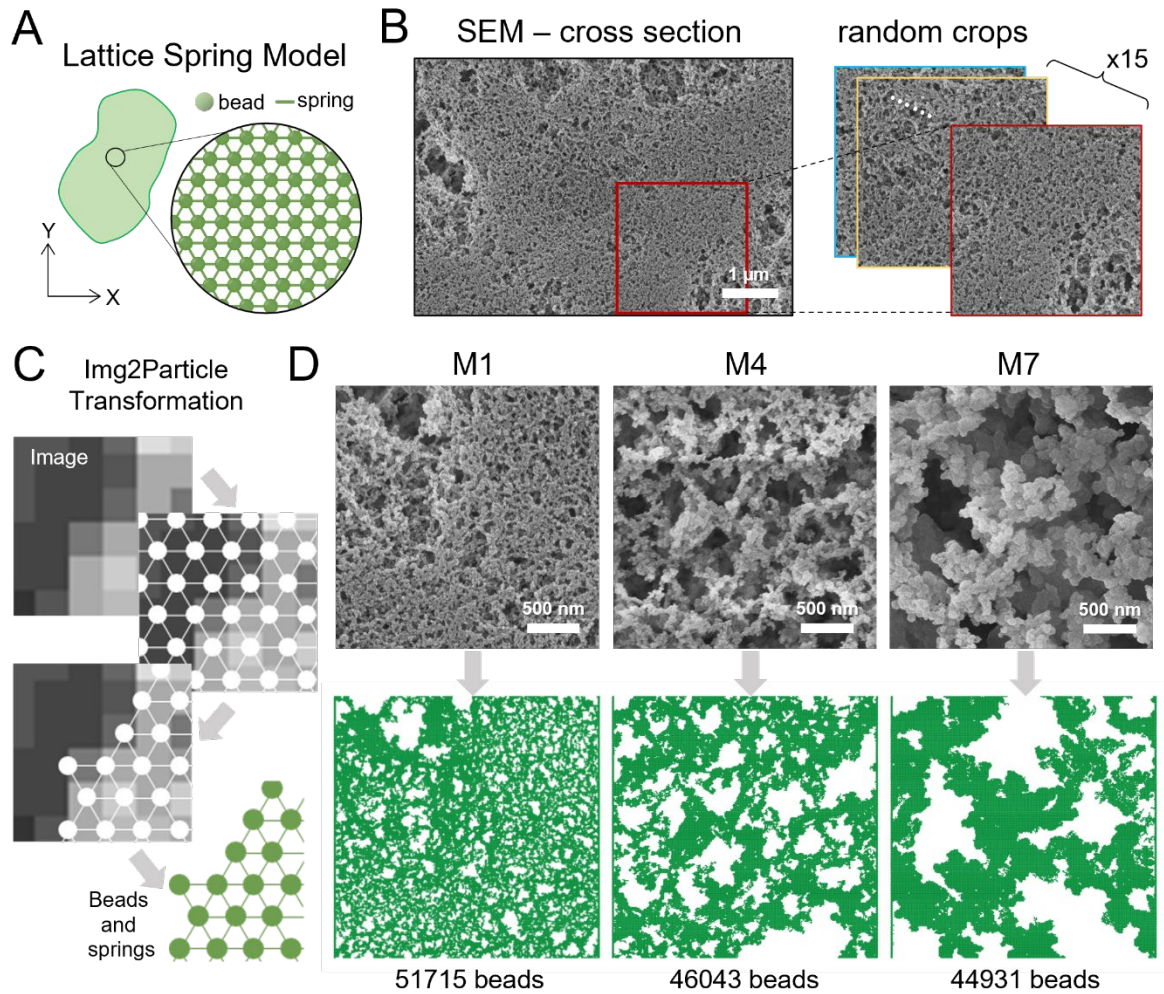
Figure 44. A procedure of cutting and converting SEM images for the elasticity simulations. (A) Illustration of the two-dimensional triangular LSM (B) An SEM image of the top surface of the pillar is cropped at a random location 15 times. (C) Illustration of the image-to-particle conversion tool, Img2Particle.[336] (D) Three examples of the converted bead models.[306] Reproduced from KUZINA ET AL. with permission. Copyright 2023, Wiley-VCH.

Based on the converted bead-spring networks, 525 simulation samples have resulted. Young's modulus values were derived from the samples by analyzing the stress-strain curves from 0.01% to 0.1% strain, following the application of a uniaxial tensile load horizontally to the bead-spring model. The example of detailed stress-strain curves for samples M1-M3 are given in **Figure 45**). Observations indicated that some clusters within the cropped images were weakly interconnected, leading to significantly lower Young's moduli. Models yielding a Young's modulus below 50 MPa were deemed invalid and excluded, resulting in 482 valid data points.
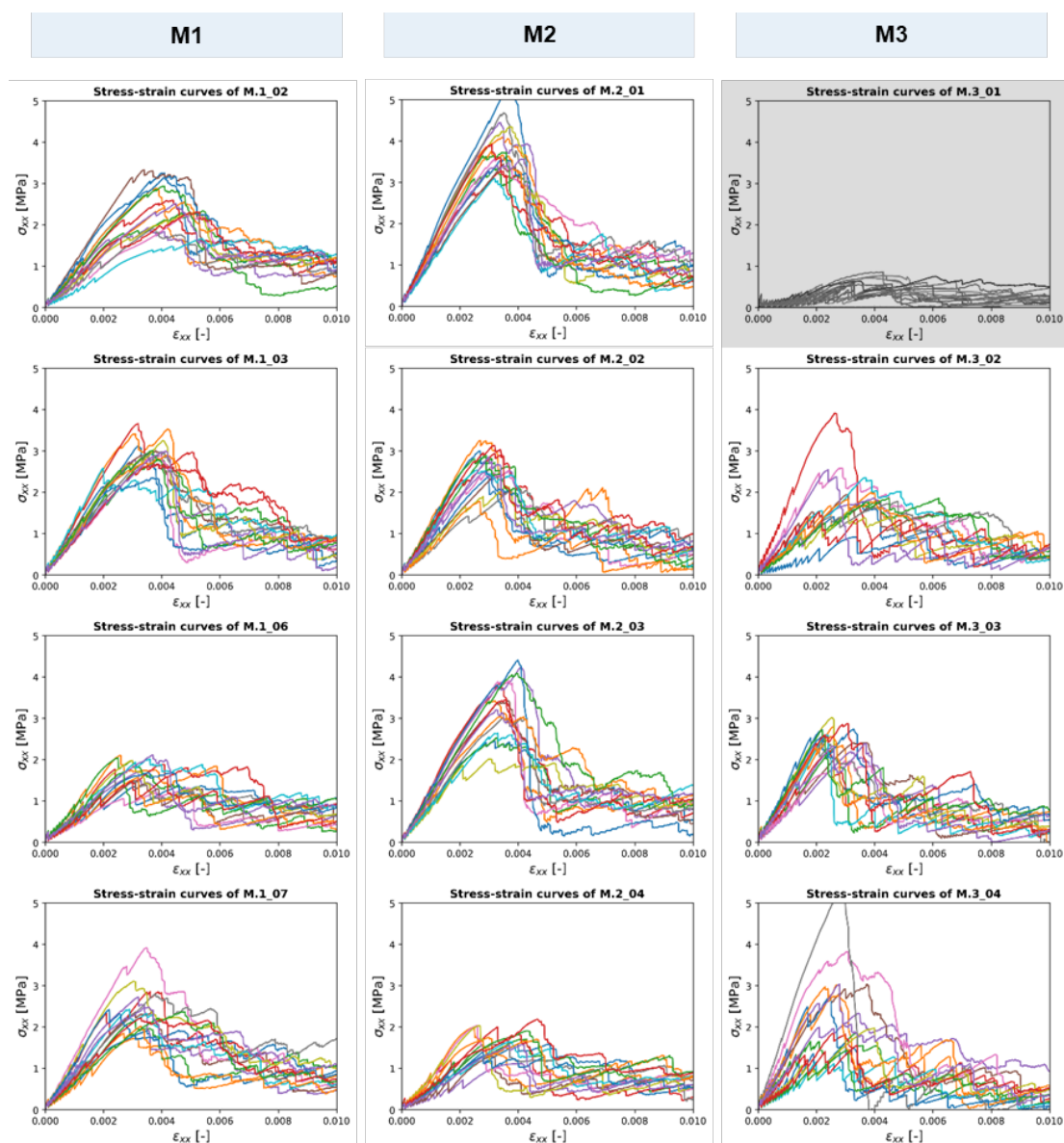
Figure 45. The stress-strain curves of simulated uniaxial tensile tests on M1 to M3. M.3_01 excluded due to falling out of the distribution. Other simulated curves can be found in the supplementary material to the publication of KUZINA ET AL.[306] Reproduced from KUZINA ET AL. with permission. Copyright 2023, Wiley-VCH.

A comparison of the average Young's modulus for samples M1 through M9 is depicted in **Figure 46** A and **Figure 46** B. The simulations revealed a trend of decreasing Young's modulus with an increase in the 1-decanol fraction within the co-porogen mixture, as shown in **Figure 46** C, which illustrates an inverse relationship between Young's modulus and porosity. Conversely, a direct relationship would then exist between Young's modulus and volume density. Beyond porosity (or calculated "volume density" =1 – "porosity"), the topology of the porous structures was also found to significantly influence stiffness. The stress distribution in samples M1, M4, and M7, showcasing the load transfer through the struts, is illustrated in **Figure 46** D and indicates that M1 exhibited a higher number of load transfer pathways.
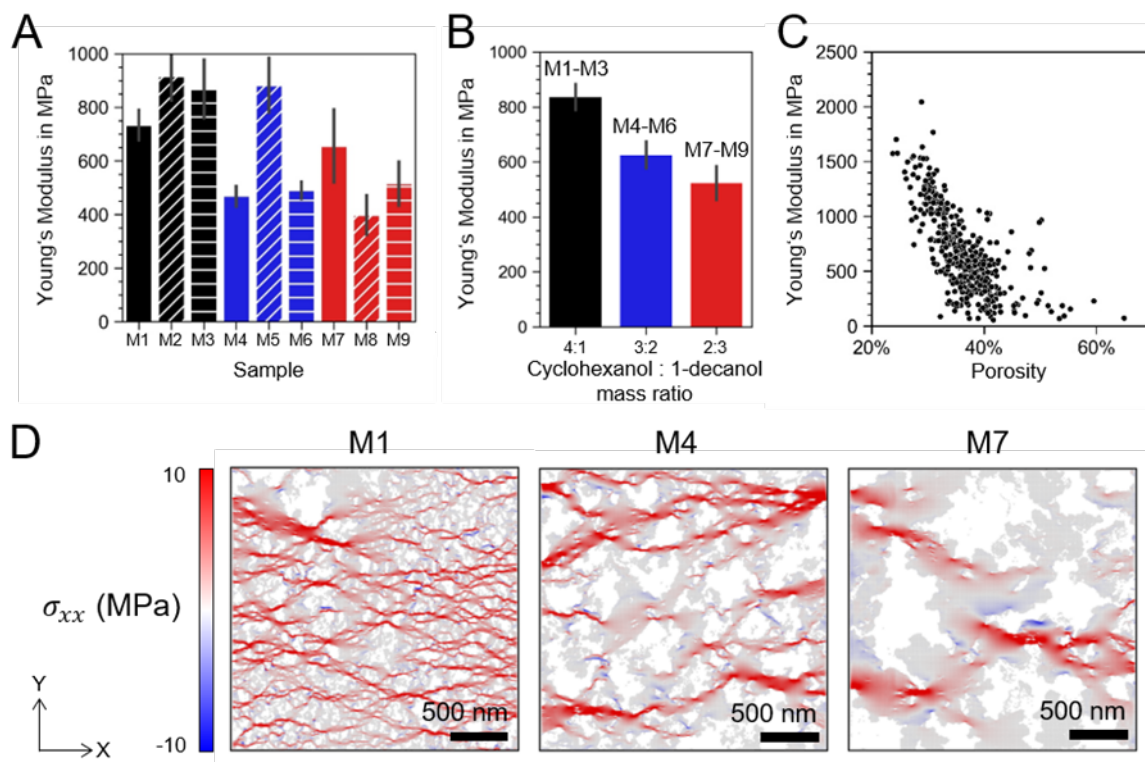
Figure 46. Comparison of simulated mechanical and topological properties. (A) A graph displaying Young's modulus for models M1 to M9, marked with error bars indicating a 95% confidence interval. The color coding (black for a cyclohexanol to 1-decanol ratio of 4:1, blue for 3:2, and red for 2:3) signifies the porogen ratios. Bar textures indicate printing layer thicknesses: solid for 50 µm, diagonal stripes for 100 µm, and horizontal stripes for 150 µm. (B) A trend showing a decrease in Young's modulus with an increase in the 1-decanol fraction in the porogen mixture is highlighted, comparing averaged values across the sample sets M1-M3, M4-M6, and M7-M9. (C) A scatter plot correlating porosity percentages derived from microscopy image analysis with Young's modulus, covering all 482 simulated data points. (D) Illustrations of stress distribution patterns under a strain of 0.075% in the X-direction for three sample cases, with a color scale from blue through white to red representing the range from compressive to tensile stresses in the X-direction.[306] Reproduced from KUZINA ET AL. with permission. Copyright 2023, Wiley-VCH.

In parallel with the computational analysis, the mechanical testing of the pillars was carried out. Mechanical tests were done by DR. CHANTAL M. KURPIERS within a collaboration with the group of PROF. RUTH SCHWAIGER. DR. KURPIERS gladly provided the description of the tests and analysis of the results for this study.

To study how the mechanical properties would be influenced by porosity and layer thickness, micro-compression tests were performed using a nanoindenter system. Each set of parameters was tested on three pillars, assessing stress and strain from the collected force and displacement data, as depicted in **Figure 47** A. The calculation of Young's modulus was based on the unloading curve's slope, providing insight into the materials' elastic properties, showcased in **Figure 47** B and **Figure 47** E. The chosen samples, M1, M4, and M7, were printed with a 50 µm layer thickness to take advantage of the higher z-printing resolution.

Stress-strain curves for these samples, with varying ratios of cyclohexanol to 1-decanol (**Figure 47** C-E), demonstrated material densification or cross-sectional changes upon unloading. Notably, Young's modulus exhibited a decrease from 554 MPa in M1 to 490 MPa in M4, before increasing to 722 MPa in M7, aligning with simulation predictions (**Figure 46** A). This pattern contradicts the expected trend of decreased stiffness with increased porosity, attributed to variations in pore distribution and cell wall thickness across samples. Specifically, M1 showed more variability due to its heterogeneous pore distribution, while M4 and M7, with larger and more uniformly distributed pores, suggested a relationship between increased 1-decanol content and particle agglomeration, leading to thicker cell walls and hence, higher stiffness in M7 as shown in **Figure 46** D. Furthermore, the mechanical properties, consistent with simulation results (**Figure 46** A), underscored the impact of 1-decanol fraction on stiffness, particularly notable in the transition from M4 to M7. It's important to recognize that the layer-by-layer printing approach used in this study could affect Young's modulus values due to overlapping layers and porosity gradients, suggesting the stiffness of the DLP 3D-printed material may vary from that of the base material without layering.
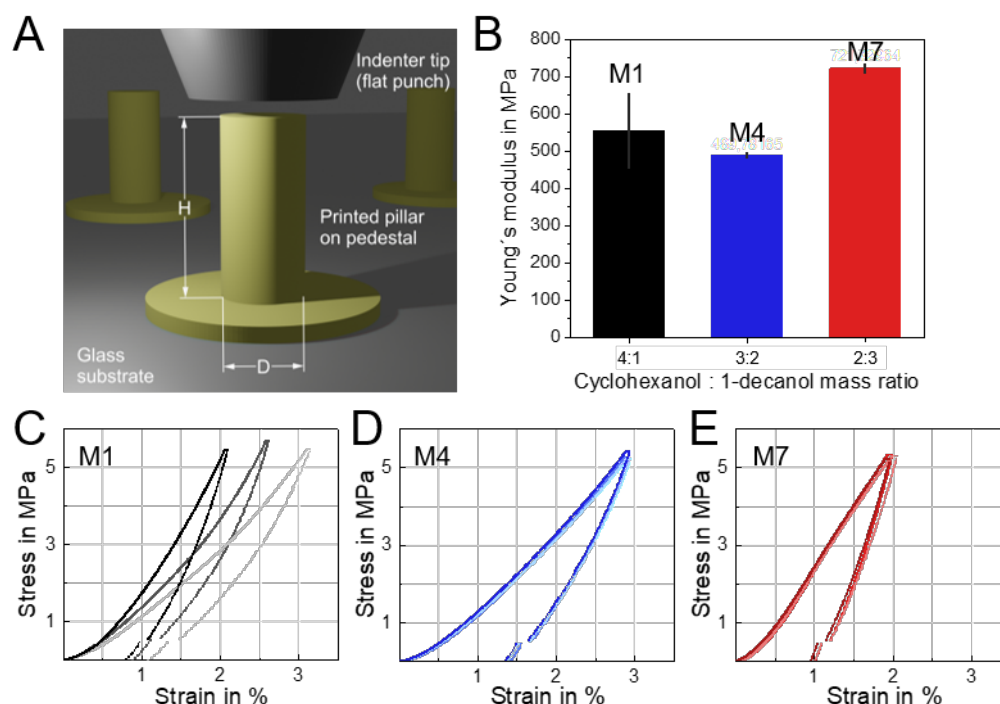
Figure 47. Compression tests for 3D-printed pillars. (A) A scheme of the experimental setup of pillar compression with a flat punch. Pillars with diameter D and height H were printed on a glass substrate and a thin pedestal. (B) Averaged Young´s modulus with standard deviation for samples M1, M4, and M7 (cyclohexanol : 1-decanol mass ratio equal to 4:1, 3:2, and 2:3, respectively) in MPa. (C)-(E) Stress-strain curves of pillar compression tests in the nanoindenter of M1, M4, and M7. For each condition, three pillars were tested. Error bars in (B) are standard deviations.[306] Reproduced from KUZINA ET AL. with permission. Copyright 2023, Wiley-VCH.

After testing the basic properties of porous polymers, the next step of decreasing material's weight followed. For that, 3D stretching-dominated tetrahedral architectures made of M1 and M4 materials were printed at the resolution limit of the technique resulting in millimeter-sized lattice structures. M1 and M4 compositions were chosen due to best printability and mechanical behavior based on previous printing and mechanical tests (M1 and M4). The main challenge of this step was that to be able to test the mechanical properties of the structures through the nano-indentation method, as it was done previously for the base material, the overall size of tetrahedra should correspond to the size of the tip. That placed limitations for the size of tetrahedra, since the largest available tip was ca. 5 mm. That would make tetrahedral features very small and make the structure prone to cracks and printing artefacts, since printing would occur at the edge of the DLP printing resolution (<100 μm). The problems with printing resolution, such as cloaked pores, cracks and uneven struts were present for multiple printing tests (**Figure 48**).
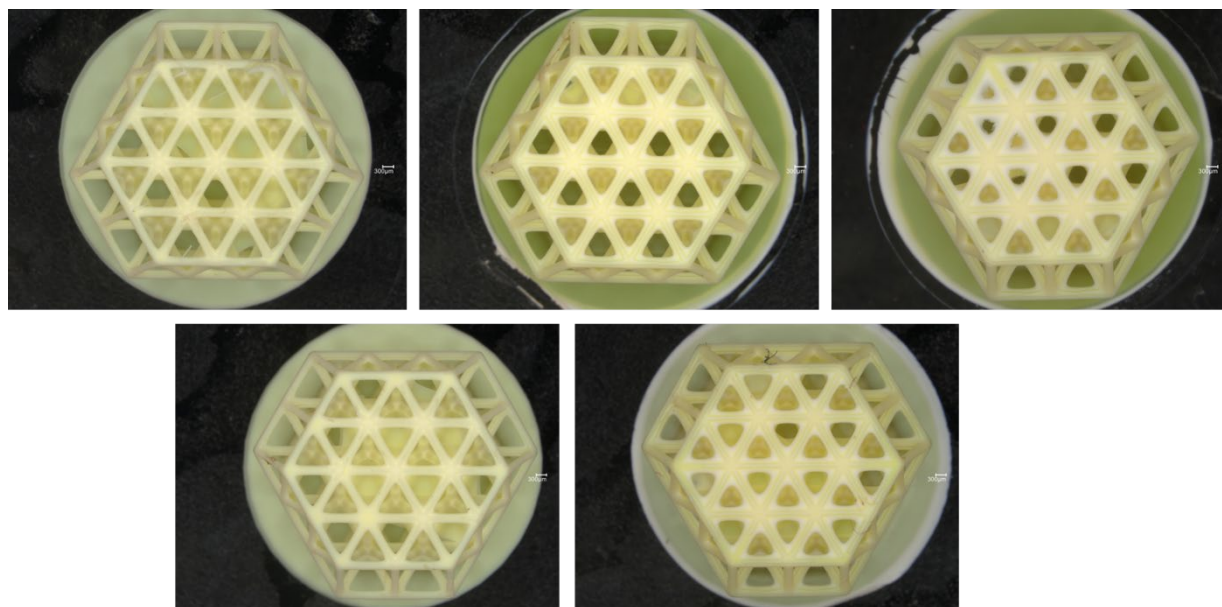
Figure 48. Issues with DLP printing of macro-porous (300-500 μm) tetrahedral structures.

However, through a multi-step process of varying the irradiation time and intensity per each layer, the optimal parameters were found that allowed to print tetrahedral structures without visible printing artefacts. To increase the stability of the structure at the contact with the glass substrate surface, a thin pedestal layer was added (in **Figure 49**, two tetrahedra – without and with a pedestal are compared). The final version of tetrahedra with the best printing quality (**Figure 49** B) was used for the mechanical tests.
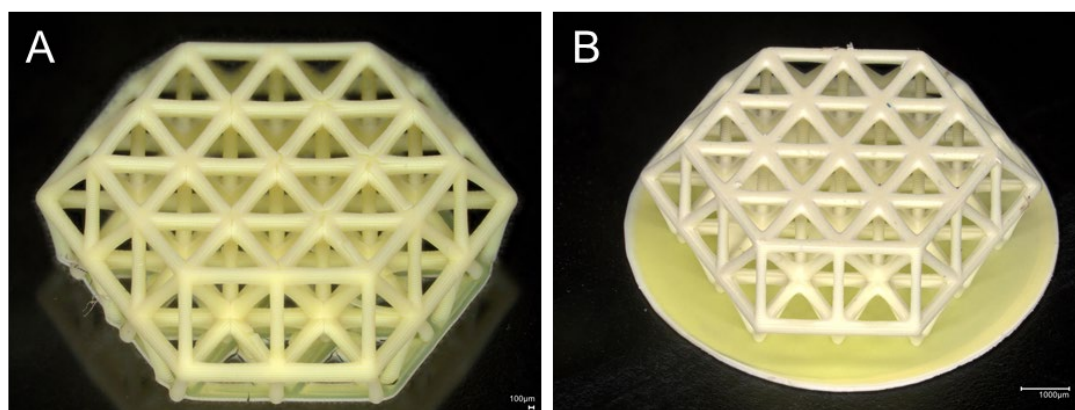
Figure 49. Comparison of the printing quality and first layers' integrity for the tetrahedral structures. (A) Tetrahedron without a pedestal, (B) tetrahedron with a pedestal. Both structures are printed on a pre-modified glass substrate.

For samples M1 and M4, the diameters measured at the top surface layer were 7.7 mm and 7.9 mm, respectively, while their heights were recorded at 3 mm for M1 and 3.6 mm for M4, as depicted in **Figure 50** A. The diameters of beam elements, ranging from 300 µm to 370 µm, displayed incremental steps of 50 µm along the z-axis of each structure, consistent with the layer-by-layer additive manufacturing process (demonstrated in **Figure 50** B).
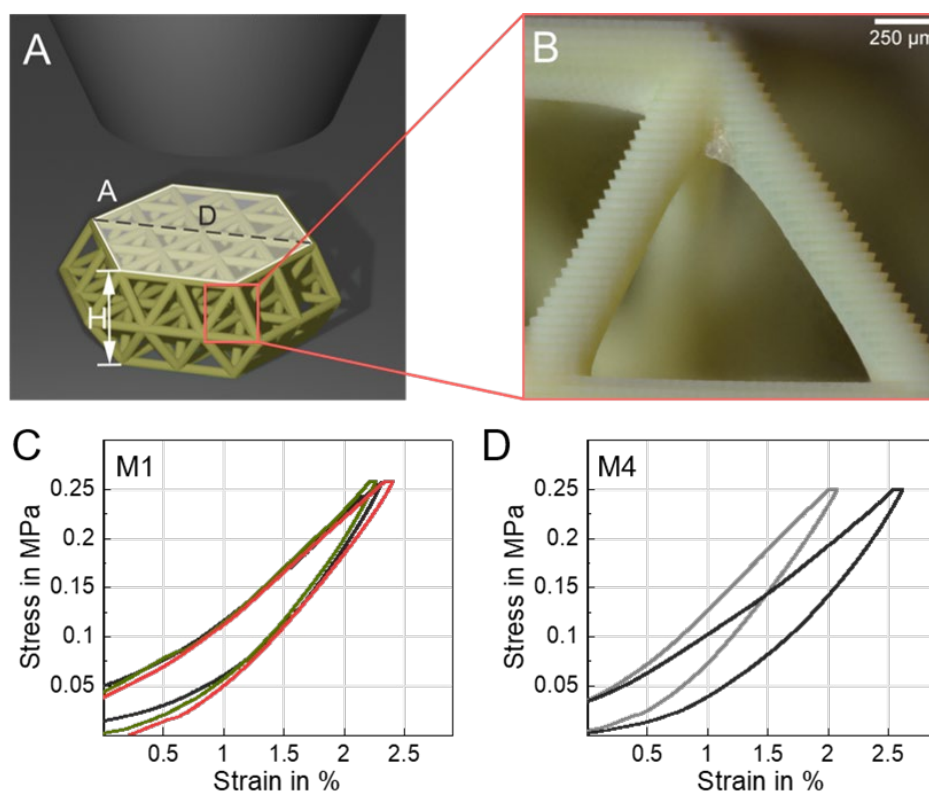
Figure 50. Compression tests of 3D-printed tetrahedral structures with intrinsic micro-porosity. (A) Schematic of compression test of a tetrahedral structure using a flat punch. Stress and strain were determined using the top area A and the height H, respectively, before the test. (B) The beams of the tetrahedral structure had diameters of 300 µm to 370 µm and step sizes of 50 µm as determined by light microscopy. (C) Representative stress-strain curves of tetrahedral structures under a compressive load of M1-based tetrahedron and (D) M4-based tetrahedron.[306] Reproduced from KUZINA ET AL. with permission. Copyright 2023, Wiley-VCH.

The compressive mechanical properties of the lattice structures, including the top surface area and height as presented in **Figure 50** A, were characterized. **Figure 50** C and **Figure 50** D display the stress-strain curves for the materials tested, indicating the stress calculations based on the top layer area as an approximation of the maximum stress levels. Adjustments were made to the x-axis of the curves to compensate for any misalignments between the indenter tip and the sample or surface roughness, identifiable by the initial flat sections of the curves. The elastic modulus was derived from the slope of the unloading segments, resulting in average elastic moduli of 17.6 ± 2.3 MPa for M1 (from ten samples) and 14.0 ± 0.5 MPa for M4 (from two samples). The consistency in deformation behavior suggests a high reproducibility, although variations due to printing limits and potential defects could affect mechanical outcomes. Integrating micro- and macro-porosity not only enhanced the material's porosity but also reduced its density. Specifically, M1 exhibited a density of 0.82 ± 0.02 g cm^{-3} with 35% porosity, and the combined density and porosity led to a specific stiffness for the tetrahedral structures of 79.5 MPa cm^3 g^{-1}. For M4, the density was 0.75 ± 0.04 g cm^{-3} with a porosity of 37.9%, resulting in a specific stiffness of 69.1 MPa cm^3 g^{-1}.
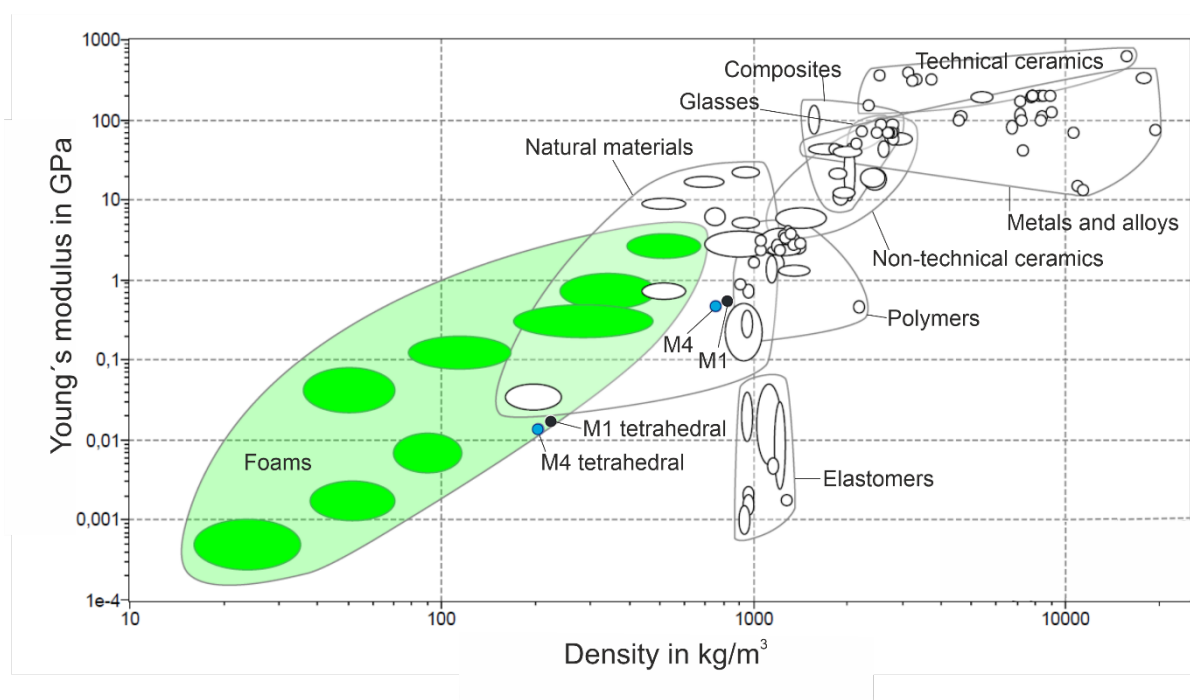
Figure 51. A materials property chart or Ashby plot demonstrating Young's modulus versus density. The chart is comparing the porous materials developed in this study against other standard material classes.[337] Black dots denote the M1 pillars and the M1 tetrahedral structures, while blue dots are used to denote the M4 pillars and M4 tetrahedral structures.[306] Plot provided by DR. CHANTAL M. KURPIERS. Reproduced from KUZINA ET AL. with permission. Copyright 2023, Wiley-VCH.

This hierarchical integration of porosity at different scales not only further reduces the density but also maintains structural stiffness comparable to foam materials, as shown in the Ashby plot

that illustrates the Young's moduli relative to the density, for the tetrahedral structures of M1 and M4, as well as for M1 and M4 pillars. Although these structures may not surpass foam materials in performance, their diverse three-dimensional configurations, enabled by 3D printing, offer unique advantages. This method of manipulating micro-porosity chemically and macro-porosity through design enhances the potential uses of porous materials, especially considering the increased surface area for applications such as cell grow[162] or catalysis.[338]

To sum up this study, stiff and lightweight polymer structures featuring porosity derived from polymerization-induced phase-separation process and precisely defined geometries were successfully produced. Based on microscopic observations of the samples' surfaces, material models for simulating mechanical properties were developed, and these models were further validated through micro-compression testing using the nanoindentation method. The tests revealed Young's moduli of 554 MPa, 490 MPa, and 722 MPa, varying with the ratio of cyclohexanol to 1-decanol, aligning closely with the simulations. This methodology highlights the significant advantages of 3D-printed inherited porous materials when combined with the computational analysis, which include: customizable porosity, the flexibility in geometric design, and the capability for mechanical behavior prediction.

Furthermore, the study explored both the constraints and future directions of the research. Mechanical assessments of macro-porous tetrahedral lattice structures identified a specific Young's modulus of 79.5 MPa cm^3 g^{-1}, positioning these materials comparably to foams and within the range of other recently developed 3D-printed porous polymers.[163,315] Nonetheless, the observed reduction in stiffness for macro-porous designs was attributed to fractures within the complex structural elements, challenges associated with the resolution limit of the DLP technique, and issues during the drying process. Additional DLP printing-related artifacts were identified, including the formation of recessed base layers, variability in porosity within and across layers, and the separation of printing layers at the structure's edges. Despite these challenges, the potential for further exploration into the structure-property relations of diverse 3D-printed lattice designs and the foundational porous material, as well as various combinations of liquid porogens, is very promising. Moreover, extending this methodology to alternative stereolithography techniques could mitigate the artifacts associated with the DLP printing process. Finally, the critical role that the composition of the liquid porogens plays in establishing and refining the material morphology in this study, underscores the powerful role of liquid phases in the design of modern functional material.

4. Conclusion and Outlook

In this work, the multifaceted role of liquids in the development of new materials was examined, demonstrating their essential contribution across three distinct yet interconnected domains. The investigation started with an exploration of liquids assembling on chemically patterned surfaces (Chapter 3.1: Liquid wells as analogues for solid vessels), proceeded through the fabrication of 3D-printed organic liquid-infused expanded polymer networks, organogels (Chapter 3.2: 3D-printed organogels with solvent-assisted tunable behavior), and finished in the creation of mechanically robust, inherently porous polymer structures through 3D printing, where the liquid phase acted as a primary determinant in material morphology through polymerization-induced phase separation (Chapter 3.3: Polymerization-induced phase separation to create 3D-printed inherently porous stiff materials).

The first part of the work was devoted to the creation of "liquid wells" on surfaces, achieved by confining various low-surface-tension hydrophobic liquids within water barriers formed by hydrophobic-hydrophilic core-shell patterning. These aqueous compartments were observed to serve as dynamic, self-healing barriers capable of chemical extraction through diffusion, presenting a novel approach to liquid containment on-a-chip. The patterning was realized through the thiol-ene photoclick reaction and a photomask enabling a large variety of the core-shell patterns available, which were tested for the solvent stability, as well as liquid-liquid wells' morphology differences. Key methods employed to investigate the unique on-surface liquid-liqid interface included raman mapping, confocal laser scanning microscopy (CLSM) and fluorescence microscopy, which allowed for the detailed investigation of the water-organic solvent interfaces and the behavior of liquid wells. These techniques were instrumental in visualizing the spatial distribution and interactions within the liquid wells. Additionally, water contact angle measurements were essential for assessing the wetting properties of heterogeneous surface, crucial for the effective liquid well formation. Interfacial surface tension measurements, critical for understanding the stability and formation of the liquid wells, were conducted using ring tensiometry. These measurements provided quantitative data on the forces governing the interfaces between the water walls and the contained LSTLs. The application of a phase-field model for multiphase wetting systems enabled the simulation of the liquid wells, offering a theoretical foundation to support experimental observations. This model helped predict the behavior of multidroplet wetting phenomena, elucidating the mechanisms behind the stability of the three-phase contact line (air-organic-water) and the effects of surface tension variations due to Gibbs adsorption. The created liquid-liquid wells have been applied for the

absorbtion of other liquids, substance exchange in the extraction experiments, as well as for the water-templated free-radical polymerization of the thin films. Various aspects of the liquid wells stability were investigated, such as the suitability tests for a large range organic liquids, cutting and injecting tests, complex patterns, triple-liquid-systems, agitation tests, maximul heights of the water barrier versus an organic liquid core. Through these methodological approaches, the study not only demonstrated the feasibility of creating fully liquid, functional, and self-healing compartments for the confinement and patterning of LSTLs but also highlighted the potential for rapid prototyping of polymer films via water-templated polymerization. The research opens new avenues for lab-on-a-chip applications, enabling studies of interfacial phenomena and offering a sustainable, fluorine-free strategy for advancing microfluidic systems. Despite facing challenges such as the height limitation of water barriers and compatibility with specific liquids, the study unveiled the potential of liquid-liquid wells for complex quasi-two-dimensional patterning and as innovative molds for polymer shaping, opening new avenues for microfluidic applications and further exploration of the liquid-liquid interface phenomenon.

In the second phase, the focus shifted to the potent role of organic liquids in modulating the properties of organogels as liquid-infused materials. through a 3D-printing-drying-swelling process. This section highlighted the adaptability of organogels soaked in various hydrophobic swelling solvents, which altered their bulk and surface properties, including adhesion and thermal behavior. Experimentally, a method was showcased for the creation of high-solvent-content organogels through DLP-based 3D printing and acrylate-based radical photopolymerization, uniquely designed to be independent of the choice of solvent. A universal, tunable approach for fabricating organogels with complex shapes was provided, significantly advancing the capability to manipulate organogel properties by the infusion of different non-polar solvents into the same polymer network. The swelling kinetics was measured and analyzed for the range of organic solvents. Through a post-printing swelling process, the characteristics of the polymer network were altered from highly adhesive to non-adhesive, employing hydrophobic solvents such as medium-chain alcohols, toluene, and oils, which was studied by the sliding sessile droplet tests via contat angle goniometry. Organogel thermo-mechanical properties could be modified to withstand a broad temperature range (-30°C to 25 and 25 to 100 °C) and to undergo reversible hardening-softening cycles determined by the solvent used, which was demonstrated by the temperature ramp rotational rheometry tests. Additionally, through optical profilometry and uv-vis spectroscopy the influence of swelling

on the removal of roughness and non.transparency of the 3D-printed organogels was demonstrated, as a way to eliminate the printing-related artifacts. Finally, mesh-shaped 3D-printed organogels showed four times more efficient extraction capacity and improved swelling kinetics, compared to the bulk gels. These findings open new perspective for the fabrication of organogels with tailored properties. Previously, exploring all combinations of networks and solvents would have required extensive protocols. With the demonstrated approach, the need for protocols has been significantly reduced, bringing the efficiency of exploring various combinations with the arbitraty choice of the solvent and material shape. Importantly, this approach allows for the inclusion of solvents that are incompatible with 3D printing or are highly hazardous, thus unlocking opportunities to create novel 3D organogel structures with unique properties. The concept of solvent-derived functionality is extendable to other 3D printing techniques, such as two-photon polymerization and stereolithography, offering a versatile method for producing organogels with customizable properties. This innovation holds particular relevance for applications beyond the scope of traditionally fabricated organogels.

The final part of the work showcased the significance of liquid porogens in the 3D printing of inherently porous polymers, showcasing how the composition of the liquid porogen critically influenced the materials' morphology and mechanical properties. The experimental part pf work was devised to explore the complex interplay between the structural configuration and the resultant properties of materials, by investigating 3D-printed porous polymers fabricated from radically polymerized acrylate-based monomer inks, carefully formulated by combining monomers, co-solvents, a photoinitiator and a dye to achieve inks capable of producing high-resolution 3D printed objects with superior mechanical stiffness. To avoid any mechanical damage related to the detachment of the 3D-printed objects, they were produced on the previously functionalized glass substrates to ensure adhesion, and dried on the substrate to remove any residual solvents. The material's microstructure was then characterized using scanning electron microscopy. Additionally, the particle agglomerate size analysis was employed, providing a deeper understanding of the material's granular structure. To complement the empirical investigations, computational modeling using the lattice spring model was incorporated in the study, predicting how the materials would behave under stress based on the microstructure shown by microscopy images. This approach allowed for a simulation of material elasticity, enhancing the understanding and predicting of the materials' mechanical properties. Finally, the mechanical properties of the printed structures were empirically determined through micro-compression testing, utilizing state-of-the-art equipment

to measure stress, strain, and Young's modulus. This testing provided valuable data on the relationship between the printing parameters, such as porosity and layer thickness, and the mechanical performance of the materials. Overall, the study adopted a comprehensive approach to investigating material properties, combining the tailoring of material properties through 3D printing technique, its micro- and macrostructure, followed by the detailed microstructural characterization, computational modeling, and mechanical testing. This comprehensive methodology aimed to shed light on how specific structural configurations of materials can be engineered to achieve desired properties, thereby advancing the field of 3D-printed porous lightweight materials. Through detailed mechanical characterization and computational modeling, the research demonstrated the ability to tailor porosity and stiffness in these polymer structures, aligning them with the properties of foam materials. Whereas the use of 3D printing technology enables an arbitrary shape and additional functionality added to the base material with the predictable mechanical behaviour, making them promising candidates for a wide range of applications, including cell growth, fabrication of implants, or catalysis.

The presented work stands as an exploration from multiple perspectives into the innovative utilization of liquids in the development of new materials, advancing several fields of material science simultaneously through experimental, theoretical, and computational methodologies. The significance of this research lies in its multidisciplinary approach to understanding and harnessing the properties of liquids for the creation of dynamic, functional, and sustainable material systems. The development of liquid wells for precise manipulation of LSTLs on surfaces introduces a novel method for creating fully liquid compartments. This breakthrough has a potential to be applied in microfluidic devices and presents a new paradigm for liquid patterning, offering solutions to challenges in handling of LSTLs in all-liquid devices. Similarly, the investigation into organogels through the infusion of organic liquids into polymers represents a significant stride toward the idea of tailoring organogel properties by its liquid component to achieve better functionality. This work not only advances our understanding of organogel behavior but also provides a versatile solvent-independent fabrication method that broadens the spectrum of possible applications for hundreds of liquids and polymer networks, contributing to the development of the organogel field towards real applications in microfluidics, soft robotics, catalytic and adsorbing materials, and more. Finally, the incorporation of liquid porogens in the 3D printing of porous polymers showcases a sophisticated approach to material design, enabling the creation of structures with specific predictable and tunable mechanical characteristics. Compatibility of such approach with a wide

range of polymerization systems underscores the innovative nature of using liquids in 3D-printing to shape and define material properties that can be applied across many materials that require tunable micro- and micromorphology for better applicability in catalysis, construction materials, microelectronics, or biomaterials. Collectively, these projects underscore the critical role of liquids in bridging traditional material classes with innovative solutions, setting several benchmarks for the utilization of liquid components in fabrication of new functional materials. This work attempts to broaden the understanding of liquid-material interactions for several types of materials through experimental and theoretical efforts, as well as explored distinctive features of liquid phase as a dynamic and functional component in multiple materials systems, which sets the stage for future innovations in all three represented areas: liquid systems on patterned surfaces, liquid-infused materials, and porous materials.

4 Experimental Part

4.1 Materials

4.1.1 Project "Liquid wells as analogues for solid vessels"

The functionalized microscopy glass slides were provided by Aquarray (Eggenstein-Leopoldshafen, Germany). Microscopy glass slides were from Schott Nexterion (Jena, Germany). Chemicals were purchased from Sigma Aldrich and used as received (Munich, Germany). Patterns were designed with the CAD software Rhinoceros 3D from Robert McNeel & Associates (Barcelona, Spain) and the respective photomask (chromium coated quartz glass) was fabricated by Rose Fotomasken (Bergisch-Gladbach, Germany). Modified nanoparticle-coated microscopic glass slides were purchased from Aquarray.

4.1.2 Project "3D-printed organogels with solvent-assisted tunable behavior"

Lauryl acrylate (LA) was purchased from abcr. polypropylene glycol dimethacrylate (PPGDMA), 1-iodooctane, 1-decanol, oil blue n, oil red o, sudan I, and mineral oil (M5904, contains 36 wt% naphthene and 64 wt% of other saturated paraffins)[339] were purchased from Sigma-Aldrich. Irgacure 379 (2-dimethylamino-2-(4-methyl-benzyl)-1-(4-morpholin-4-yl-phenyl)butan-1-one) was purchased from IGM resins. 1-Octanol, 1-nonanol, toluene, and hexadecane were purchased from Alfa Aesar. n-octane was purchased from Merck.

4.1.3 Project "3D-printed inherently porous structures with tetrahedral lattice architecture"

The following chemicals were used for the printing ink: monomers 2-hydroxyethyl methacrylate (HEMA, purchased from Sigma-Aldrich, Darmstadt, Germany), ethylene glycol dimethacrylates (EDMA, purchased from MERCK KGaA, Darmstadt, Germany), initiator phenylbis(2,4,6-trimethylbenzoyl)phosphine oxide (Irgacure 819,S u. K Hock GmbH, Regen, Germany), as well as two co-solvents 1-decanol and cyclohexanol (both purchased from Sigma-Aldrich, Darmstadt, Germany).

Microscopy cover glasses of 22 x 22 mm size and 170 ± 5 μm thickness were purchased from Paul Marienfeld GmbH & Co KG, Lauda-Königshofen, Germany. For the substrate functionalization, 3-(trimethoxysilyl)propyl methacrylate (purchased from Alfa Aesar) was used.

4.2 Methods

4.2.1 Project "Liquid wells as analogues for solid vessels"

Photopatterning

Modified microscopic glass slides from Aquarray were photopatterned by two consecutive thiol-ene reactions. In a first step, 200 µL of a solution of 1-dodecanethiol (10 vol%) in isopropanol was pipetted onto a modified glass slide. Then, a photomask was placed on top and the surface was irradiated with UV light for 2 min (16.0−17.0 mW cm^{-2}). For the second modification, 200 µL of a solution of 2-mercaptoethanol (10 vol%) a 1:1 solvent mixture of ethanol and water was pipetted onto the glass surface, which was then covered by a quartz glass plate. The surface was again irradiated with UV light for 2 min (16.0−17.0 mW cm^{-2}). Slides were rinsed thoroughly with isopropanol and dried after each modification step. An UVAcube 2000 from Dr. Hönle AG (Gräfelfing, Germany) was used for irradiation. The parts of the surface to become hydrophilic were modified with 2-mercaptoethanol while the parts of the surface to become oleophilic were modified with 1-dodecanethiol.

Solvent confinement test

First the circle-shaped hydrophilic pattern was filled with 60 µL of water, which was dyed in blue. Then 20 µL of organic solvent were added in the middle of the pattern. To improve the visibility of the two phases, water was dyed with 10 w% of food blue ink from Dr. Oetker (Bielefeld, Germany) and the organic solvents were dyed with 10 w% of Oil Red O from Sigma Aldrich (Munich, Germany) to improve visibility of the phases.

Water-templated polymerization

A polymer precursor solution was prepared by dissolving lauryl acrylate (LA) in 1-nonanol in a mass ratio of 4:1. As a crosslinker, poly (propylene glycol) dimethacrylate (1 mol% relative to lauryl acrylate), the photoinitiator Irgacure 379 (4 wt% relative to lauryl acrylate), and Nile Red (0.036 wt% relative to the monomer) were added. The hydrophilic area of the pattern was filled with DI water. Then, the reaction mixture was poured into the hydrophobic surface area. The surface was then irradiated in the UV curing chamber UVAcube 2000 from Dr. Hönle AG (Gräfelfing, Germany) at a light intensity of 17-18 mW cm^{-2} for 3 minutes. The substrate was gently rinsed with 2-propanol to remove the water walls.

Confocal laser scanning microscopy (CLSM)

Water-organic solvent interface on a pattern was investigated using confocal microscopy imaging (Leica Confocal Microscope SPE.). The fluorescence was observed for water stained with Rhodamine B (excitation/emission ~553/627 nm, 0.33 mg/ml) and 1-nonanol or *n*-hexadecane stained with Nile Red (excitation/emission ~552/636 nm, 0.33 mg ml^{-1}). LiCl (100 mg ml^{-1}) was added to the aqueous phase to prevent evaporation.

Fluorescence Microscopy

Fluorescence light microscopy images of liquid wells were recorded using a Keyence BZ-9000 fluorescence microscope from Keyence Corporation (Osaka, Japan).

Interfacial Surface Tension Measurement

The interfacial tension γ_{ow} (1-nonanol-water) was determined via ring tensiometry using a K11 Tensiometer from Krüss (Hamburg, Germany). The correction factor was chosen as described by Huh & Mason.[340] The measurement can be described in brief: A ring is deposited at the interface of two liquids and is then lifted. When the ring is not wetted by the interface anymore, the force exerted onto the ring decreases. Since this force is a function of the interfacial tension, the interfacial tension can be determined.

Raman microscopy

Raman 2D microscopy was performed on a Bruker Senterra instrument from Bruker Optic (Ettlingen, Germany). Excitation was performed with a laser beam at 532 nm at 2 mW output power. Spectra were collected from 70 – 4450 cm^{-1}. The Raman map consisted of 108 individual spectra over a surface area of ca. 3 • 5 mm². A chemical map was obtained by integration of the characteristic OH-stretching vibration from 3700 to 3140 cm^{-1} and the CH-stretching vibration from 3020 to 2780 cm^{-1}. To minimize evaporation of the aqueous compartment, LiCl was added (0.5 g mL^{-1}). To 60 µL of this solution 1 mg of phosphoric acid was added to serve as an internal reference.

Phase-field model for multiphase wetting systems

To model multidroplet wetting phenomena with N phases, $N \in \mathbb{N}$, we introduce a vector-valued order parameter $\boldsymbol{\varphi}(\boldsymbol{x},t) = (\varphi_1(\boldsymbol{x},t), ..., \varphi_N(\boldsymbol{x},t))^{\mathrm{T}}$, where $\varphi_i(\boldsymbol{x},t)$, $i \in \{1, ..., N\}$, describes the state of the phase i at time t and position $\boldsymbol{x}$. The order parameter $\varphi_i(\boldsymbol{x},t)$ varies continuously between two states, $\varphi_i(\boldsymbol{x},t) = 0$ (in gas) and $\varphi_i(\boldsymbol{x},t)=1$ (in liquid). The phase-field model is a kind of diffuse

interface model and based on the Ginzburg–Landau energy density functional, which is formulated as:

$$F(\boldsymbol{\varphi}) = \int_V \left(\varepsilon a(\boldsymbol{\varphi}, \nabla\boldsymbol{\varphi}) + \frac{1}{\varepsilon} w(\boldsymbol{\varphi}) + g(\boldsymbol{\varphi}) \right) dV + \int_S f_w(\boldsymbol{\varphi}) dS,$$

where V is the spatial domain, S indicates the solid-fluid boundary, and ε is related to the thickness of the diffuse interface. The first term $a(\boldsymbol{\varphi}, \nabla\boldsymbol{\varphi})$ is the gradient energy density and reads $a(\boldsymbol{\varphi}, \nabla\boldsymbol{\varphi}) = \sum_{i<j} \gamma_{ij} (\varphi_i \nabla\varphi_j - \varphi_j \nabla\varphi_i)^2$, with γ_{ij} denoting the surface/interfacial energy density of the ij phase boundary. The second term $w(\boldsymbol{\varphi})$ denotes a multiobstacle potential of the form:

$$w(\boldsymbol{\varphi}) = \frac{16}{\pi^2} \sum_{i<j} \gamma_{ij} \varphi_i \varphi_j + \sum_{i<j<k} \gamma_{ijk} \varphi_i \varphi_j \varphi_k$$

Here, the higher order term $\sum_{i<j<k} \gamma_{ijk} \varphi_i \varphi_j \varphi_k$ is used to suppress artificial third phase contributions along binary phase boundaries. The third term $g(\boldsymbol{\varphi})$ is formulated to ensure the volume conservation of respective phases. The last term $f_w(\boldsymbol{\varphi})$ depicts the wall energy density, which constrains the Young's wetting angles at the three-phase contact line on the substrate.

The evolution of the phase order parameter $\varphi_i(\boldsymbol{x}, t)$ is such as to minimize the free energy functional:

$$\tau\varepsilon\partial_t\varphi_i = \varepsilon \left(\nabla \cdot a_{,\nabla\varphi_i}(\boldsymbol{\varphi}, \nabla\boldsymbol{\varphi}) - a_{,\varphi_i}(\boldsymbol{\varphi}, \nabla\boldsymbol{\varphi}) \right) - \frac{1}{\varepsilon} w_{,\varphi_i}(\boldsymbol{\varphi}) - g_{,\varphi_i}(\boldsymbol{\varphi}) - \lambda_1$$

in V with the natural boundary condition

$$-\varepsilon a_{,\nabla\varphi_i}(\boldsymbol{\varphi}, \nabla\boldsymbol{\varphi}) \cdot \boldsymbol{n} - f_{w,\varphi_i}(\boldsymbol{\varphi}) - \lambda_2 = 0$$

on S. Here, $\boldsymbol{n}$ is the normal vector of the substrate and τ is a pseudo time variable. This pseudo time relaxation is used to effectively find the equilibrium state following the gradient descent path. The notations $a_{,\nabla\varphi_i}$, $a_{,\varphi_i}$, $w_{,\varphi_i}$, $g_{,\varphi_i}$, and f_{w,φ_i} describe the partial derivatives $\partial / \partial_{\nabla\varphi_i}$ and $\partial / \partial_{\varphi_i}$ of the functions $a(\boldsymbol{\varphi}, \nabla\boldsymbol{\varphi})$, $w(\boldsymbol{\varphi})$, $g(\boldsymbol{\varphi})$, and $f_w(\boldsymbol{\varphi})$, respectively. λ_1 and λ_2 are Lagrange multipliers to ensure the constraint $\sum_{i=1}^N \varphi_i(\boldsymbol{x}, t) = 1$ in the domain V and on the substrate S, respectively. The Lagrange multipliers λ_1 and λ_2 are found to read:

$$\lambda_1 = \frac{1}{N} \sum_{i=1}^N (\varepsilon \left(\nabla \cdot a_{,\nabla\varphi_i}(\boldsymbol{\varphi}, \nabla\boldsymbol{\varphi}) - a_{,\varphi_i}(\boldsymbol{\varphi}, \nabla\boldsymbol{\varphi}) \right) - \frac{1}{\varepsilon} w_{,\varphi_i}(\boldsymbol{\varphi}) - g_{,\varphi_i}(\boldsymbol{\varphi})),$$

$$\lambda_2 = \frac{1}{N} \sum_{i=1}^N (-\varepsilon a_{,\nabla\varphi_i}(\boldsymbol{\varphi}, \nabla\boldsymbol{\varphi}) \cdot \boldsymbol{n} - f_{w,\varphi_i}(\boldsymbol{\varphi})).$$

Water contact angle measurements

Measurements were performed with a DSA 25 contact angle goniometer from Krüss (Hamburg, Germany) using the sessile drop technique. Apparent contact angles were determined by depositing 5 µL droplets of 1-nonanol, *n*-hexadecane, or water onto the surface. The droplet shape was fitted with a Young-Laplace fit. Apparent contact angles were determined on surfaces coated completely with either the hydrophobic, the hydrophilic, or the omniphobic surface modification.

4.2.2 Project "3D-printed organogels with solvent-assisted tunable behavior"

Ink preparation

PPGDMA was purified with an Al_2O_3-basic column to remove the inhibitor. Other solvents and reagents were used without further purification. Ink compositions contained 100:0, 80:20, 70:30, or 50:50 weight ratio of LA to mineral oil. After that, in relation to the quantity of monomer, 0.5/0.75/1 mol% of PPGDMA and 4 wt% of initiator irgacure 379 (2-dimethylamino-2-(4-methyl-benzyl)-1-(4-morpholin-4-yl-phenyl)butan-1-one) were added. To achieve the colored printed object shown in **Figure 28** A, 0.05 wt% of sudan I was additionally added to the inks. All components were mixed and sonicated for 30 min at 35 °C to completely dissolve the photoinitiator. The ink was stored in a dark flask at 5 °C and equilibrated to room temperature before printing.

Detailed compositions of the inks are provided in the Discussion and Results, Chapter 3.2 (**Table 4**)

Printing protocol

All objects were printed using a commercial DLP-based 3D printer Miicraft 110 Prime (Taiwan) with the following parameters: layer thickness 50 µm, curing time per layer 10 s, and power ratio 0.5 (a Miicraft software printing parameter corresponding to 50% of the maximum brightness of light engine).

Swelling

For swelling, printed organogels were sonicated in 30-50 ml of isopropanol for 48 h to remove the sacrificial printing solvent, photo initiator, and unreacted monomer/crosslinker. After that, the objects were dried on air for 8-12 h and were placed in excess of the desired solvent. To measure swelling, the objects were weighed before and after swelling at 24 h intervals, after

which the swelling ratios were calculated from the mass of the dried (W_{dr}) and swollen gel (W_{sw}) according to the following formula:

Swelling [%] = (W_{sw} − W_{dr}) · W_{dr}^{-1} ·100%

Wet and solid adhesion

For measuring the liquid and solid adhesion of organogels, sliding angles at a KRÜSS DSA25S Drop Shape Analyzer (Germany) of a 15 µl water drop and 0.91 g neodymium cube, respectively, were recorded. To determine the sliding angle, a 3d-printed organogel with a smooth flat top surface was fixed on a platform. After placing a drop or a cube on the gel, the sample-holding platform started tilting at 1° per second from 0 to 90° with the device camera recording the movement of the sliding object. The angle was determined as the moment the object left its initial position, i.e., starts sliding. For the swollen organogels, prior to the measurement, the excess of swelling liquid was removed by a non-fiber tissue. Each sliding experiment was repeated 5 times. Between the measurements, organogels were re-immersed in their respective solvents to replenish lubrication layers.

Optical digital microscopy

Optical digital microscopy images were captured with a VHX-7000 Microscope (Keyence, Japan), 20x lens.

Optical profilometry

Profiles on the Figures 4B, E were characterized with the optical microscope equipped with the laser VK-X3000 (Keyence, Germany), across the surface of the non-swollen and swollen in mineral oil gel. Axis Y of the profile represents depth, axis X represents the length of sample along which the profile was measured.

Rheology

The tests were conducted on the strain-controlled rheometer ARES G2 (TA Instruments, Eschborn, Germany). For the test, 3 samples were chosen: the non-swollen gel, the gel swollen in n-hexadecane (72 h), and the gel swollen in butyl disulfide (72 h). The test geometry was a 13.0 mm parallel plate, and a constant axial force of 1 N (ca. 11600 Pa) at an angular frequency ω = 1 rad/s was applied, while the sample was covered with a solvent trap to prevent solvent evaporation. The fixed value of strain of γ_o = 0.5 % was chosen to be in the viscoelastic regime. The low-temperature ramp was carried out over a range of 25 °C to –20 °C for non-swollen and

swollen in hexadecane gels, and from 20 °C to –40 °C for organogel swollen in dibutyl sulfide. The high-temperature ramp was carried out over a range of 25 °C to 100 °C for non-swollen and swollen hexadecane gels. A mobile fume extractor was placed next to the rheometer during all tests to avoid inhalation of any leaking solvent.

Camera

All photos were made with a Canon digital single-lens reflex camera (model: EOS 80D) using a 100 mm macro lens (model: ef 100 mm 1:2.8l macro is usm). Brightness and contrast were adjusted for the images in Figure 2 and Figure 5 for better clarity.

4.2.3 Project "3D-printed inherently porous structures with tetrahedral lattice architecture

Ink preparation

Monomer, crosslinkers, photoinitiator, and solvents were mixed, stirred, and sonicated for 30 min into a homogeneous ink. To achieve the highest resolution simultaneously with high stiffness, both a high ratio of monomers to solvents and high content of the cross-linking component is required. Based on the results of our previous study, we used the ratio HEMA : EDMA equal to 3 : 2 and the relative content of monomers to solvents of 50 wt.%.[162]

The exact ink compositions are shown in the "Results and discussion" section, **Table 5. Ink compositions with the varied co-porogen ratio.[306]**

To avoid aging, all inks were stored in amber glass vials at 5°C and renewed regularly.

3D printing

A commercial DLP-based 3D printer Miicraft 110 Prime (Miicraft, Taiwan) was used to print cylindrical pillars and complex tetrahedral architectures. All models were created with the CAD software Inventor (Autodesk Inventor, Autodesk Inc., San Rafael, USA) and imported into the printer as an .stlfile. As changing the ink composition affects the conversion efficiency of the ink, the printing times for some of the samples were changed based on the printing quality. Cylindrical pillars with a diameter of 500 μm (matching the flat indenter tip) and a height-to-diameter ratio of 3:1 were printed with the following printing settings:

For Ink 1 and Ink 2, power ratio and printing time of 50% and 100 s, respectively, were used.

For Ink 3, the power ratio was 50% and the printing time 150 s. The tetrahedral structures (height – 4 mm, top diameter – 8.7 mm) were printed using the following printing settings: a

layer thickness of 50 μm, a power ratio of 50%, and a curing time of 70 s for Ink 1 and 100 s for Ink 2.

Each printing time was adjusted experimentally based on the best printing quality.

For easier handling, all objects were printed on previously functionalized microscopy glass substrates. The samples, i.e., printed structures on the glass substrates, were put in acetone and dried vertically in the critical point dryer.

Substrate functionalization

Microscopy cover glasses were cleaned by isopropanol and ozone cleaner for 10 min. Then, the substrates were submerged overnight in a solution of 25 mL of absolute ethanol mixed with 1 mL of 3-(trimethoxysilyl)propyl methacrylate (purchased from Alfa Aesar). Finally, the slides were rinsed with ethanol and blow-dried by an air gun.

Samples drying

After detaching from the printing platform, the samples on the glass substrates were soaked in acetone for 24 h. To remove the residual solvent, the samples on the substrates were dried using an Automated Critical Point Dryer (Leica EM CPD030, Germany).

Microstructural characterization

The printed structures were characterized using a scanning electron microscope (Zeiss LEO 1530) at an operating voltage of 5 kV with an InLens detector. Prior to the SEM measurements, the samples were coated with a 10 nm thick carbon layer (EM ACE 600, Leica Microsystems GmbH, Germany).

Particle agglomerate size analysis

To estimate the average size of particle agglomerates of the porous polymer, the size distribution was estimated by the calculation of Feret's diameter. Boundaries of the agglomerates were manually delineated in the ImageJ software.[341] From the measured diameters, the average size and standard deviation were calculated. The size distribution was visualized by the normal distribution curve.

Morphology and elasticity modeling by the Lattice Spring Model

Elasticity modeling was performed by the lattice spring model (LSM), which is a coarse-grained particle-based model, adopted from the previous works.[333,335] For simulations, a 2D lattice

spring model with hexagonal packing particles and a triangular spring network was used, in which each particle binds with its first nearest neighbors through harmonic springs. All the simulations were performed by the open-source software LAMMPS (https://www.lammps.org).[342] The 2D simulation models were constructed from 35 SEM images (three for the sample M6 and four for others). First, each SEM image was reproduced 15 times by random crop. The cropped images were transformed into discrete particle models by img2particle software.[333,336] Two edges at the left and right were added to the models to grip the samples during the uniaxial tensile tests. Finally, a uniaxial tensile load was applied horizontally based on the computational framework described in LIBONATI ET AL.[26][331]

Micro-compression testing

To determine the mechanical properties depending on porosity and layer thickness in the printing process, we carried out compression tests using an Agilent Technologies nanoindenter system (G200 XP, Agilent Technologies Inc., Santa Clara, USA). For each parameter set, three pillars were tested by compressing them at a displacement rate of 100 nm/s with a diamond flat punch of 600 μm diameter until the maximum force of the indenter (approximately 500 mN) was reached. Then, the load was removed at the same rate. With the mean value of the diameter and height of the pillars, which were measured using a digital microscope (VHX-7000, Keyence Corporation, Osaka, Japan), stress and strain were calculated. Young´s modulus was determined from the slope of the unloading curve.

The tetrahedral lattices were tested with a CSM indenter (Anton Paar, Switzerland) equipped with a custom-made Al flat punch with a diameter of 5 mm. The compression tests were conducted with a loading rate of 0.5 N/min until reaching the maximum force of 6 N. Stress and strain were estimated based on the area of the top layer of the tetrahedral structure and the height before loading (**Figure 50**).

Graphics were created using CorelDRAW, Blender and BioRender.com.

5 List of Abbreviations

CLSM	confocal laser scanning microscopy
DI	deionised
DLP	digital light processing
EDMA	ethylene glycol dimethacrylate
HEMA	hydroxyethyl methacrylate
LA	lauryl acrylate
LIS	lubricant-infused surfaces
LLPS	liquid-liquid phase separation
LSM	lattice spring model
LSTL	low-surface-tension liquid
MP	melting point
o(PGDMA)	oligo(propylene glycol) dimethacrylate
PPGDMA	poly(propylene glycol) dimethacrylate
SEM	scanning electron microscopy
UV	ultraviolet
WTP	water-templated polymerization

6 List of Figures

7 List of Tables

8 Literature

[1] B. L. Karger, L. R. Snyder, C. Eon, *Journal of Chromatography A* **1976**, *125*, 71.

[2] D. Rajendran, R. Ramalingame, A. Adiraju, H. Nouri, O. Kanoun, *J. Compos. Sci.* **2022**, *6*, 26.

[3] G. Sánchez-Balderas, J. D. H. Velázquez, E. Pérez, *Langmuir* **2022**, *38*, 12804.

[4] H. Gudla, C. Zhang, D. Brandell, *The Journal of Physical Chemistry B* **2020**, *124*, 8124.

[5] S. Savić, M. Savić, S. Tamburić, G. Vuleta, S. Vesić, C. C. Müller-Goymann, *European Journal of Pharmaceutical Sciences* **2007**, *30*, 441.

[6] W. Zhang, X. Xu, X. Zhao, G. Zhou, *Food Hydrocolloids* **2022**, *128*, 107563.

[7] S. Raub, G. Jansen, *Theoretical Chemistry Accounts: Theory, Computation, and Modeling (Theoretica Chimica Acta)* **2001**, *106*, 223.

[8] M. Piejko, B. Patrahau, K. Joseph, C. Muller, E. Devaux, T. W. Ebbesen, J. Moran, *Journal of the American Chemical Society* **2023**, *145*, 13215.

[9] A. Dutta, R. K. Behera, N. Pradhan, *ACS Energy Lett.* **2019**, *4*, 926.

[10] K. Scheurrell, I. C. B Martins, C. Murray, F. Emmerling, *Phys. Chem. Chem. Phys.* **2023**, *25*, 23637.

[11] K. Fumino, P. Stange, V. Fossog, R. Hempelmann, R. Ludwig, *Angewandte Chemie International Edition* **2013**, *52*, 12439.

[12] D. R. Joshi, N. Adhikari, *1* **2019**.

[13] G. Schmidt-Naake, I. Woecht, A. Schmalfuß, T. Glück, *Macromolecular Symposia* **2009**, *275–276*, 204.

[14] R. Kol, P. Nachtergaele, T. de Somer, D. R. D'hooge, D. S. Achilias, S. de Meester, *Ind. Eng. Chem. Res.* **2022**, *61*, 10999.

[15] Y. Marcus, *Chem. Soc. Rev.* **1993**, *22*, 409.

[16] K. Tamm, *Berichte der Bunsengesellschaft für physikalische Chemie* **1974**, *78*, 98.

[17] A. R. Katritzky, D. C. Fara, H. Yang, K. Tämm, T. Tamm, M. Karelson, *Chemical reviews* **2004**, *104*, 175.

[18] L. Hartshorn, J. V. L. Parry, L. Essen, *Proc. Phys. Soc. B* **1955**, *68*, 422.

[19] P. Havran, R. Cimbala, J. Kurimský, B. Dolník, I. Kolcunová, D. Medveď, J. Király, V. Kohan, Ľ. Šárpataky, *Energies* **2022**, *15*, 391.

[20] S. K. Subburaj, M. Rengaraj, R. Mariappan, *International Journal of Emerging Electric Power Systems* **2020**, *21*.

[21] D. C. Wadsworth, I. Mudawar, *Journal of Heat Transfer* **1990**, *112*, 891.

[22] X. Li, L. Lv, X. Wang, J. Li, *Thermal Science and Engineering Progress* **2021**, *25*, 100986.

[23] A. Puerto, A. Méndez, L. Arizmendi, A. García-Cabañes, M. Carrascosa, *Phys. Rev. Applied* **2020**, *14*.

[24] F. O. Romero-Soto, M. I. Polanco-Oliva, R. C. Gallo-Villanueva, S. O. Martinez-Chapa, V. H. Perez-Gonzalez, *Electrophoresis* **2021**, *42*, 605.

[25] Q. Ma, Y. Song, W. Sun, J. Cao, H. Yuan, X. Wang, Y. Sun, H. C. Shum, *Advanced Science* **2020**, *7*, 1903359.

[26] A. D. Buckingham, *Aust. J. Chem.* **1953**, *6*, 93.

[27] N. Yao, X. Chen, X. Shen, R. Zhang, Z.-H. Fu, X.-X. Ma, X.-Q. Zhang, B.-Q. Li, Q. Zhang, *Angew. Chem.* **2021**, *133*, 21643.

[28] M. A. Kuzina, D. D. Kartsev, A. V. Stratonovich, P. A. Levkin, *Adv. Funct. Mater.* **2023**.

[29] J. P. Baker, H. Le Hong, H. W. Blanch, J. M. Prausnitz, *Macromolecules* **1994**, *27*, 1446.

[30] B. S. Kaith, A. Singh, A. K. Sharma, D. Sud, *J Polym Environ* **2021**, *29*, 3827.

[31] M. F. Haase, K. J. Stebe, D. Lee, *Advanced Materials* **2015**, *27*, 7065.

[32] A. Bartolini, P. Tempesti, A. F. Ghobadi, D. Berti, J. Smets, Y. G. Aouad, P. Baglioni, *Journal of colloid and interface science* **2019**, *556*, 74.

[33] N. M. Correa, J. J. Silber, R. E. Riter, N. E. Levinger, *Chemical reviews* **2012**, *112*, 4569.

[34] G. R. Guillen, Y. Pan, M. Li, E. M. V. Hoek, *Ind. Eng. Chem. Res.* **2011**, *50*, 3798.

[35] M. Padaki, R. Surya Murali, M. S. Abdullah, N. Misdan, A. Moslehyani, M. A. Kassim, N. Hilal, A. F. Ismail, *Desalination* **2015**, *357*, 197.

[36] C. Kahrs, J. Schwellenbach, *Polymer* **2020**, *186*, 122071.

[37] T.-N. Gao, T. Wang, W. Wu, Y. Liu, Q. Huo, Z.-A. Qiao, S. Dai, *Advanced Materials* **2019**, *31*, e1806254.

[38] C. Mollart, A. Trewin, *Phys. Chem. Chem. Phys.* **2020**, *22*, 21642.

[39] S. H. Bauer, *J. Chem. Educ.* **1958**, *35*, 289.

[40] K. S. Pitzer, D. Z. Lippmann, R. F. Curl, C. M. Huggins, D. E. Petersen, *J. Am. Chem. Soc.* **1955**, *77*, 3433.

[41] K. M. Watson, *Industrial & Engineering Chemistry* **1943**, *35*, 398.

[42] J. C. Mcgowan, *Recl. Trav. Chim. Pays-Bas* **1965**, *84*, 99.

[43] D. M. Murphy, T. Koop, *Q. J. R. Meteorol. Soc.* **2005**, *131*, 1539.

[44] J. W. Goodrum, D. P. Geller, *Bioresource technology* **2002**, *84*, 75.

[45] J. C. Dearden, *Environmental toxicology and chemistry* **2003**, *22*, 1696.

[46] B. K. Mandal, A. K. Padhi, Z. Shi, S. Chakraborty, R. Filler, *Journal of Power Sources* **2006**, *162*, 690.

[47] A. Jänes, E. Lust, *Journal of Electroanalytical Chemistry* **2006**, *588*, 285.

[48] B. Nan, L. Chen, N. D. Rodrigo, O. Borodin, N. Piao, J. Xia, T. Pollard, S. Hou, J. Zhang, X. Ji, J. Xu, X. Zhang, L. Ma, X. He, S. Liu, H. Wan, E. Hu, W. Zhang, K. Xu, X.-Q. Yang, B. Lucht, C. Wang, *Angewandte Chemie International Edition* **2022**, *61*, e202205967.

[49] Y. Jian, S. Handschuh-Wang, J. Zhang, W. Lu, X. Zhou, T. Chen, *Mater. Horiz.* **2021**, *8*, 351.

[50] X. Su, H. Wang, Z. Tian, X. Duan, Z. Chai, Y. Feng, Y. Wang, Y. Fan, J. Huang, *ACS Applied Materials & Interfaces* **2020**, *12*, 29757.

[51] H. Gao, Z. Zhao, Y. Cai, J. Zhou, W. Hua, L. Chen, L. Wang, J. Zhang, D. Han, M. Liu, L. Jiang, *Nature communications* **2017**, *8*, 15911.

[52] K. Oliver, A. Seddon, R. S. Trask, *J Mater Sci* **2016**, *51*, 10663.

[53] B. Jin, J. Liu, Y. Shi, G. Chen, Q. Zhao, S. Yang, *Advanced Materials* **2022**, *34*, e2107855.

[54] C.-M. Chen, C.-L. Chiang, S. Yang, *Langmuir* **2015**, *31*, 9523.

[55] Z. Wang, M. Heck, W. Yang, M. Wilhelm, P. A. Levkin, *Adv. Funct. Mater.* **2023**.

[56] L. Zeng, X. Lin, P. Li, F.-Q. Liu, H. Guo, W.-H. Li, *Progress in Organic Coatings* **2021**, *159*, 106417.

[57] A. E. Balan, A. Al-Sharea, E. J. Lavasani, E. Tanasa, S. Voinea, B. Dobrica, I. Stamatin, *Materials (Basel, Switzerland)* **2023**, *16*.

[58] X. Wang, P. Jia, S. Sun, X. He, T. J. Lu, F. Xu, S. Feng, *ACS Omega* **2021**, *6*, 21646.

[59] N. Blagojevic, M. Müller, *ACS Applied Materials & Interfaces* **2023**, *15*, 57913.

[60] U. Biermann, U. Bornscheuer, M. A. R. Meier, J. O. Metzger, H. J. Schäfer, *Angewandte Chemie (International ed. in English)* **2011**, *50*, 3854.

[61] E. Yara-Varón, Y. Li, M. Balcells, R. Canela-Garayoa, A.-S. Fabiano-Tixier, F. Chemat, *Molecules (Basel, Switzerland)* **2017**, *22*.

[62] C. Wei, G. Zhang, Q. Zhang, X. Zhan, F. Chen, *ACS Applied Materials & Interfaces* **2016**, *8*, 34810.

[63] G. Xin, Y. Wang, Y. Sun, Q. Huang, L. Zhu, *Energy Conversion and Management* **2015**, *94*, 169.

[64] Y. Ren, J. Guo, Z. Liu, Z. Sun, Y. Wu, L. Liu, F. Yan, *Science Advances* **2019**, *5*, eaax0648.

[65] J. Wang, S. Zhang, Z. Ma, L. Yan, *Green Chemical Engineering* **2021**, *2*, 359.

[66] Y. H. Choi, R. Verpoorte, *Current Opinion in Food Science* **2019**, *26*, 87.

[67] V. G. Levich, V. S. Krylov, *Annu. Rev. Fluid Mech.* **1969**, *1*, 293.

[68] C. G. Gray, K. E. Gubbins, *Molecular Physics* **1975**, *30*, 179.

[69] B. Lautrup, *PHYSICS OF CONTINUOUS MATTEREXOTIC AND EVERYDAY PHENOMENA IN THE MACROSCOPIC W*, CRC Press, BOCA RATON **2011**.

[70] B. Chandesris, U. Soupremanien, N. Dunoyer, *Colloids and Surfaces A: Physicochemical and Engineering Aspects* **2013**, *434*, 126.

[71] Z. F. Gao, R. Liu, J. Wang, J. Dai, W.-H. Huang, M. Liu, S. Wang, F. Xia, L. Jiang, *Chem* **2018**, *4*, 2929.

[72] Y. P. Hou, S. L. Feng, L. M. Dai, Y. M. Zheng, *Chem. Mater.* **2016**, *28*, 3625.

[73] J. Li, X. Tian, A. P. Perros, S. Franssila, V. Jokinen, *Adv. Mater. Interfaces* **2014**, *1*, 1400001.

[74] T. Moragues, D. Arguijo, T. Beneyton, C. Modavi, K. Simutis, A. R. Abate, J.-C. Baret, A. J. deMello, D. Densmore, A. D. Griffiths, *Nat Rev Methods Primers* **2023**, *3*, 1.

[75] Y. Nakashima, Y. Nakanishi, T. Yasuda, *Review of Scientific Instruments* **2015**, *86*, 15001.

[76] J. Wang, P. H. Chao, S. Hanet, R. M. van Dam, *Lab on a chip* **2017**, *17*, 4342.

[77] J. Wu, S. Yadavali, D. Lee, D. A. Issadore, *Appl. Phys. Rev.* **2021**, *8*, 31304.

[78] L.-J. Pan, J.-W. Tu, H.-T. Ma, Y.-J. Yang, Z.-Q. Tian, D.-W. Pang, Z.-L. Zhang, *Lab on a chip* **2017**, *18*, 41.

[79] W. S. Y. Wong, *Nano Letters* **2019**, *19*, 1892.

[80] D. Tripathi, P. Ray, A. V. Singh, V. Kishore, S. L. Singh, *Coatings* **2023**, *13*, 1095.

[81] Y. Wang, X. Yao, J. Chen, Z. He, J. Liu, Q. Li, J. Wang, L. Jiang, *Sci. China Mater.* **2015**, *58*, 559.

[82] C. W. Extrand, *Langmuir* **2016**, *32*, 7697.

[83] Y. Si, C. Yu, Z. Dong, L. Jiang, *Current Opinion in Colloid & Interface Science* **2018**, *36*, 10.

[84] F. H. Chung, *Journal of Applied Polymer Science* **1991**, *42*, 1319.

[85] A. A. Tracton (Ed.), *Coatings technology: Fundamentals, testing, and processing techniques*, CRC Press, Boca Raton, FL **2007**.

[86] S. Ebnesajjad, in *Handbook of adhesives and surface preparation: Technology, applications and manufacturing* (Ed.: S. Ebnesajjad), William Andrew/Elsevier. Amsterdam **2011**, p. 3.

[87] J. W. Drelich, *Advances in Colloid and Interface Science* **2019**, *267*, 1.

[88] R. J. Good, *Journal of Adhesion Science and Technology* **1992**, *6*, 1269.

[89] A. B. D. Cassie, *Discuss. Faraday Soc.* **1948**, *3*, 11.

[90] R. N. Wenzel, *Industrial & Engineering Chemistry* **1936**, *28*, 988.

[91] R. N. Wenzel, *J. Phys. Chem.* **1949**, *53*, 1466.

[92] A. B. D. Cassie, S. Baxter, *Trans. Faraday Soc.* **1944**, *40*, 546.

[93] E. B. Dussan, *Annu. Rev. Fluid Mech.* **1979**, *11*, 371.

[94] E. Pierce, F. J. Carmona, A. Amirfazli, *Colloids and Surfaces A: Physicochemical and Engineering Aspects* **2008**, *323*, 73.

[95] T. Mouterde, P. S. Raux, C. Clanet, D. Quéré, *Proceedings of the National Academy of Sciences of the United States of America* **2019**, *116*, 8220.

[96] D. Wang, Q. Sun, M. J. Hokkanen, C. Zhang, F.-Y. Lin, Q. Liu, S.-P. Zhu, T. Zhou, Q. Chang, B. He, Q. Zhou, L. Chen, Z. Wang, R. H. A. Ras, X. Deng, *Nature* **2020**, *582*, 55.

[97] M. Backholm, D. Molpeceres, M. Vuckovac, H. Nurmi, M. J. Hokkanen, V. Jokinen, J. V. I. Timonen, R. H. A. Ras, *Commun Mater* **2020**, *1*, 1.

[98] L. Feng, S. Li, Y. Li, H. Li, L. Zhang, J. Zhai, Y. Song, B. Liu, L. Jiang, D. Zhu, *Advanced Materials* **2002**, *14*, 1857.

[99] H. P. Jansen, O. Bliznyuk, E. S. Kooij, B. Poelsema, H. J. W. Zandvliet, *Langmuir* **2012**, *28*, 499.

[100] M. Brinkmann, R. Lipowsky, *Journal of Applied Physics* **2002**, *92*, 4296.

[101] Y. Wu, F. Wang, M. Selzer, B. Nestler, *Physical review. E* **2019**, *100*, 41102.

[102] Y. Wu, F. Wang, S. Ma, M. Selzer, B. Nestler, *Soft Matter* **2020**, *16*, 6115.

[103] O. Bliznyuk, J. R. T. Seddon, V. Veligura, E. S. Kooij, H. J. W. Zandvliet, B. Poelsema, *ACS Applied Materials & Interfaces* **2012**, *4*, 4141.

[104] B. Majhy, V. P. Singh, A. K. Sen, *Journal of colloid and interface science* **2020**, *565*, 582.

[105] D. Jacqmin, *Journal of Computational Physics* **1999**, *155*, 96.

[106] P. Yue, *J. Fluid Mech.* **2020**, *899*.

[107] F. Wang, B. Nestler, *The Journal of chemical physics* **2021**, *154*, 94704.

[108] M. Sussman, P. Smereka, S. Osher, *Journal of Computational Physics* **1994**, *114*, 146.

[109] C. Hirt, B. Nichols, *Journal of Computational Physics* **1981**, *39*, 201.

[110] H. Kusumaatmaja, J. M. Yeomans, *Langmuir the ACS journal of surfaces and colloids* **2007**, *23*, 6019.

[111] Y. Wu, M. Kuzina, F. Wang, M. Reischl, M. Selzer, B. Nestler, P. A. Levkin, *Journal of colloid and interface science* **2022**, *606*, 1077.

[112] T.-S. Wong, S. H. Kang, S. K. Y. Tang, E. J. Smythe, B. D. Hatton, A. Grinthal, J. Aizenberg, *Nature* **2011**, *477*, 443.

[113] M. Villegas, Y. Zhang, N. Abu Jarad, L. Soleymani, T. F. Didar, *ACS Nano* **2019**, *13*, 8517.

[114] C. E. Colosqui, in *Encyclopedia of interfacial chemistry surface science and electrochemistry* (Ed.: K. 1. Wandelt), Elsevier. Oxford **uuuu-uuuu**, p. 654.

[115] G. McHale, B. V. Orme, G. G. Wells, R. Ledesma-Aguilar, *Langmuir* **2019**, *35*, 4197.

[116] F. Schellenberger, J. Xie, N. Encinas, A. Hardy, M. Klapper, P. Papadopoulos, H.-J. Butt, D. Vollmer, *Soft Matter* **2015**, *11*, 7617.

[117] M. R. Gunjan, A. Kumar, R. Raj, *Langmuir* **2021**, *37*, 6601.

[118] P. Che, L. Heng, L. Jiang, *Adv. Funct. Mater.* **2017**, *27*, 1606199.

[119] X. Hu, Y. Wang, H. Tang, Y. Xia, S. Huang, X. Xu, R. Zhang, *Lubricants* **2022**, *10*, 322.

[120] J. Li, E. Ueda, D. Paulssen, P. A. Levkin, *Adv. Funct. Mater.* **2019**, *29*, 1802317.

[121] S. Sett, X. Yan, G. Barac, L. W. Bolton, N. Miljkovic, *ACS Applied Materials & Interfaces* **2017**, *9*, 36400.

[122] M. P. Lautenschlaeger, S. Stephan, M. T. Horsch, B. Kirsch, J. C. Aurich, H. Hasse, *Procedia CIRP* **2018**, *67*, 296.

[123] T. Y. Woma, S. A. Lawal, A. S. Abdulrahman, M. A. Olutoye, M. M. Ojapah, *Tribology Online* **2019**, *14*, 60.

[124] K. Koch, W. Barthlott, *Philosophical transactions. Series A, Mathematical, physical, and engineering sciences* **2009**, *367*, 1487.

[125] Z. Wan, Q.-D. Wang, D. Liu, J. Liang, *Chemical Physics Letters* **2021**, *773*, 138589.

[126] C. Hu, J. Ai, L. Ma, P. Wen, M. Fan, F. Zhou, W. Liu, *ACS Omega* **2021**, *6*, 16343.

[127] P. R. Campos Flexa Ribeiro Filho, M. Rocha do Nascimento, S. S. Da Otaviano Silva, F. M. Tavares de Luna, E. Rodríguez-Castellón, C. Loureiro Cavalcante, *Lubricants* **2023**, *11*, 57.

[128] J. Song, *ACS Omega* **2021**, *6*, 29345.

[129] L. Yang, X. Zhao, Z. Ma, S. Ma, F. Zhou, *Friction* **2023**, *11*, 23.

[130] P. J. Flory, J. Rehner, *The Journal of chemical physics* **1943**, *11*, 521.

[131] T. Tanaka, D. Fillmore, S.-T. Sun, I. Nishio, G. Swislow, A. Shah, *Phys. Rev. Lett.* **1980**, *45*, 1636.

[132] S. Hirotsu, *The Journal of chemical physics* **1991**, *94*, 3949.

[133] N. Orakdogen, O. Okay, *European Polymer Journal* **2006**, *42*, 955.

[134] M. Shibayama, Y. Shirotani, H. Hirose, S. Nomura, *Macromolecules* **1997**, *30*, 7307.

[135] R. V. Godbole, F. Khabaz, R. Khare, R. C. Hedden, *The Journal of Physical Chemistry B* **2017**, *121*, 7963.

[136] H. S. Choi, I. H. Kim, Y. C. Bae, *J. Polym. Sci. B Polym. Phys.* **2001**, *39*, 1928.

[137] I. Barudio, G. Févotte, T. McKenna, *European Polymer Journal* **1999**, *35*, 775.

[138] S. Friesen, S. Kakorin, T. Hellweg, *Polymers* **2022**, *14*.

[139] N. Schuld, B. A. Wolf, *Polymer-Solvent Interaction Parameters*, John Wiley & Sons, Ltd **2003**.

[140] G. J. Price, A. J. Ashworth, *Polymer* **1987**, *28*, 2105.

[141] R. A. Orwoll, P. A. Arnold, in *Physical properties of polymer handbook* (Ed.: J. E. Mark), Springer New York. New York, NY **2007**, p. 233.

[142] A. Fernández-Nieves, A. Fernández-Barbero, B. Vincent, F. J. de las Nieves, *Macromolecules* **2000**, *33*, 2114.

[143] N. A. Pérez-Chávez, A. G. Albesa, G. S. Longo, *Macromolecules* **2021**, *54*, 2936.

[144] E. Weißenborn, B. Braunschweig, *Soft Matter* **2019**, *15*, 2876.

[145] L. Brannon-Peppas, N. A. Peppas, *Chemical Engineering Science* **1991**, *46*, 715.

[146] M. Rossi, P. Nardinocchi, T. Wallmersperger, *Proceedings. Mathematical, physical, and engineering sciences* **2019**, *475*, 20190174.

[147] K. Tong, J. Guo, S. Chen, F. Yu, S. Li, Z. Dai, *Geofluids* **2021**, *2021*, 1.

[148] Z. Chen, C. Cohen, F. A. Escobedo, *Macromolecules* **2002**, *35*, 3296.

[149]   M. Ignacio, G. W. Slater, *Physica A: Statistical Mechanics and its Applications* **2022**, *603*, 127775.

[150]   A. SANNINO, M. MADAGHIELE, L. AMBROSIO, in *Cellular response to biomaterials* (Ed.: L. Di Silvio), Woodhead. Cambridge, UK **2009**, p. 114.

[151]   N. Benmessaoud, S. Hamri, T. Bouchaour, U. Maschke, *Polym. Bull.* **2020**, *77*, 5567.

[152]   Y. Tian, Y. Tang, S. Li, H. Lv, P. Liu, Q. Jing, *e-Polymers* **2019**, *19*, 365.

[153]   Y. Chao, O. Ramírez-Soto, C. Bahr, S. Karpitschka, *Proceedings of the National Academy of Sciences of the United States of America* **2022**, *119*, e2203510119.

[154]   Y. Lu, C. Chang, *Frontiers in cell and developmental biology* **2022**, *10*, 910640.

[155]   Y. G. Zhao, H. Zhang, *Developmental Cell* **2020**, *55*, 30.

[156]   C. D. Keating, R. V. Pappu, *The Journal of Physical Chemistry B* **2021**, *125*, 12399.

[157]   *Nat Chem Biol* **2022**, *18*, 1289.

[158]   Z. Xu, W. Wang, Y. Cao, B. Xue, *Supramolecular Materials* **2023**, *2*, 100049.

[159]   D. R. Lloyd, S. S. Kim, K. E. Kinzer, *Journal of Membrane Science* **1991**, *64*, 1.

[160]   Y. Huang, J. Wang, N. Wang, X. Li, X. Ji, J. Yang, L. Zhou, T. Wang, X. Huang, H. Hao, *Chemical Engineering Science* **2022**, *262*, 118005.

[161]   S. S. Kim, D. R. Lloyd, *Polymer* **1992**, *33*, 1047.

[162]   Z. Dong, H. Cui, H. Zhang, F. Wang, X. Zhan, F. Mayer, B. Nestler, M. Wegener, P. A. Levkin, *Nat Commun* **2021**, *12*, 247.

[163]   V. A. Bobrin, Y. Yao, X. Shi, Y. Xiu, J. Zhang, N. Corrigan, C. Boyer, *Nat Commun* **2022**, *13*, 3577.

[164]   J. Xu, S. Xiu, Z. Lian, H. Yu, J. Cao, *Droplet* **2022**, *1*, 11.

[165]   W. Feng, E. Ueda, P. A. Levkin, *Advanced Materials* **2018**, *30*, e1706111.

[166]   H. Wu, X. Chen, X. Gao, M. Zhang, J. Wu, W. Wen, *Analytical chemistry* **2018**, *90*, 4303.

[167]   S. Kim, D. Yoo, S. Lee, J. Kim, *Adv. Mater. Interfaces* **2022**, *9*.

[168]   Z. Long, A. M. Shetty, M. J. Solomon, R. G. Larson, *Lab Chip* **2009**, *9*, 1567.

[169]   J. K. Park, S. Kim, *Lab on a chip* **2017**, *17*, 1793.

[170] J. Seo, S.-K. Lee, J. Lee, J. Seung Lee, H. Kwon, S.-W. Cho, J.-H. Ahn, T. Lee, *Sci Rep* **2015**, *5*, 12326.

[171] X. Wang, Z. Zhuang, X. Li, X. Yao, *Small Methods* **2023**.

[172] Y. Song, L. Wang, T. Xu, G. Zhang, X. Zhang, *Natl Sci Rev* **2023**, *10*, nwad106.

[173] M. Benz, A. Asperger, M. Hamester, A. Welle, S. Heissler, P. A. Levkin, *Nat Commun* **2020**, *11*, 5391.

[174] P. Zhang, M. Moretti, M. Allione, Y. Tian, J. Ordonez-Loza, D. Altamura, C. Giannini, B. Torre, G. Das, E. Li, S. T. Thoroddsen, S. M. Sarathy, I. Autiero, A. Giugni, F. Gentile, N. Malara, M. Marini, E. Di Fabrizio, *Commun Biol* **2020**, *3*, 457.

[175] N.-K. Nguyen, C. H. Ooi, P. Singha, J. Jin, K. R. Sreejith, H.-P. Phan, N.-T. Nguyen, *Processes* **2020**, *8*, 793.

[176] Y. Tang, X. Yang, L. Wang, Y. Li, Di Zhu, *ACS Applied Materials & Interfaces* **2023**, *15*, 21549.

[177] R. Wen, X. Ma, in *21st century surface science: A handbook* (Eds.: P. Pham, P. Goel, S. Kumar, K. Yadav), IntechOpen. London **2020**.

[178] X. Hu, Q. Yi, X. Kong, J. Wang, *Applied Sciences* **2021**, *11*, 1553.

[179] F. Wang, M. Liu, C. Liu, C. Huang, L. Zhang, A. Cui, Z. Hu, X. Du, *Natl Sci Rev* **2023**, *10*, nwac164.

[180] Y. Zhang, S. Jiang, Y. Hu, T. Wu, Y. Zhang, H. Li, an Li, Y. Zhang, H. Wu, Y. Ding, E. Li, J. Li, D. Wu, Y. Song, J. Chu, *Nano Letters* **2022**, *22*, 2923.

[181] K. S. Khalil, S. R. Mahmoudi, N. Abu-dheir, K. K. Varanasi, *Applied Physics Letters* **2014**, *105*.

[182] C. Yang, Q. Zeng, J. Huang, Z. Guo, *Advances in Colloid and Interface Science* **2022**, *306*, 102724.

[183] H. Dai, C. Gao, J. Sun, C. Li, N. Li, L. Wu, Z. Dong, L. Jiang, *Advanced Materials* **2019**, *31*, e1905449.

[184] Y. Liu, S. Bertels, M. Reischl, R. Peravali, M. Bastmeyer, A. A. Popova, P. A. Levkin, *Advanced Healthcare Materials* **2022**, *11*, e2200718.

[185] G. Oudeng, M. Benz, A. A. Popova, Y. Zhang, C. Yi, P. A. Levkin, M. Yang, *ACS Applied Materials & Interfaces* **2020**, *12*, 55614.

[186] G. Schneider, *Nat Rev Drug Discov* **2018**, *17*, 97.

[187] A. Sattari, P. Hanafizadeh, M. Hoorfar, *Advances in Colloid and Interface Science* **2020**, *282*, 102208.

[188] M. Mastiani, S. Seo, B. Mosavati, M. Kim, *ACS Omega* **2018**, *3*, 9296.

[189] Z. Huang, Y. Xie, H. Chen, Z. Yu, L. Shi, J. Jin, *Processes* **2023**, *11*, 983.

[190] T. Wang, C. Xu, *Lab Chip* **2020**, *20*, 1891.

[191] T. S. Kaminski, P. Garstecki, *Chem. Soc. Rev.* **2017**, *46*, 6210.

[192] K. Yiannacou, V. Sharma, V. Sariola, *Langmuir* **2022**, *38*, 11557.

[193] A. Keiser, L. Keiser, C. Clanet, D. Quéré, *Soft Matter* **2017**, *13*, 6981.

[194] J. Zhang, P. Liu, B. Yi, Z. Wang, X. Huang, L. Jiang, X. Yao, *ACS Nano* **2019**, *13*, 10596.

[195] M. Cao, D. Guo, C. Yu, K. Li, M. Liu, L. Jiang, *ACS Applied Materials & Interfaces* **2016**, *8*, 3615.

[196] V. Gold (Ed.), *The IUPAC Compendium of Chemical Terminology*, International Union of Pure and Applied Chemistry (IUPAC), Research Triangle Park, NC **2019**.

[197] M. Lescanne, A. Colin, O. Mondain-Monval, F. Fages, J.-L. Pozzo, *Langmuir* **2003**, *19*, 2013.

[198] S. Hou, J. Zhang, B. Huang, X. Wang, P. Xing, *Colloids and Surfaces A: Physicochemical and Engineering Aspects* **2022**, *648*, 129267.

[199] M. J. Zohuriaan-Mehr, K. Kabiri, M. Kheirabadi, *Journal of Applied Polymer Science* **2010**, *117*, 1127.

[200] Y.-S. Yang, C. Liang, C. Yang, Y.-P. Zhang, B.-X. Wang, J. Liu, *Spectrochimica acta. Part A, Molecular and biomolecular spectroscopy* **2020**, *237*, 118391.

[201] G. Zhu, J. S. Dordick, *Chem. Mater.* **2006**, *18*, 5988.

[202] J. Hao, F. An, C. Lu, Y. Liu, *Journal of Macromolecular Science, Part A* **2019**, *56*, 1012.

[203] M. Fernández-García, M. Fernández-Sanz, E. L. Madruga, R. Cuervo-Rodriguez, V. Hernández-Gordo, M. C. Fernández-Monreal, *J. Polym. Sci. A Polym. Chem.* **2000**, *38*, 60.

[204] K. Liang, R. A. Hutchinson, *Macromolecules* **2010**, *43*, 6311.

[205] I. Sideridou-Karayannidou, G. Seretoudi, *Polymer* **1997**, *38*, 4223.

[206] L. Li, J. M. Scheiger, T. Tronser, C. Long, K. Demir, C. L. Wilson, M. A. Kuzina, P. A. Levkin, *Advanced Functional Materials* **2019**, *29*.

[207] J. M. Scheiger, S. Li, M. Brehm, A. Bartschat, P. Theato, P. A. Levkin, *Adv. Funct. Mater.* **2021**, *31*, 2105681.

[208] H. Chang, C. Li, R. Huang, R. Su, W. Qi, Z. He, *J. Mater. Chem. B* **2019**, *7*, 2899.

[209] P. Eslami, F. Rossi, S. Fedeli, *Pharmaceutics* **2019**, *11*, 71.

[210] A. Hendi, M. Umair Hassan, M. Elsherif, B. Alqattan, S. Park, A. K. Yetisen, H. Butt, *International Journal of Nanomedicine* **2020**, *15*, 3887.

[211] C. Urata, H. Nagashima, B. D. Hatton, A. Hozumi, *ACS Applied Materials & Interfaces* **2021**, *13*, 28925.

[212] J. Lv, X. Yao, Y. Zheng, J. Wang, L. Jiang, *Advanced Materials* **2017**, *29*.

[213] Z. Gao, T. Xu, X. Miao, J. Lu, X. Zhu, Y. Song, G. Ren, Y. Jia, X. Li, *Surfaces and Interfaces* **2021**, *24*, 101022.

[214] X. Yao, S. Wu, L. Chen, J. Ju, Z. Gu, M. Liu, J. Wang, L. Jiang, *Angewandte Chemie International Edition* **2015**, *54*, 8975.

[215] P. Zhang, H. Liu, J. Meng, G. Yang, X. Liu, S. Wang, L. Jiang, *Advanced Materials* **2014**, *26*, 3131.

[216] H. Zhang, Y. Liang, P. Wang, D. Zhang, *Progress in Organic Coatings* **2019**, *132*, 132.

[217] X. Wang, J. Huang, Z. Guo, *Advances in Colloid and Interface Science* **2022**, *301*, 102602.

[218] F. Wang, B. Chen, L. Wu, Q. Zhao, L. Zhang, *Cell Reports Physical Science* **2020**, *1*, 100011.

[219] M. Wang, P. Zhang, M. Shamsi, J. L. Thelen, W. Qian, V. K. Truong, J. Ma, J. Hu, M. D. Dickey, *Nature Materials* **2022**, *21*, 359.

[220] Q. Zheng, X. Li, Q. Yang, C. Li, G. Liu, Y. Wang, P. Sun, H. Tian, C. Wang, X. Chen, J. Shao, *Journal of Power Sources* **2022**, *524*, 231102.

[221] F. Mo, G. Liang, Q. Meng, Z. Liu, H. Li, J. Fan, C. Zhi, *Energy & Environmental Science* **2019**, *12*, 706.

[222] K. Wang, J. Wang, L. Li, L. Xu, N. Feng, Y. Wang, X. Fei, J. Tian, Y. Li, *Chemical Engineering Journal* **2019**, *372*, 216.

[223] Y. Gao, L. Shi, S. Lu, T. Zhu, X. Da, Y. Li, H. Bu, G. Gao, S. Ding, *Chem. Mater.* **2019**, *31*, 3257.

[224] Y. Feng, J. Yu, D. Sun, W. Ren, C. Shao, R. Sun, *Chemical Engineering Journal* **2022**, *433*, 133202.

[225] W. Li, J. Zhang, J. Niu, X. Jin, X. Qian, C. Xiao, W. Wang, *Nano Energy* **2022**, *99*, 107359.

[226] T. Jing, B. Xu, Y. Yang, M. Li, Y. Gao, *Nano Energy* **2020**, *78*, 105373.

[227] Y.-S. Kim, Y.-G. Cho, D. Odkhuu, N. Park, H.-K. Song, *Scientific Reports* **2013**, *3*, 1917.

[228] M. M. Amaral, R. Venâncio, A. C. Peterlevitz, H. Zanin, *Journal of Energy Chemistry* **2022**, *67*, 697.

[229] Q. Rong, W. Lei, L. Chen, Y. Yin, J. Zhou, M. Liu, *Angewandte Chemie International Edition* **2017**, *56*, 14159.

[230] L. Li, Q. Wang, X. Liang, Z. Li, S. Guo, G. Sun, *Polymer Testing* **2021**, *99*, 107018.

[231] G. Chen, S. Liu, Z. Sun, S. Wen, T. Feng, Z. Yue, *Progress in Organic Coatings* **2020**, *144*, 105641.

[232] Y. Zhuo, J. Chen, S. Xiao, T. Li, F. Wang, J. He, Z. Zhang, *Mater. Horiz.* **2021**, *8*, 3266.

[233] B. Eslami, P. Irajizad, P. Jafari, M. Nazari, A. Masoudi, V. Kashyap, S. Stafslien, H. Ghasemi, *Soft Matter* **2019**, *15*, 6014.

[234] H. M. J. Boots, J. G. Kloosterboer, C. Serbutoviez, F. J. Touwslager, *Macromolecules* **1996**, *29*, 7683.

[235] A. Sicher, R. Ganz, A. Menzel, D. Messmer, G. Panzarasa, M. Feofilova, R. O. Prum, R. W. Style, V. Saranathan, R. M. Rossi, E. R. Dufresne, *Soft Matter* **2021**, *17*, 5772.

[236] S. C. Leguizamon, J. Ahn, S. Lee, B. H. Jones, *Soft Matter* **2022**, *18*, 4455.

[237] P. Zhang, D. C. Sundberg, J. G. Tsavalas, *Ind. Eng. Chem. Res.* **2019**, *58*, 21118.

[238] Z. Dong, J. Monti, H. Cui, A. Welle, S. A. Singaraju, E. Blasco, P. A. Levkin, *Adv Materials Technologies* **2023**, *8*.

[239] K. Xia, Z. Dong, Q. Sun, R. Debastiani, S. Liu, Q. Jin, Y. Li, U. W. Paetzold, P. Gumbsch, U. Lemmer, Y. M. Eggeler, P. A. Levkin, G. Hernandez-Sosa, *Adv Materials Technologies* **2023**, *8*.

[240] Z. Dong, M. Vuckovac, W. Cui, Q. Zhou, R. H. A. Ras, P. A. Levkin, *Advanced Materials* **2021**, *33*, e2106068.

[241] J. M. Scheiger, M. A. Kuzina, M. Eigenbrod, Y. Wu, F. Wang, S. Heißler, S. Hardt, B. Nestler, P. A. Levkin, *Advanced Materials* **2021**, *33*, e2100117.

[242] B. Xiong, K. Ren, Y. Shu, Y. Chen, B. Shen, H. Wu, *Advanced Materials* **2014**, *26*, 5525.

[243] V. Narayanamurthy, Z. E. Jeroish, K. S. Bhuvaneshwari, P. Bayat, R. Premkumar, F. Samsuri, M. M. Yusoff, *RSC Adv.* **2020**, *10*, 11652.

[244] J. J. Heiland, R. Warias, C. Lotter, L. Mauritz, P. J. W. Fuchs, S. Ohla, K. Zeitler, D. Belder, *Lab Chip* **2016**, *17*, 76.

[245] S. Pan, R. Guo, M. Björnmalm, J. J. Richardson, L. Li, C. Peng, N. Bertleff-Zieschang, W. Xu, J. Jiang, F. Caruso, *Nature Materials* **2018**, *17*, 1040.

[246] S. S. Latthe, R. S. Sutar, A. K. Bhosale, K. K. Sadasivuni, S. Liu, *Superhydrophobic surfaces for oil-water separation*, Elsevier **2019**, 339.

[247] A. I. Neto, C. R. Correia, C. A. Custódio, J. F. Mano, *Advanced Functional Materials* **2014**, *24*, 5096.

[248] H. Cui, W. Wang, L. Shi, W. Song, S. Wang, *Small Methods* **2020**, *4*.

[249]   M. Benz, M. R. Molla, A. Böser, A. Rosenfeld, P. A. Levkin, *Nat Commun* **2019**, *10*, 2879.

[250]   B. Wang, Y. Zhang, W. Liang, G. Wang, Z. Guo, W. Liu, *J. Mater. Chem. A* **2014**, *2*, 7845.

[251]   J. Wang, W. Gao, H. Zhang, M. Zou, Y. Chen, Y. Zhao, *Science Advances* **2018**, *4*, eaat7392.

[252]   M. Tenjimbayashi, M. Higashi, T. Yamazaki, I. Takenaka, T. Matsubayashi, T. Moriya, M. Komine, R. Yoshikawa, K. Manabe, S. Shiratori, *ACS Applied Materials & Interfaces* **2017**, *9*, 10371.

[253]   L. Ni, C. Dietlin, A. Chemtob, C. Croutxé-Barghorn, J. Brendlé, *Langmuir* **2014**, *30*, 10118.

[254]   Y.-K. Lai, Y.-X. Tang, J.-Y. Huang, F. Pan, Z. Chen, K.-Q. Zhang, H. Fuchs, L.-F. Chi, *Scientific Reports* **2013**, *3*, 3009.

[255]   W. Feng, L. Li, X. Du, A. Welle, P. A. Levkin, *Advanced Materials* **2016**, *28*, 3202.

[256]   S. P. R. Kobaku, A. K. Kota, D. H. Lee, J. M. Mabry, A. Tuteja, *Angewandte Chemie International Edition* **2012**, *51*, 10109.

[257]   P. Liu, W. He, G. Lu, H. Zhang, Z. Wang, X. Yao, *J. Mater. Chem. A* **2017**, *5*, 16344.

[258]   P. Zhu, T. Kong, X. Tang, L. Wang, *Nat Commun* **2017**, *8*, 15823.

[259]   V. Jokinen, L. Sainiemi, S. Franssila, *Advanced Materials* **2008**, *20*, 3453.

[260]   D. Paulssen, W. Feng, I. Pini, P. A. Levkin, *Adv. Mater. Interfaces* **2018**, *5*.

[261]   J. Forth, X. Liu, J. Hasnain, A. Toor, K. Miszta, S. Shi, P. L. Geissler, T. Emrick, B. A. Helms, T. P. Russell, *Advanced Materials* **2018**, *30*, e1707603.

[262]   E. H. Wong, E. Rondeau, P. Schuetz, J. Cooper-White, *Lab Chip* **2009**, *9*, 2582.

[263]   P. Dunne, T. Adachi, A. A. Dev, A. Sorrenti, L. Giacchetti, A. Bonnin, C. Bourdon, P. H. Mangin, J. M. D. Coey, B. Doudin, T. M. Hermans, *Nature* **2020**, *581*, 58.

[264]   I. Martinez, J. M. Haynes, D. Langbein, in *Fluid Sciences and Materials Science in Space* (Ed.: H. U. Walter), Springer-Verlag. Berlin, Heidelberg **uuuu-uuuu**, p. 53.

[265]   P.-G. de Gennes, F. Brochard-Wyart, D. Quéré, *Capillarity and wetting phenomena: Drops, bubbles, pearls, waves*, Springer, New York, London **2010**.

[266] M. Ben Said, M. Selzer, B. Nestler, D. Braun, C. Greiner, H. Garcke, *Langmuir* **2014**, *30*, 4033.

[267] H. Sobol, J. Garfias, J. Keller, *J. Phys. Chem.* **1976**, *80*, 1941.

[268] D. Villers, J. K. Platten, *J. Phys. Chem.* **1988**, *92*, 4023.

[269] A. Estrada-Baltazar, J. l. S. López-Lázaro, G. A. Iglesias-Silva, J. Barajas-Fernández, *The Journal of Chemical Thermodynamics* **2020**, *150*, 106225.

[270] A. H. Demond, A. S. Lindner, *Environ. Sci. Technol.* **1993**, *27*, 2318.

[271] Y.-C. Lee, Y.-B. Liou, R. Miller, H.-S. Liu, S.-Y. Lin, *Langmuir* **2002**, *18*, 2686.

[272] R. Stephenson, J. Stuart, *J. Chem. Eng. Data* **1986**, *31*, 56.

[273] F. Zhang, J.-B. Fan, S. Wang, *Angewandte Chemie International Edition* **2020**, *59*, 21840.

[274] C. L. Esposito, P. Kirilov, V. G. Roullin, *Journal of controlled release official journal of the Controlled Release Society* **2018**, *271*, 1.

[275] Y. Long, B. Jiang, T. Huang, Y. Liu, J. Niu, Z. L. Wang, W. Hu, *Adv. Funct. Mater.* **2023**, https://onlinelibrary.wiley.com/doi/10.1002/adfm.202304625.

[276] P. Charoensumran, H. Ajiro, *Polym J* **2018**, *50*, 1021.

[277] A. Khan, R. R. Kisannagar, S. Mahmood, W.-T. Chuang, M. Katiyar, D. Gupta, H.-C. Lin, *ACS Applied Materials & Interfaces* **2023**.

[278] J.-M. Park, J. Park, Y.-H. Kim, H. Zhou, Y. Lee, S. H. Jo, J. Ma, T.-W. Lee, J.-Y. Sun, *Nature communications* **2020**, *11*, 4638.

[279] F. Mo, Y. Huang, Q. Li, Z. Wang, R. Jiang, W. Gai, C. Zhi, *Adv. Funct. Mater.* **2021**, *31*, 2010830.

[280] J. Lv, X. Yao, Y. Zheng, J. Wang, L. Jiang, *Advanced materials (Deerfield Beach, Fla.)* **2017**, *29*.

[281] Z. Li, B. Zhang, S. Jia, M. Ma, J. Hao, *Journal of Molecular Liquids* **2018**, *250*, 19.

[282] N. L. Smith, A. E. Coukouma, D. C. Wilson, B. Ho, V. Gray, S. A. Asher, *ACS Applied Materials & Interfaces* **2020**, *12*, 238.

[283] Y. Jia, G. Sciutto, R. Mazzeo, C. Samorì, M. L. Focarete, S. Prati, C. Gualandi, *ACS Applied Materials & Interfaces* **2020**, *12*, 39620.

[284] Y. Yu, B. Jin, M. I. Jamil, D. Cheng, Q. Zhang, X. Zhan, F. Chen, *ACS Applied Materials & Interfaces* **2019**, *11*, 12838.

[285] H. Liu, P. Zhang, M. Liu, S. Wang, L. Jiang, *Advanced materials (Deerfield Beach, Fla.)* **2013**, *25*, 4477.

[286] Y. Zhang, Y. Zhao, Z. Peng, B. Yao, Y. Alsaid, M. Hua, D. Wu, Y. Qiu, Q. Pei, X. Zhu, Z. He, X. He, *ACS Materials Lett.* **2021**, *3*, 1477.

[287] Y. Wang, X. Yao, S. Wu, Q. Li, J. Lv, J. Wang, L. Jiang, *Advanced materials (Deerfield Beach, Fla.)* **2017**, *29*.

[288] B. Eslami, P. Irajizad, P. Jafari, M. Nazari, A. Masoudi, V. Kashyap, S. Stafslien, H. Ghasemi, *Soft Matter* **2019**, *15*, 6014.

[289] H. Y. Lai, A. d. Leon, K. Pangilinan, R. Advincula, *Progress in Organic Coatings* **2018**, *115*, 122.

[290] X. Yao, J. Ju, S. Yang, J. Wang, L. Jiang, *Advanced materials (Deerfield Beach, Fla.)* **2014**, *26*, 1895.

[291] Z. Zhang, L. Wang, H. Yu, F. Zhang, L. Tang, Y. Feng, W. Feng, *ACS Applied Materials & Interfaces* **2020**, *12*, 15657.

[292] P. Zhang, H. Liu, J. Meng, G. Yang, X. Liu, S. Wang, L. Jiang, *Advanced materials (Deerfield Beach, Fla.)* **2014**, *26*, 3131.

[293] Di Chen, C. Ni, L. Xie, Y. Li, S. Deng, Q. Zhao, T. Xie, *Science Advances* **2021**, *7*, eabi7360.

[294] J. Oh, D. Baek, T. K. Lee, D. Kang, H. Hwang, E. M. Go, I. Jeon, Y. You, C. Son, D. Kim, M. Whang, K. Nam, M. Jang, J.-H. Park, S. K. Kwak, J. Kim, J. Lee, *Nature Materials* **2021**, *20*, 385.

[295] C. Zhao, Q. Lv, W. Wu, *Gels (Basel, Switzerland)* **2022**, *8*.

[296] K. Ahmed, M. N. I. Shiblee, A. Khosla, L. Nagahara, T. Thundat, H. Furukawa, *J. Electrochem. Soc.* **2020**, *167*, 37563.

[297] Y. Zhang, Y. Zhao, D. Wu, J. Xue, Y. Qiu, M. Liao, Q. Pei, M. S. Goorsky, X. He, *Advanced Materials* **2019**, *31*, e1902928.

[298] C. S. O'Bryan, T. Bhattacharjee, S. Hart, C. P. Kabb, K. D. Schulze, I. Chilakala, B. S. Sumerlin, W. G. Sawyer, T. E. Angelini, *Science Advances* **2017**, *3*, e1602800.

[299]   F. Horkay, A. M. Hecht, E. Geissler, *The Journal of chemical physics* **1989**, *91*, 2706.

[300]   G. Hoti, F. Caldera, C. Cecone, A. Rubin Pedrazzo, A. Anceschi, S. L. Appleton, Y. Khazaei Monfared, F. Trotta, *Materials (Basel, Switzerland)* **2021**, *14*.

[301]   H. Zhang, P. Wang, D. Zhang, *Colloids and Surfaces A: Physicochemical and Engineering Aspects* **2018**, *538*, 140.

[302]   Z. Wang, H. Zhu, J. Huang, Z. Ge, J. Guo, X. Feng, Q. Xu, *International Journal of Biological Macromolecules* **2019**, *126*, 603.

[303]   Z. Li, C. Yu, H. Kumar, X. He, Q. Lu, H. Bai, K. Kim, J. Hu, *Gels (Basel, Switzerland)* **2022**, *8*.

[304]   W. M. Haynes, *CRC handbook of chemistry and physics: A ready-reference book of chemical and physical data*, CRC Press, Boca Raton **2014**.

[305]   L. Dagdug, M.-V. Vazquez, A. M. Berezhkovskii, V. Y. Zitserman, S. M. Bezrukov, *The Journal of chemical physics* **2012**, *136*, 204106.

[306]   M. A. Kuzina, C. M. Kurpiers, Y.-Y. Tsai, R. Schwaiger, S.-W. Chang, P. Levkin, *Macromol. Mater. Eng.* **2023**, *308*.

[307]   Q. Tran-Cong-Miyata, H. Nakanishi, *Polymer International* **2017**, *66*, 213.

[308]   S. C. Leguizamon, J. Powers, J. Ahn, S. Dickens, S. Lee, B. H. Jones, *Macromolecules* **2021**, *54*, 7796.

[309]   Y. Chen, N. Wang, O. Ola, Y. Xia, Y. Zhu, *Materials Science and Engineering: R: Reports* **2021**, *143*, 100589.

[310]   F.-L. Jin, M. Zhao, M. Park, S.-J. Park, *Polymers* **2019**, *11*.

[311]   F. Mayer, D. Ryklin, I. Wacker, R. Curticean, M. Čalkovský, A. Niemeyer, Z. Dong, P. A. Levkin, D. Gerthsen, R. R. Schröder, M. Wegener, *Advanced Materials* **2020**, *32*, e2002044.

[312]   W. Deng, S. Kumar, A. Vallone, D. M. Kochmann, J. R. Greer, *Advanced Materials* **2024**.

[313]   J. Göken, N. Saba, *Acta Phys. Pol. A* **2020**, *138*, 844.

[314]   E. Truszkiewicz, A. Thalhamer, M. Rossegger, M. Vetter, G. Meier, E. Rossegger, P. Fuchs, S. Schlögl, M. Berer, *Journal of Applied Polymer Science* **2022**, *139*.

[315]   X. Pei, M. Zhao, R. Li, H. Lu, R. Yu, Z. Xu, D. Li, Y. Tang, W. Xing, *Composites Part A: Applied Science and Manufacturing* **2021**, *145*, 106363.

[316]   G. Liu, R. Yu, D. Liu, Y. Xia, X. Pei, W. Wang, C. Min, S. Liu, R. Shao, Z. Xu, *Composites Part A: Applied Science and Manufacturing* **2022**, *160*, 107058.

[317]   X. Pei, G. Liu, H. Shi, R. Yu, S. Wang, S. Liu, C. Min, J. Song, R. Shao, Z. Xu, *Composites Science and Technology* **2023**, *233*, 109909.

[318]   D. Liu, B. Šavija, G. E. Smith, P. E. J. Flewitt, T. Lowe, E. Schlangen, *International Journal of Fracture* **2017**, *205*, 57.

[319]   E. Chen, S. Luan, S. Gaitanaros, *Extreme Mechanics Letters* **2022**, *51*, 101598.

[320]   O. Eren, H. K. Sezer, N. Yalçın, *Journal of Manufacturing Processes* **2022**, *75*, 1175.

[321]   J. Bauer, L. R. Meza, T. A. Schaedler, R. Schwaiger, X. Zheng, L. Valdevit, *Advanced Materials* **2017**, *29*.

[322]   X. Zheng, H. Lee, T. H. Weisgraber, M. Shusteff, J. DeOtte, E. B. Duoss, J. D. Kuntz, M. M. Biener, Q. Ge, J. A. Jackson, S. O. Kucheyev, N. X. Fang, C. M. Spadaccini, *Science* **2014**, *344*, 1373.

[323]   M. Kadic, G. W. Milton, M. van Hecke, M. Wegener, *Nat Rev Phys* **2019**, *1*, 198.

[324]   Arjunan A., *Encyclopedia of Smart Materials* **2020**.

[325]   H. Ma, C. Feng, J. Chang, C. Wu, *Acta Biomaterialia* **2018**, *79*, 37.

[326]   F. S. L. Bobbert, S. Janbaz, A. A. Zadpoor, *J. Mater. Chem. B* **2018**, *6*, 3449.

[327]   R. Hedayati, A. M. Leeflang, A. A. Zadpoor, *Applied Physics Letters* **2017**, *110*.

[328]   Z. Jia, F. Liu, X. Jiang, L. Wang, *Journal of Applied Physics* **2020**, *127*.

[329]   C. M. Kurpiers, S. Hengsbach, R. Schwaiger, *MRS Advances* **2021**, *6*, 507.

[330]   G. A. Buxton, C. M. Care, D. J. Cleaver, *Modelling Simul. Mater. Sci. Eng.* **2001**, *9*, 485.

[331]   F. Libonati, V. Cipriano, L. Vergani, M. J. Buehler, *ACS Biomaterials Science & Engineering* **2017**, *3*, 3236.

[332]   H. Chen, E. Lin, Y. Liu, *International Journal of Solids and Structures* **2014**, *51*, 1819.

[333] Y. Chiang, C.-C. Tung, X.-D. Lin, P.-Y. Chen, C.-S. Chen, S.-W. Chang, *Composite Structures* **2021**, *262*, 113349.

[334] Y. Kim, Y. Kim, F. Libonati, S. Ryu, *Composites Part B: Engineering* **2019**, *167*, 736.

[335] A. Ghimire, Y.-Y. Tsai, P.-Y. Chen, S.-W. Chang, *Composites Part B: Engineering* **2021**, *215*, 108754.

[336] Y. Chiang, T.-W. Chiu, S.-W. Chang, *Front. Mater.* **2022**, *8*.

[337] *https://www.ansys.com/products/materials/granta-edupack(accessed:2023)* **2023**, https://www.ansys.com/products/materials/granta-edupack(accessed:2023).

[338] M. F. Ashby, *Philosophical transactions. Series A, Mathematical, physical, and engineering sciences* **2006**, *364*, 15.

[339] L. Helden, K. Dietrich, C. Bechinger, *Langmuir the ACS journal of surfaces and colloids* **2016**, *32*, 13752.

[340] C. Huh, S. G. Mason, *Colloid & Polymer Sci* **1975**, *253*, 566.

[341] C. A. Schneider, W. S. Rasband, K. W. Eliceiri, *Nature Methods* **2012**, *9*, 671.

[342] A. P. Thompson, H. M. Aktulga, R. Berger, D. S. Bolintineanu, W. M. Brown, P. S. Crozier, P. J. in 't Veld, A. Kohlmeyer, S. G. Moore, T. D. Nguyen, R. Shan, M. J. Stevens, J. Tranchida, C. Trott, S. J. Plimpton, *Computer Physics Communications* **2022**, *271*, 108171.

9 Appendix

Curriculum Vitae

EDUCATION

Ph.D. Candidate in Chemistry	– **Karlsruhe Institute of Technology (KIT), 01/2020-09/2023**

Group of Prof. Levkin, financed by Carl Zeiss Stipend

B.Sc. and M.Sc. in Materials Science	– **Lomonosov Moscow State University,**
M.Sc. with honors	**2013-2019**

RESEARCH EXPERIENCE

Doctoral candidate	– **Karlsruhe Institute of Technology (KIT), 01/2020-09/2023**

- Liquid systems on surfaces with patterned wettability: results published in Advanced Materials (02/21) and Journal of Colloidal Science (08/21)

- Comprehensive progress review about the current progress, distinctive properties, and applications of organogels, published in Advanced Functional Materials (04/23)

- DLP-based 3D-printing of functional polymers:

  1) organogels with solvent-induced properties, *in submission* (02/24)

  2) stiff, lightweight inherently porous polymers, 1st-author manuscript, published in Macromolecular Materials and Engineering (06/23)

Master Student	– **Karlsruhe Institute of Technology (KIT)**
	– **& Lomonosov Moscow State University, 10/2018-06/2019**

- Graduate qualification work: 3D-printed hydrophilic-hydrophobic polyacrylate-based scaffolds for tissue engineering (Grade: excellent, 1.0)

Internship	– **Karlsruhe Institute of Technology (KIT), 07/2018-09/2018**

- Investigated UV-degradation products of methacrylate-based polymers, published in Advanced Functional Materials (06/19)

- Fabricated patterned hydrophilic-hydrophobic surfaces for self-organized liquid-liquid assemblies

Bachelor Student - **Lomonosov Moscow State University, 09/2017-06/2018**

- Graduate qualification work: Synthesis of calcium phosphate powders in non-aqueous media to fabricate osteoconductive resorbable bioceramics, published in [Russian Journal of Inorganic Chemistry](03/20)

INDUSTRY EXPERIENCE

Innovation Researcher - **Nissan Research Center Ltd., Russia, Moscow, 07/2017-11/2019**

- Made over 20 state-of-the-art research reports in 2.5 years to determine 10-15 years' innovation strategy for Nissan's R&D and innovation teams

- Provided research summaries of electromobility, energy harvesting, generation and storage, acoustic metamaterials, advanced manufacturing for automotive

- Evaluated key collaborators for Nissan innovation programs in Russian automotive industry

PUBLICATIONS

- 3D-printed organogels with solvent-assisted tuneable thermal stability, slippery non-adhesive surface and increased extracting efficiency. M. Kuzina et al., *submitted, under revision*

- 3D-printed inherently porous structures with tetrahedral lattice architecture: experimental and computational study of the mechanical behavior. M. Kuzina et al. Macromolecular Materials and Engineering, 2023

- Organogels versus Hydrogels: Advantages, Challenges, and Applications. M. Kuzina et al. Advanced Functional Materials, 2023

- Inhibition of lysyl oxidases synergizes with 5-azacytidine to restore erythropoiesis in myelodysplastic and myeloid malignancies. Q. Xu et al. Nature Communications, 2023

- Equilibrium droplet shapes on chemically patterned surfaces: theoretical calculation, phase-field simulation, and experiments. Y. Wu, <u>M. Kuzina</u> et al. Journal of Colloidal Science, 2021

- Designing Inherently Photodegradable Cell-Adhesive Hydrogels for 3D Cell Culture. A. Rosenfeld, T. Göckler, <u>M. Kuzina</u> et al. Advanced Healthcare Materials, 2021

- Liquid Wells as Self-Healing, Functional Analogues to Solid Vessels. J. Scheiger, <u>M. Kuzina</u> et al. Advanced Materials, 2021

- Synthesis of calcium phosphate powders in non-aqueous media for stereolithography 3D-printing.
  D. Larionov, <u>M. Kuzina</u> et al. Russian Journal of Inorganic Chemistry, 2020

- Inherent Photodegradability of Polymethacrylate Hydrogels: Straightforward Access to Biocompatible Soft Microstructures. L. Li et al. Advanced Functional Materials, 2019

CONFERENCES

- Materials Science and Engineering Congress 2022, poster (Darmstadt, Germany)
- 28th annual conference of the European Society for Biomaterials 2017, poster (Athens, Greece)
- XXVII Mendeleev conference of young scientists 2017 poster, talk (Ufa, Russia), 3rd best work award
- CPSSC16: Challenges and Prospects for Solid State Chemistry 2016, poster (Seville, Spain)
- 11th Conference for Young Scientists in Ceramics 2015, poster (Novi Sad, Serbia)
- International Conference for Young Scientists "Lomonosov" 2015, poster, talk (Moscow, Russia), 2nd best work award
- XXV Mendeleev conference of young scientists 2015, poster, talk (Tomsk, Russia), 3rd best work award

Acknowledgments

I owe a deep gratitude to my dear family, who supported me throughout this entire journey. To my mom Anna, dad Alexei, and my two amazing, supportive, and sweet brothers, Alexei with his wife Maria, and Nikolai, your love and encouragement have been my rock. I miss time with you the most.

A heartfelt thank you goes to Professor Pavel Levkin for believing in me and seeing a potential in me back in 2018 when I first joined the group. You shaped me as a professional and taught me the endless amount of lessons on how to be a proper project manager, scientific writer, innovative thinker, and on top not too bad of a scientist. I am very grateful for this growth.

I am thankful for the possibilities that all my collaborators, Cluster 3DMM2O and Carl Zeiss Scholarship, and my graduate schools gave me during my PhD time. Without you, none of my projects would be possible to accomplish.

Warm greetings go to my dear work colleagues, who have always cheered me up, taught me skills and methods, supported me in the hardships, and just went this whole way along with me. A particular thanks for always making me feel great go to Marius Brehm, Johannes Scheiger, Charlotte Luchena, Nikolaj Mandsberg, Maximilian Seifermann, Julius Höpfner, Sida Liu, Zheqin Dong, Wenxi Ley, Yanxi Liu, Julián Serna, Lutong Lu, Tatiana Starikova, Jovana Topalovska, Roxana Grömmer, Weiyi Liu, Qian-Pu (Antonio) Cheng, Junning Zhang, Fatma Aslan, Shraddha Chakraborty, Haijun Cui, Jonathan Elton, Yelda Nur Demirdögen, Konstantin Demir, and everyone who I didn't mention in this already too long list of names, for your invaluable support. I am also very grateful for the opportunity to collaborate and lead projects with the Chantal Kurpiers and Yanchen Wu, very supportive colleagues and talented young scientists. Working with you was a pleasure!

To new colleagues from MCQST and MQV: thank you for being very supportive at those late stages of my writing and for welcoming me so warmly in my new role as a program coordinator. I am continuously lucky with colleagues!

I would like to thank the whole team of my co-founders of our mentor program Sci.STEPS, who have been waiting until I defend and finally can spend more of my free time on helping our project grow and proliferate. I'm on it, I promise! I am so happy I met you in September 2022 and so proud of our progress.